

DMITRII SOLOMITCKII

Evaluation of mmWave 5G Performance by Advanced Ray Tracing Techniques

DMITRII SOLOMITCKII

Evaluation of mmWave 5G
Performance by Advanced
Ray Tracing Techniques

ACADEMIC DISSERTATION

To be presented, with the permission of
the Faculty of Information Technology and Communication Sciences
of Tampere University,
for public discussion in the TB207
of the Tietotalo, Korkeakoulunkatu 10, Tampere,
on 10 December 2019, at 12 o'clock.

ACADEMIC DISSERTATION

Tampere University, Faculty of Information Technology and Communication Sciences
Finland

<i>Responsible supervisor and Custos</i>	Prof. Yevgeni Koucheryavy Tampere University Finland	
<i>Supervisor(s)</i>	Assist. Prof. Sergey Andreev Tampere University Finland	
<i>Pre-examiner(s)</i>	Prof. Tapani Ristaniemi University of Jyväskylä Finland	Prof. Sundeep Rangan New York University United States
<i>Opponent(s)</i>	Prof. Thomas Kürner Technical University of Braunschweig Germany	

The originality of this thesis has been checked using the Turnitin OriginalityCheck service.

Copyright ©2019 author

Cover design: Roihu Inc.

ISBN 978-952-03-1368-5 (print)
ISBN 978-952-03-1369-2 (pdf)
ISSN 2489-9860 (print)
ISSN 2490-0028 (pdf)
<http://urn.fi/URN:ISBN:978-952-03-1369-2>

PunaMusta Oy – Yliopistopaino
Tampere 2019

Dedicated to my family...

PREFACE/ACKNOWLEDGEMENTS

This thesis relies on the academic work carried out at the Electrical Engineering Unit of Tampere University (TAU) and formerly Department of Electronics and Communications Engineering of Tampere University of Technology (TUT) between 2014 and 2019.

During this period, many people have supported and guided me towards the fruitful results. First of all, I would like to thank Prof. Yevgeni Koucheryavy, who has been supervising my PhD study within these five fascinated years. I also appreciate the help of Asst. Prof. Sergey Andreev with my publishing activity; his experience and advice have greatly improved the quality of my articles.

The most significant contribution has come from the Intel Labs team (Santa Clara, CA), who formulated the most relevant tasks for the mmWave 5G. Specifically, Dr. Hosein Nikopour, Dr. Mustafa Akdeniz, Dr. Shilpa Talwar, Dr. Nageen Himayat, Dr. Qian (Clara) Li, Dr. Tommaso Balercia, and Dr. Claudio R. C. M. da Silva, who were all part of the team whom I had the pleasure to work with. I would like to acknowledge financial support from Intel Labs, project 5G-FORCE, and RAAS Connectivity RTF framework.

I would like to express my appreciation to my colleagues Dr. Vasilii Semkin, Vitaly Petrov, Margarita Gapeyenko, Dr. Alexander Pyattaev and Dr. Aleksandr Ometov for their distinct contributions to this research. I also want to express my appreciation to Adj. Prof. Sebastian Szyszkowicz and Prof. Halim Yanikomeroglu from the Carleton University for the fruitful collaboration on the topic of massive simulation.

Every hypothesis should be verified by measurements. Therefore, I would like to express special thanks to Prof. Mikko Valkama and Prof. Katsuyuki Haneda for affording me the opportunity to work with world-class millimeter-wave sounding equipment.

Dmitrii Solomitckii. November 15, 2019, Tampere, Finland

ABSTRACT

Technological progress leads to the emergence of new concepts, which can change people's everyday lives and accelerate the transformation of many industries. Among the more recent of these revolutionary concepts are big data analysis, artificial intelligence, augmented/virtual reality, quantum computing, and autonomous vehicles. However, this list would be incomplete without referring to fifth-generation (5G) technology, which is driven by several trends. First, the exponential growth of the worldwide monthly smartphone traffic up to 50 petabytes during the next three years will require the development of mobile networks supporting high data-sharing capabilities, excellent spectral efficiency, and gigabits per second of throughput. Another trend is Industry 4.0/5.0 (also called the smart factory), which refers to advanced levels of automation requiring millions of distributed sensors/devices connected into a scalable and smart network. Finally, the automation of critical industrial processes, as well as communication between autonomous vehicles, will require 99.999% reliability and under 1 ms latency as they also become the drivers for the emergence of 5G.

Besides traditional sub-6 GHz microwave spectrum, the 5G communication encompasses the novel millimeter-wave bands to mitigate spectrum scarcity and provide large bandwidth of up to several GHz. However, there are challenges to be overcome with the millimeter-wave band. The band suffers from higher pathloss, more atmospheric attenuation, and higher diffraction losses than microwave signals. Because the millimeter-wave band has such a small wavelength (< 1 cm), it is now feasible to implement compact antenna arrays. This enables the use of beamforming and multi-input and multi-output techniques. In this thesis, advanced ray tracing methodology is developed and utilized to simulate the propagation mechanisms and their effect on the system-level metrics. The main novelty of this work is in the introduction of typical millimeter-wave 5G technologies into channel modelling and propagation specifics into the system-level simulation, as well as the adaptation of the ray tracing methods to support extensive simulations with multiple antennas.

CONTENTS

1	Introduction	21
1.1	Research Motivation	21
1.2	Main Contribution and Scope	23
1.3	Structure of the Thesis	23
2	Wireless Channel and Models	25
2.1	Wireless Channel Properties	25
2.2	Channel Models and Simulators	27
2.2.1	Classification of Channel Models	27
2.2.2	Overview of the mmWave Channel Models and Simulators	28
3	The Background to Ray-Tracing	31
3.1	Ray Field Theory	31
3.1.1	Geometrical Optics	31
3.1.2	Geometrical/Uniform Theory of Diffraction	32
3.1.3	Electromagnetic Theory	33
3.1.4	High-frequency Asymptotic Solution of Electromagnetic Fields	34
3.2	The Practical Implementation of a Ray Field	36
3.2.1	Propagation Geometry Models	37
3.2.1.1	Image-based Ray Tracing	37
3.2.1.2	Ray-Launching	37
3.2.2	Acceleration Techniques	38
3.2.3	Physical Models	40

4	Methodology	43
4.1	Proposed Ray-Tracing Tool	43
4.1.1	First Stage: the Validation and Conversion of the Input Data	43
4.1.2	Second Stage: the Propagation Engine	44
4.1.3	Applied Accelerating Methods in the Second Stage	47
4.1.4	Fourth Stage: Post-processing	49
4.2	RT-based Framework	49
4.2.1	The RT-based Framework for MAC-abstraction	49
4.2.2	The Framework for the Map-based RT Simulation	50
4.3	mmWave Sounding Equipment	51
5	Deployments	53
5.1	mmWave Cellular Networks	53
5.1.1	Idealized Manhattan Grid with the Open Square	53
5.1.2	Idealized Manhattan Grid Scenario Without the Open Square	55
5.1.3	Map-based Manhattan Grid Topology	55
5.2	The mmWave Backhaul Links	55
5.3	The mmWave Network Deployment for Drone Detection	56
5.4	mmWave Urban Vehicular Links	58
6	Results	61
6.1	The Power Contribution of the Diffuse Scattering	61
6.2	The RT Methodology for the Massive Simulation of Manhattan Island	62
6.3	Drone Detection Assistance with mmWave Networks	65
6.4	Interference Analysis	66
6.5	The Capacity Gain of Dual-Polarized Antenna in Environment with Diffuse Scattering	68
6.6	The Impact of the Input Data Quality on the RT Simulations	70
6.7	Wave Propagation in Urban Deployment with Vehicular Blockage	72
7	Conclusion	77
7.1	Summary of Completed Work	77

7.2	The RT in 5G mmWave	78
7.3	Potential Improvements of the RT	79
	References	81

List of Figures

1.1	Ericsson forecast on the global cellular data traffic, Nov.2018 [1]. . .	22
3.1	GO propagation geometry	32
3.2	Propagation properties of GTD	33
3.3	Astigmatic ray tube.	36
3.4	RT propagation principles	38
4.1	Propagation engine employed in the proposed RT tool.	45
4.2	Comparison of computational time versus different accelerating techniques in Matlab. Simulated scenario is urban topology with square buildings.	48
4.3	A block-diagrams of the two utilized RT-based frameworks.	50
4.4	28/60 GHz sounding equipment (modified from [94]).	51
5.1	Manhattan grid mmWave cellular deployments	54
5.2	mmWave Backhaul Link Deployment (modified from [115]).	56
5.3	Block-diagram of the mWave networks assistance to detect the violating drones (modified from [118]).	57
5.4	Street-canyon urban deployment with vehicular blockage [94].	58
5.5	Deployment for in-depth analysis of transmission through the vehicular cabin [94].	59
6.1	CDFs of the total received power [107].	62
6.2	Omnidirectional path loss [101].	63

6.3	LOS probability [101].	64
6.4	The total received power difference between 3D and 2D RT results [101].	64
6.5	The reflectivity of the small unloaded drone (left image) and large loaded drone (right image) [118].	65
6.6	The mean number of the mmWave BSs detected the violating drone [118].	66
6.7	CDFs of the total received power [103].	67
6.8	Mean SINR as a function of HPBW and ISD [103].	68
6.9	The capacity gain as a function of ISD and the level of the diffuse scattering [123].	69
6.10	Comparison of measured versus simulated (green points) PADP [115].	71
6.11	Comparison between PDPs obtained by measurement and by RT- simulations of simple and accurate scenarios [115].	72
6.12	Propagation paths in the Scenario 1 [94].	73
6.13	Comparison between measured and simulated transmission through cabin [94].	74
6.14	Comparison of measured and simulated PADPs (modified from [94]).	75

List of Tables

2.1	Comparison of channel models	28
5.1	Utilized physical properties	59
6.1	Comparison with 3GPP parameters [101].	63
6.2	Comparison between simple and accurate Models [115].	71

6.3 Measurement results of excess loss for different propagation mechanisms in an urban street canyon [94]. 73

ABBREVIATIONS

3GPP	3rd Generation Partnership Project
AS	Angular Spread
BS	Base Station
CDF	Cumulative Distribution Function
CIR	Channel Impulse Response
CPU	Central Processing Unit
CUDA	Compute Unified Driver Architecture
DS	Delay Spread
EM	Electromagnetic
GO	Geometrical Optics
GPU	Graphics Processing Unit
GTD	Geometrical Theory of Diffraction
HPBW	Half Power Beam Width
INR	Interference-to-Noise Ratio
ISD	Inter-Site Distance
ITU-R	International Telecommunication Union Radiocommunication Sector
LOS	Line-of-Sight
LTE	Long-Term Evolution Systems
MAC	Medium Access Control
MIMO	Multi-Input and Multi-Output

mmWave	Millimeter-Wave Frequency Spectrum
MPC	Multipath Component
NLOS	Non Line-of-Sight
NR	New Radio
PADP	Power Angular Delay Profile
PDP	Power Delay Profile
PHY	Physical Layer
PL	Pathloss
RL	Ray Launching
RT	Ray Tracing
RX	Receiver
SINR	Signal-to-Interference-plus-Noise Ratio
TX	Transmitter
UE	User Equipment
UTD	Uniform Theory of Diffraction
uWave	Microwave Frequency Spectrum
V2V	Vehicular-to-Vehicular Communication
XPR	Cross-Polarization Ratio

ORIGINAL PUBLICATIONS

- Publication I D. Solomitckii, Q. C. Li, T. Balercia, C. R. da Silva, S. Talwar, S. Andreev and Y. Koucheryavy. Characterizing the Impact of Diffuse Scattering in Urban Millimeter-Wave Deployments. *IEEE Wireless Communications Letters* 5.4 (2016), 432–435. DOI: 10.1109/LWC.2016.2580669.
- Publication II V. Semkin, D. Solomitckii, R. Naderpour, S. Andreev, Y. Koucheryavy and A. V. Räsänen. Characterization of radio links at 60 GHz using simple geometrical and highly accurate 3-D models. *IEEE Transactions on Vehicular Technology* 66.6 (2016), 4647–4656. DOI: 10.1109/TVT.2016.2617919.
- Publication III D. Solomitckii, M. Gapeyenko, S. Szyszkowicz, S. Andreev, H. Yanikomeroglu and Y. Koucheryavy. Toward massive ray-based simulations of mmWave small cells on open urban maps. *IEEE Antennas and Wireless Propagation Letters* 16 (2016), 1435–1438. DOI: 10.1109/LAWP.2016.2641339.
- Publication IV D. Solomitckii, V. Petrov, H. Nikopour, M. Akdeniz, O. Orhan, N. Himayat, S. Talwar, S. Andreev and Y. Koucheryavy. Detailed interference analysis in dense mmWave systems employing dual-polarized antennas. *IEEE Globecom Workshops (GC Wkshps)*. 2017. DOI: 10.1109/GLOCOMW.2017.8269040.
- Publication V D. Solomitckii, M. Gapeyenko, V. Semkin, S. Andreev and Y. Koucheryavy. Technologies for efficient amateur drone detection in 5G millimeter-wave cellular infrastructure. *IEEE Communications Magazine* 56.1 (2018), 43–50. DOI: 10.1109/MCOM.2017.1700450.

- Publication VI D. Solomitckii, V. Petrov, H. Nikopour, M. Akdeniz, O. Orhan, N. Himayat, S. Talwar, S. Andreev and Y. Koucheryavy. Ray-Based Evaluation of Dual-Polarized MIMO in (Ultra-) Dense Millimeter-Wave Urban Deployments. *IEEE 87th Vehicular Technology Conference (VTC Spring)*. 2018. DOI: 10.1109/VTCSpring.2018.8417788.
- Publication VII D. Solomitckii, V. Semkin, A. Karttunen, V. Petrov, S. Nguyen, H. Nikopour, K. Haneda, S. Andreev, S. Talwar and Y. Koucheryavy. Characterizing Radio Wave Propagation in Urban Street Canyon with Vehicular Blockage at 28 GHz. *IEEE Transaction on Vehicular Technologies* (2019). Accepted, to appear.

Author's contribution

All the publications comprising this thesis were written in the Electrical Engineering Unit of Tampere University (TAU) and formerly Department of Electronics and Communications Engineering of Tampere University of Technology (TUT), Finland.

1. "Characterizing the Impact of Diffuse Scattering in Urban Millimeter-Wave Deployments".

The Intel team proposed the problem. The author developed a methodology and performed the modelling results shown in the paper. Other participants contributed to the compilation of the paper's structure and writing the text.

2. "Characterization of Radio Links at 60 GHz Using Simple Geometrical and Highly Accurate 3-D Models".

The idea of this project was proposed by Dr. V. Semkin. All the channel measurements were carried out by the team from Aalto University. Dr. Semkin was responsible for creating the 3D models, as well as writing the manuscript. The author's contribution focused on the channel modelling, the explanation of the underlying propagation mechanisms, and writing the paper.

3. **"Toward Massive Ray-based Simulations of mmWave Small Cells on Open Urban Maps".**

The idea of this paper was proposed and discussed in detail by all the participants. The author developed the methodology, performed the modelling, and plotted the figures. The efficient algorithm of BS placement developed by Adj. Prof. S. Szyszkowicz is utilized as a part of the methodology.

4. **"Detailed Interference Analysis in Dense mmWave Systems Employing Dual-Polarized Antennas".**

The idea was proposed by the Intel group. The author was engaged in the development and implementation of the methodology, as well as obtaining all the results available in the article. V. Petrov contributed significantly to the structure of the paper, as well as in writing the text.

5. **"Technologies for Efficient Amateur Drone Detection in 5G Millimeter-wave Cellular Infrastructure".**

The main idea is developed by the author with significant contributions from all the participants. The author developed the methodology and produced Fig. 2 - Fig. 5.

6. **"Ray-Based Evaluation of Dual-Polarized MIMO in (Ultra-) Dense Millimeter-Wave Urban Deployments".**

The idea was proposed by the Intel group. The author adapted the methodology developed earlier, and obtained all the results available in the paper. V. Petrov contributed crucially to the structure of the article, as well as writing the text.

7. **"Characterizing Radio Wave Propagation in Urban Street Canyon with Vehicular Blockage at 28 GHz".**

This article is the result of the well-coordinated work of the groups from Aalto and Tampere Universities. The idea belongs to Dr. Vasili Semkin. He was engaged in the channel sounding part, and with Prof. K. Haneda approved the final results. The author was responsible for the modelling part, using the methodology developed earlier by himself. Additionally, the author actively participated in writing the manuscript.

1 INTRODUCTION

1.1 Research Motivation

Over the past ten years, our society has experienced an explosive increase in the number of mobile devices and global cellular data traffic, primarily due to the popularization of multimedia and high data-rate application (see Fig. 1.1). Being an inherent part of daily life, social networks, video/audio resources and telecommunication services account for most of this traffic. According to the recent Ericsson report [1] the monthly mobile traffic rose by 88 % between Q4 2017 and Q4 2018, although even this is not the highest recorded rise, which was 89% registered in Q2 of 2013. Also, 220 million new subscribers were added to the mobile network in Q4 last year, bringing the total number of mobile phones up to 5.9 billion representing a 15% year on year increase. The Cisco Global Mobile Data Traffic Forecast [2] predicts 77 exabytes (77×10^{18} bytes) of global mobile data traffic per month by 2022, 90% of which will be due to smartphones. Video traffic will rise ninefold, and will account for four-fifths of the world's mobile data traffic by 2022.

This growing trend in mobile data volume is continuously eating up the available bandwidth in the microwave (uWave) frequency band, which is already thoroughly exploited by the existing wireless networks. Thus, the millimeter-wave (mmWave) spectrum was introduced as part of the 5G wireless technologies [3] to resolve this issue. This frequency range employs 45 GHz of the available bandwidth, which is more than $10\times$ higher than what is available in the <6 GHz spectrum [4], [5]. As a result, mmWave networks have the potential to improve the throughput per area over Long-Term Evolution Systems (LTE) [6] by as much as a thousand times. In view of this, in 2014 Samsung had already demonstrated technologies capable of transmitting 7.5 Gbps [7] at 28 GHz, demonstrating the feasibility of future 5G networks. Further proof of their feasibility soon followed. Using NI mmWave equipment, Nokia achieved 10 Gbps over the air at 73 GHz in 2015 [8]. The recent

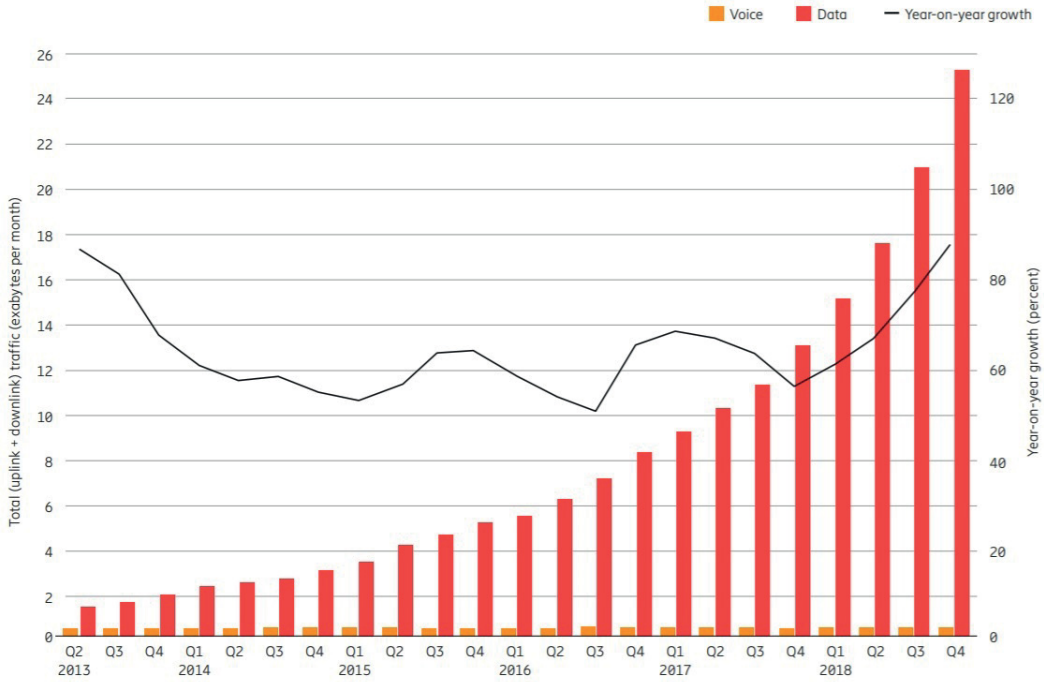


Figure 1.1 Ericsson forecast on the global cellular data traffic, Nov.2018 [1].

collaboration of Mitsubishi Electric Corporation and NTT DOCOMO resulted in 25 Gbps throughput via one mobile terminal at 28 GHz [9]. Finally, the partnership between Samsung, Qualcomm and Verizon led to the successful demonstration of the 1.7 Gbps mmWave system, meeting the 5G New Radio (5G NR) specifications [10].

Despite these successes, the mmWave spectrum poses unique challenges [11] that are not usually encountered with the uWave band. First, the propagation of the mmWave signal experiences high free-space pathloss (PL), as well as significant atmospheric and precipitation attenuation, all of which shrink the coverage radius to below a few hundred meters [12]. Moreover, the contribution of diffraction and transmission through typical brick or concrete wall (typical building materials) is negligible [13]. In practice, this means that the signal strength at a receiving device located just around the corner from an mmWave transmitter may be below the noise level, even if it is only few away far from the transmitter. Finally, because the wavelength is less than a centimetre on the mmWave band, there are more electrically large objects that can contribute to multipath propagation, and this causes a notice-

able difference to the mmWave band channel properties compared to uWave [14]. On the other hand, the wavelength factor has led to the emergence of compact directional antennas, whose physical features and position [15] affect the quality and uniqueness of a wireless channel. Finally, the guidance of the signal in a particular direction by a high-gain antenna improves the total interference picture [16] and channel security [17], which is a distinguishing feature against the dipole antenna. To evaluate the performance of mmWave 5G networks, comprehensive methods which consider essential mmWave 5G features such as the antenna array or multiple-input and multiple-output (MIMO) systems are required. Although academia and industry have already proposed several mmWave 5G models [5], a number of mmWave-related issues about diffuse scattering and depolarization remain unresolved. Moreover, it is poorly studied yet to what extent the mentioned phenomena and features affect the basic communication parameters, such as throughput, for instance, in different environmental conditions. However, maximizing of the throughput exactly what the mmWave 5G basic goal is.

1.2 Main Contribution and Scope

This thesis focuses on an ray tracing (RT) methodology, enabling efficient evaluation of mmWave 5G networks. The main contributions of this thesis are as follows:

1. The development and utilization of the RT-based methodology for the massive simulation of 5G mmWave networks.
2. A demonstration and evaluation of the photogrammetry method to capture accurate 3D models for the RT simulation.
3. An assessment of the impact of diffuse scattering on mmWave 5G networks.
4. The characterization of noise- and interference-limited mmWave 5G networks.

1.3 Structure of the Thesis

This thesis consists of seven chapters based on a compilation of seven publications. Chapter 1 familiarizes the reader with the research motivation, the main contribution and the structure of the thesis. Chapter 2 explains wireless channel properties,

while Chapter 3 clarifies the background of channel simulators, classical electromagnetism and ray-optic fields. This section also discusses the advantages and drawbacks of RT methods, and identifies a list of tasks for which its use is urgently required. The RT-based methodology is explained in Section 4, while the deployment of interest are demonstrated in Chapter 5. The results obtained by the RT-based methodology and the aforesaid deployments are presented in Chapter 6. Finally, Chapter 7 summarises the work done and discusses the future plans for the proposed RT.

2 WIRELESS CHANNEL AND MODELS

2.1 Wireless Channel Properties

A wireless channel is a medium in which a signal propagates from the transmitter (TX) to the receiver (RX). The geometrical and physical heterogeneity of this environment forms multipath components (MPCs), wherein the emitted signal arrives at RX with some delay and angular spread. Assuming there is a directive channel on both the TX and RX sides, this phenomenon can be expressed by the double-directional channel impulse response (CIR) as follows [18]:

$$h(\tau, \Omega^{\text{RX}}, \Omega^{\text{TX}}) = \sum_{n=1}^N a_n e^{-j\phi_n} \delta(\tau - \tau_n) \delta(\Omega^{\text{RX}} - \Omega_n^{\text{RX}}) \delta(\Omega^{\text{TX}} - \Omega_n^{\text{TX}}), \quad (2.1)$$

where $\Omega_n^{\text{TX}} = [\phi^{\text{TX}} \ \theta^{\text{TX}}]$ and $\Omega_n^{\text{RX}} = [\phi_n^{\text{RX}} \ \theta_n^{\text{RX}}]$ denote the direction of the transmitted and received signals respectively, and a_n , ϕ_n and τ_n designate the amplitude, phase and delay of the n^{th} MPC. When the TX behaves as an omnidirectional antenna, then the delta function of Ω_n^{TX} might be removed. In practice, instead of using two parameters of an MPC such as magnitude and phase, it is more convenient to apply the power metric, which is squared absolute value of a complex signal. Following this, the power delay profile (PDP) is the is squared absolute value of a CIR. Furthermore, any MPC arriving at an RX may produce small-scale fading due to constructive or destructive interference, resulting in variations in the amplitude and phase of the CIR. However, further averaging of the PDP may smooth out these splashes of interference as follows:

$$PDP(\tau, \Omega^{\text{RX}}, \Omega^{\text{TX}}) = \frac{1}{M} \sum_{m=1}^M |h(\tau, \Omega^{\text{RX}}, \Omega^{\text{TX}})|^2, \quad (2.2)$$

where M is the number of CIR samples. The synthetic omnidirectional (PDP) is then obtained as follows:

$$PDP(\tau) = \frac{1}{K} \frac{1}{N} \sum_{k=1}^K \sum_{n=1}^N PDP(\tau, \Omega^{\text{RX}}, \Omega^{\text{TX}}), \quad (2.3)$$

where K and N is the number of TX and RX scan steps.

Furthermore, a list of essential metrics used for channel characterization may be derived from the PDP. First, the total received power is an integral ¹ over the PDP function above the noise floor. Second, the difference between the transmitted power and the total received power is the pathloss (PL). The set of aggregated PDPs obtained in a specific angular range (e.g. $-90^\circ \dots +90^\circ$) forms the power angular delay profile (PADP). In addition, the delay spread (DS) of the arriving MPCs may be characterized using the following formula [18]:

$$\tau_{\text{RMS}} = \sqrt{\frac{\int_{-\infty}^{\infty} (\tau - \tau_m)^2 \text{PDP}(\tau) d\tau}{\int \text{PDP}(\tau) d\tau}}, \quad (2.4)$$

here τ_m is mean delay specified in [18]. Another important parameter, describing the angular spread (AS) of the arriving MPCs is [18]:

$$\phi_{\text{RMS}} = \sqrt{\frac{\int |e^{j\phi} - \mu_\phi|^2 \text{PAS}(\phi) d\phi}{\int \text{PAS}(\phi) d\phi}}, \quad (2.5)$$

where APS is the angular power spectrum and μ_ϕ denotes the average angle explained in [18].

A signal propagating in a heterogeneous medium experiences intermediate interactions with any surrounding objects resulting in the depolarization effect. It is this mechanism that enables the energy coupling between two orthogonal orientations of an antenna system. Therefore, the cross-polarization ratio (XPR) shows the ratio between the copolarized and cross-polarized components of the received signal [19]:

$$\text{XPR} = 20 \log_{10} \left(\frac{|E^{\text{copol}}|}{|E^{\text{xpol}}|} \right). \quad (2.6)$$

This metric is widely exploited to evaluate polarization losses and polarization diversity, as well as in the design of dual-polarized antenna systems.

The line-of-sight (LOS) probability specifies the chances of establishing a direct link between TX and RX in a particular scenario. This property has a purely geometrical nature and does not relate to any of the physical mechanisms. At the same time, the ratio between the LOS and non-LOS (NLOS) powers specifies the Rician K-factor.

¹The sum replaces the integral sign when PDP has a discrete (performed by delta-function) form.

2.2 Channel Models and Simulators

2.2.1 Classification of Channel Models

The design of any mmWave TX/RX system starts with an investigation of the wireless channel through the parameters mentioned in Sec. 2.1. There are two approaches to doing that, measurements and modelling. Due to the high cost and weight of the measuring apparatus, as well as the limitations imposed by humidity, temperature and vibration, it is difficult to carry out complete physical measurements. Therefore, modelling comes into play, and the following sections are devoted to this method.

Despite previous efforts [20] and [21] to classify available channel models precisely, it is not an easy task, since there are so many classification criteria that can be applied. For example, models can be categorized as narrow- and wide-band, time-variant and time-invariant, stationary and non-stationary and in many other ways [22]. However, the most comprehensible division might be realized through original formation principles. Such a criterion establishes four types of channel models, namely empirical, analytical (or stochastic), deterministic [23], [24] and hybrid. The first type represents the mathematical interpolation of the measured data by exponential, linear or polynomial functions. A typical example of this is the parametrized linear function fitting the measured PL data points [25]. The second type, the analytical/stochastic model, is described by more advanced math related to probabilistic formulas and distribution functions. Usually, such models characterize the angular and temporal behavior of a wireless channel [26] in a certain deployment (e.g. urban, indoor, outdoor-to-indoor).

Deterministic electromagnetic (EM) simulation [27] yields the most accurate results for site-specific conditions. However, the overall precision of this method depends on the quality of the input data, as well as the number and performance of the built-in physics-calculating functions. Unlike the analytical model, which is trained on a specific deployment, the deterministic simulation is more versatile and supports any of scenarios, with any distribution of objects in it. Unfortunately, for the relatively highest accuracy and versatility we have to pay the long calculation time among all other types of models (see Table 2.1). Finally, the hybrid approach [28] combines elements of some of the above-mentioned methods. This mix can compensate for the drawbacks and gain from the positive qualities of the hybrid model

Table 2.1 Comparison of channel models

Parameter	Accuracy	Calculation Time	Complexity
Empirical	Low	Very Low	Low
Analytical/Stochastic	Medium	Low	Medium
Deterministic	High	Very high	High

as a whole. A good example of the hybrid model is demonstrated in [29] and in [30].

Within this thesis, the concepts of "*tool/simulator*" and "*model*" should be clearly specified. A "model" represents the mathematical interpretation of a single process. A tool or simulator usually encompasses single or multiple models and provides user-friendly capabilities to manage them.

2.2.2 Overview of the mmWave Channel Models and Simulators

Nowadays both industry and academically driven projects such as METIS [31], MiWEBA [32], NYU WIRELESS [33]–[35] and mmMagic [36] propose mostly analytical and empirical 5G mmWave channel models and simulators, which are therefore de facto the most commonly used. Nevertheless, a number of popular simulators have been created by academic groups working on their own. For example, QuaDRiGa (QUAsi Deterministic RadIochannel GenerAtor) was developed for the evaluation of indoor and outdoor MIMO channels, as well as satellite-based scenarios [37] at 10, 28, 43, 60 and 82 GHz. Sharing some common features with SCM [38] and WINNER [39] QuaDRiGa facilitates multilink tracking of RXs in a 3D mobile environment. The measurement-based statistical channel simulator SIRCIM (Simulation of Indoor Radio Channel Impulse Response Models) was originally designed for the investigation of early stage WiFi, but SMRCIM extends it to outdoor scenarios as well. Both of them these are capable of generating CIRs for frequencies of up to 60 GHz. The exhaustive wideband channel sounding at 28 to 73 GHz results in the NYUSIM [40] simulator which supports rural and urban outdoor environments. Finally, the wireless channel simulator proposed in [41] focuses on the performance analysis and verification for machine-to-machine (M2M) and Internet of Things (IoT) industrial applications. It delivers the basic CIR properties and may support orthogonal frequency-division multiplexing (OFDM) transmission.

Due to the continuous reduction in computational costs [42], as well as the emergence of new accelerating hardware [43], the interest in RT-based deterministic meth-

ods has intensified. Today, academia and industry are constantly trying to find fast, flexible and accurate RT-based methods capable of supporting the essential features of mmWave 5G [44]–[46]. There are a number of commercially available RTs on the market, several examples of which are briefly described below.

Wireless Insite from Remcom [47] is the most popular tool, supporting frequencies up to 100 GHz. Built-in empirical and deterministic models accelerated by the graphics processing unit (GPU) and multi-threaded central processing unit (CPU) may resolve a comprehensive list of propagation tasks. Models of the diffuse scattering [48] and 5G MIMO [49] have recently been introduced.

WinProp from Altair HyperWorks [50] supports standard RT, Intelligent Ray Tracing (IRT) and Dominant Path (DPM) models at frequencies up to 75 GHz. Besides the static deployment, Winprop may simulate the spatial variability of the objects in the scene, which is vital for the study of vehicular communication in 5G.

Ranplan Professional [51] supports simulations from 100 MHz to 70 GHz in both indoor and outdoor deployments. 3D-to-2D dimension reduction, space partitioning, and hybrid RT reduce the total computational time. An extensive material database for frequencies up to 60 GHz makes the tool versatile and easy to utilize.

Atoll from Forsk [52] performs on a <6 GHz and >6 GHz frequency spectrum. It employs multi-threaded CPU-based acceleration techniques for RT. On top of that, Atoll proposes non-standard approaches to the issues of absorption in vegetation, rain and atmospherics.

Besides RT, there are deterministic full-wave methods which also look attractive due to their high accuracy. Such methods utilise the method of moments (MoM), finite difference time domain (FDTD), finite element method (FEM) and finite integral techniques (FIT). All of these approaches provide a numerical solution consisting of Maxwell equations in both differential or integral and time or frequency forms [53]. However, they all use a common preprocessing stage based on triangulation, i.e. the fragmentation of surfaces into polygonal primitives called facets, whose sizes have to meet the $10/\lambda \dots 20/\lambda$ criterion [54]. This means that it is impractical to simulate large scenarios with these full-wave methods as the computational time required to process such densely triangulated grids is unsustainable. As a result, to date, MoM, FDTD, FEM, FIT and some other similar methods have typically focused on the calculation of antenna patterns, radar cross-sections, emissions and a number of other parameters. Full-wave methods can be found in commercial soft-

ware such as Ansys HFSS [55], CST Microwave [56], EMPro [57] and SEMCAD [58] among others.

It should be noted that commercial and academic simulators have different roles. The tools developed for academic projects are aimed at testing new ideas, use cases and models, and as such they are pioneers in their field. Commercial simulators, on the other hand, tend to offer convenient and efficient solutions to commonly encountered problems. Trying to solve a non-standard task with a commercial simulator usually poses significant challenges. Therefore, both types of simulators are needed as they serve different purposes.

3 THE BACKGROUND TO RAY-TRACING

3.1 Ray Field Theory

Mathematically, an EM field can be illustrated in different ways in order to distinguish its particular properties and capabilities. Thus, the following section explains how the ‘rays’ appear, and why they are so easy to utilize and therefore crucial in modelling wireless channels.

3.1.1 Geometrical Optics

Geometrical optics (GO) is a high-frequency approximation that can specify the EM waves in discrete form. Here the term ‘high frequency’ means that the wavelength is considerably smaller than the linear size of the interacting objects [59]. Thus, it does not in any way relate to the carrier frequency of the oscillating wave specified by Hz or $\frac{Rad}{s}$. Furthermore, GO performs EM radiation, travelling along a line¹ from the source to the destination perpendicular to the wavefront and parallel to the wave vector [60]. This concept relies on Fermat’s principle, which states that *in a homogeneous medium the path taken by a ray of light between two points is the path that can be traversed in the least time* [61]. This principle has several useful consequences, the most important of which is that these rays are mutually independent. As will be shown later, this property significantly extends GO’s capabilities.

The GO theory describes two basic physical phenomena, reflection from a specular surface (path TX-RX1 in Fig. 3.1a) and transmission across a medium (path TX-RX2 in Fig. 3.1a). The geometry of the first mechanism follows the rule that the incident angle of impinging EM radiation is equal to the reflection angle, i.e. $\theta_i = \theta_r$. In turn, the transmission mechanism satisfies Snell’s law, which connects

¹Based on the observation of photons

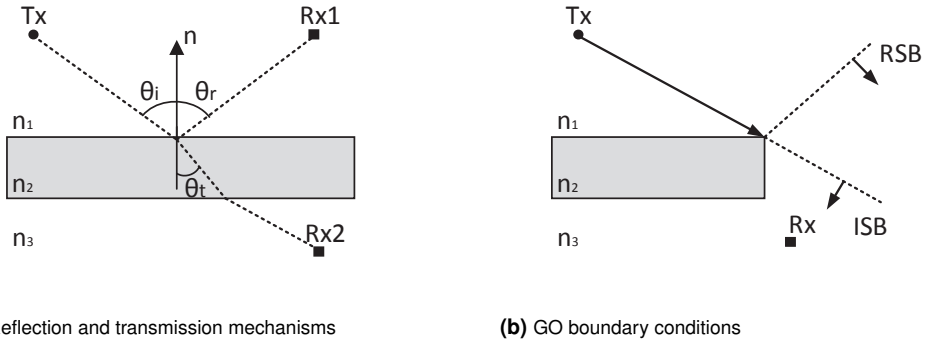
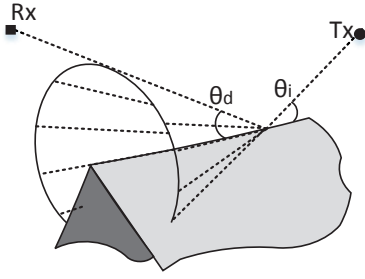


Figure 3.1 GO propagation geometry

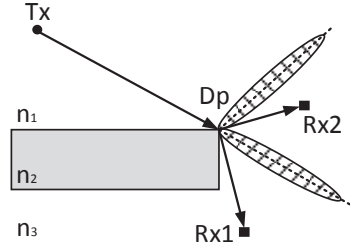
the propagation geometry of a ray to the refractive indices (n_1 and n_2 in Fig. 3.1a) of the medium, i.e. $\sin(\theta_i)n_1 = \sin(\theta_t)n_2$. However, these reflection and transmission mechanisms are not enough to characterize the EM field in the Incident Shadow (ISB) and Reflected Shadow (RSB) boundaries shown in Fig. 3.1b. In particular, if the RX is located behind a non-transmitting metallic object (the RX is in the shadow region), then the GO ray is unable to reach it. Such a context also conflicts with the fact that an EM field is monotonous and does not have any spatial discontinuities [62]. Another issue is that classic GO theory does not introduce wave behavior, and thus wavelength as it is, so this limits the investigation of interference processes on the RX. Moreover, vector amplitude and therefore, polarization, are not specified in the GO theory either [63]. In the light of these facts, the use of GO should be enhanced to be able to solve the problem in the shadow regions and account for the wave behavior of an EM.

3.1.2 Geometrical/Uniform Theory of Diffraction

To improve GO's performance in the shadow regions, J. Keller has proposed the Geometrical Theory of Diffraction (GTD) [64]. When a ray impinges on a wedge, a corner, a vertex, a tip or a curved surface it produces secondary diffraction rays in the shape of a Keller cone (see Fig. 3.2a), when $\theta_i = \theta_d$ (practical realization might be found in Sec. 4.1.2). Such a notion facilitates the propagation of the EM field around an obstacle (see the path TX-RX1 in Fig. 3.2b) by bending at the Dp point. As a result, besides the direct, incident, reflected and transmitted rays, GTD also



(a) Keller's cone and secondary diffracted rays



(b) Discontinuities of GTD (hashed).

Figure 3.2 Propagation properties of GTD

invokes the independent existence and propagation of diffracted rays. More detailed information about GTD equations can be found in [64].

However, being based on ray-optical theory, GTD still produces regions where no solution can be obtained. These regions are adjacent to the RSB and ISB, but are smaller in area (see the hashed zones in Fig. 3.2b). These discontinuities have been resolved by the Uniform Theory of Diffraction (UTD) proposed by R. Kouyoumjian and P. Pathak in [65]. The underlying idea behind this theory relies on the transition function, whose multiplication with the GTD coefficients makes the field continuous and smooth ² throughout.

3.1.3 Electromagnetic Theory

As well as the discrete GO approach, there is also the classical theory of electromagnetism which describes the EM field as seamless. This is based on four differential equations derived by J. Maxwell. The phasor or time-harmonic form of the EM field in a homogeneous lossless medium is specified as [66]:

²Hereafter referred as 'uniform'.

$$\nabla \times \mathbf{E}(\mathbf{r}, \omega) = -j\omega\mu\mathbf{H}(\mathbf{r}, \omega), \quad (3.1)$$

$$\nabla \times \mathbf{H}(\mathbf{r}, \omega) = j\omega\epsilon\mathbf{E}(\mathbf{r}, \omega), \quad (3.2)$$

$$\nabla \cdot \mathbf{E}(\mathbf{r}, \omega) = 0, \quad (3.3)$$

$$\nabla \cdot \mathbf{H}(\mathbf{r}, \omega) = 0. \quad (3.4)$$

Vectors \mathbf{E} and \mathbf{H} in equations (3.1) - (3.4) denote the electrical and magnetic fields. The dielectric permittivity, $\epsilon = \epsilon_0\epsilon_r$, and permeability, $\mu = \mu_0\mu_r$, characterize the physical properties of the propagating medium with respect to free space. Specifically, $\epsilon_0 = 8.8542 \times 10^{-12}$ F/m and $\mu_0 = 4\pi \times 10^{-7}$ H/m. In the case of a lossy medium, ϵ becomes complex, due to the non-zero conductivity, σ , so that $\epsilon_c = \epsilon - j\sigma/\omega$. Also, it is highly important to note that the dielectric permittivity depends on the refractive index is as follows: $n = \sqrt{\epsilon_r\mu_r}$. Finally, the radius vector, \mathbf{r} , specifies the spatial coordinate, while ω is the angular frequency of the continuously oscillating wave.

Taking the curl of (3.2) and then substituting it with (3.1) gives the vector Helmholtz equation as:

$$\nabla^2 \times \mathbf{E}(\mathbf{r}, \omega) + k^2\mathbf{E}(\mathbf{r}, \omega) = 0, \quad (3.5)$$

where $k = k' - jk'' = \omega\sqrt{\mu\epsilon}$ is the wave number. This equation is utilized to derive the EM fields through the high-frequency asymptotic solution described in the next section. However, the straightforward application of electromagnetic theory to solve real-life problems seems to be extremely challenging [63].

3.1.4 High-frequency Asymptotic Solution of Electromagnetic Fields

In order to supply the GO with wave and polarization properties, as well as to observe the behavior of an EM field at distances far from its source, and to extend the Sommerfeld-Runge ansatz [67], Luneberg and Kline proposed the high-frequency asymptotic solution of electromagnetic fields [68], [69] as follows:

$$\mathbf{E}(\mathbf{r}, \omega) \sim e^{-jk\phi(r)} \sum_{n=0}^{\infty} \frac{E_n(r)}{(j\omega)^n}, \quad (3.6)$$

$$\mathbf{H}(\mathbf{r}, \omega) \sim e^{-jk\phi(r)} \sum_{n=0}^{\infty} \frac{H_n(r)}{(j\omega)^n}, \quad (3.7)$$

where $\phi(r)$ represents so-called eikonal function [70] and the symbol " \sim " means equality in the asymptotic sense. Since, the plane wave solutions are not physically possible in an inhomogeneous medium (μ and ϵ are constant in Eq. 3.1 and Eq. 3.2) because the variation in refractive index in the direction of propagation will bend the wave, the eikonal function is introduced. This function assumes the variation of phase in a inhomogeneous media, where $n(r)$. More detailed information about the derivation of the eikonal function can be found in [71]. Expressed through (3.6) and (3.7) an EM field is called a *ray-optic field* or *ray field*, whose asymptotic solutions become more accurate as soon as ω , and, subsequently, k increases³ [59]. Moreover, it encompasses the classical GO field as soon as $\omega \rightarrow \infty$.

The substitution of the Luneberg-Kline series (3.6) into the vector Helmholtz equation (3.5) derives the important eikonal $|\nabla\phi(r)|^2 = n^2$ and transport $2(\nabla\phi \cdot \nabla)E_0 + (\nabla^2\phi)E_0 = 0$ equations which link wave and geometrical optics theories. The first equation specifies the spatial properties of a wavefront, while the second one characterizes the transfer of energy.

Mathematical manipulations with these equations reveal the underlying physical and geometrical properties of the ray-fields. The most important of these are listed below.

1. In a homogeneous medium EM energy flows along straight lines, from source to destination point. The direction of that flow is defined as $\mathbf{e} = \nabla\phi/|\nabla\phi|$.
2. A group of rays adjacent (solid lines) to the axial (dashed line) ray form an *astigmatic ray tube* [72] as shown in Fig. 3.3.
3. The orientations of \mathbf{E} and \mathbf{H} remain unchanged in a homogeneous medium. Conversely, \mathbf{E} , \mathbf{H} and \mathbf{e} change an orientation in a heterogeneous one due to propagation mechanisms.

³This fact explains the better accuracy of RT on higher frequencies

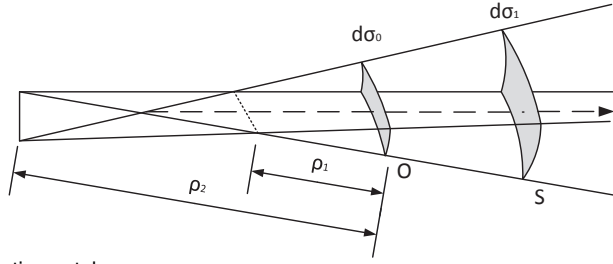


Figure 3.3 Astigmatic ray tube.

4. For a medium with admittance Z , the real power is calculated as $Z|E_0|^2(\nabla\psi)$.
5. The magnitude of the total field at a particular observation point is the sum of all direct, reflected, transmitted and diffracted ray-optic fields passing across it.
6. A ray with the initial phase $\psi(0)$ has the phase equal to $e^{-jk\psi(s)} = e^{-jk\psi(0)}e^{-jks}$ on a distance s .
7. Attenuation of the ray-optic amplitude at the observation distance s is expressed by the under square root spreading factor as follows:

$$E(s) = |E_0(0)| \sqrt{\frac{\rho_1 \rho_2}{(\rho_1 + s)(\rho_2 + s)}} e^{-jks}. \quad (3.8)$$

More precisely, the decay rate is inversely proportional to the square $d\sigma$ (see Fig. 3.3) specified by the curvatures ρ_1 and ρ_2 of the wave front.

As a result, it becomes possible to consider an EM field with wave properties from the perspective of GO and the GTD. Namely, it emerges the concepts of polarization and wavelength, while the field remains monotonic even in the shadow regions. Finally, it becomes feasible to solve applied and scientific problems in heterogeneous conditions, as well as when the receiver and transmitter are sufficiently remote from each other.

3.2 The Practical Implementation of a Ray Field

The next section is devoted to the practical implementation of ray field theory using modern computational approaches.

3.2.1 Propagation Geometry Models

Traditionally, RT has accounted for the reflectivity of objects in a 3D scene with graphical computing [73]. Imitating the behavior of a photon in such RT conforms to GO principles, which makes it possible to extend its use to the modelling of wireless channels as well. Nowadays, there are two basic geometrical methods (see Fig. 3.4) capable of doing this, image-based RT and Ray launching (RL)⁴.

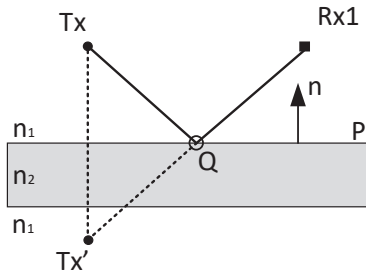
3.2.1.1 Image-based Ray Tracing

Given the locations of TX and RX, the reflected path from a flat surface can be calculated with the image method using three basic steps. First, we search for the TX image (denoted as TX' in Fig. 3.4a) relative to the reflecting plane P as $TX' = TX + 2(\mathbf{n} \cdot (v - TX))\mathbf{n}$, where \mathbf{n} is the normal of the reflecting plane P , v is any point on that plane, and TX is the initial position of the transmitter. After that, the image point TX' should be connected to RX by a line, intersecting the plane at point Q. Finally, the incident and reflected geometry of the ray follow the TX-Q-RX path. This algorithm can be extended to high-order reflections as well, simply by applying the recursive procedure. This method is reasonably accurate and highly attractive for tasks in which the precise phase (time and distance) plays a crucial role. Such tasks are related to MIMO channel, positioning and radar. However, high-order reflections result in exponential growth [18] of the computation time, which makes modelling large deployments unfeasible. Therefore, pure image-based RT is rarely used nowadays.

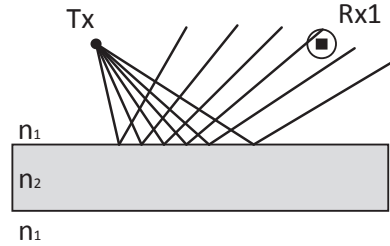
3.2.1.2 Ray-Launching

The alternative to image-based RT is the RL [74]–[76] method, which launches an enormous number of uniformly distributed test rays in all directions (shown in Fig. 3.4b). While they are travelling, these rays experience intermediate interactions with surrounding objects according to the rules of GO and UTD geometry. The propagation of a certain ray stops when it: i) intersects the receiving sphere, ii) carries power below the noise level, iii) a maximum number of ray-object intersections is reached.

⁴It is also called "shoot-and-bouncing" RT, brute-force RT, or Ray-casting.



(a) Image-based RT propagation geometry



(b) RL propagation geometry

Figure 3.4 RT propagation principles

Most of the computation time for RL is due to the density of the rays emitted by TX, while the number of scene objects and antennas does not have much impact. It is this fact that makes RL more attractive than image-based RT. On the other hand, RL has a couple of limitations associated with the discrete rays and the RX sphere [77]. First, the ray-sphere intersection test distorts the angular and temporal parameters, which limits its use mostly to coverage prediction. Moreover, the wrong balance between the ray density and the size of the RX sphere may result in two outcomes: i) some rays are unable to cross the sphere, ii) multiple similar rays cross the sphere. In the first case, it may not be possible to find a meaningful path, while the combination of two similar paths may result in an extra 3 dB of received power. There are several ways to compensate for these issues. For example, to reduce the ray divergence, additional ray densification occurs after a specified travel distance [78].

3.2.2 Acceleration Techniques

Although the RT performs better than full-wave methods in large scenes, *massive simulation* with tens or even hundreds of antennas and objects is still time-consuming. Consequently, accelerating techniques [79] are required.

The dimension reduction approach can produce a fast, but rough estimation of network coverage. It reduces the dimensions of the scene from 3D to 2D [80] or even 2.5D [81]. As a result, the computation time could be reduced by ten times, while the total accuracy remains better than that of analytical or stochastic models. Never-

theless, the output data may not yet be precise enough to plan a real communication network with variable antenna height and different-height objects.

The ray-object intersection test consumes a great deal of computational time. Therefore, the spatial division algorithm is proposed, which has the potential to improve the situation. Specifically, first it breaks the whole scenario into hierarchical sub-spaces, wrapping up the scene objects. This algorithm then efficiently filters out the sub-spaces that do not interact with the test rays and thus reduces the number of objects to be tested. Various hierarchical space-partitioning methods, such as angular sectoring [82], kD-tree, octree and quadtree [83], [84] have been proposed.

A visibility algorithm [79], [85] forms a tree, which describes the mutual visibility of the scene objects (walls, wedges, RX, TX) to each other [84]. This tree is utilized to identify the possible paths between TX and RX, taking into account the single/high-order, similar/mixed propagation mechanisms. Once the visibility data has been calculated, it can be utilized for the same site-specific deployment without the need for any further recalculation. The visibility algorithm is usually aggregated with the spatial division to optimize its performance.

Acceleration of the RT is not only achieved at the level of algorithms. Video cards whose purpose is to process millions of graphic primitives, such as in a computer game, or some other graphical application, can also be used [46], [86]. The video card may calculate the independent processes in parallel, using multiple onboard processing cores. This conforms well to the independence principle of GO (see Sec. 3.1.1). The most popular computing platform for this purpose is CUDA (Compute Unified Driver Architecture) from NVIDIA [43] because its architecture has several software layers, offering flexible capabilities to manage the computing resources in a GPU.

Multiple clusters can be applied to parallelize the RT workflow. The framework proposed in [87], [88] consists of three primary stages: preprocessing the input data, processing the rays and post-processing the obtained results. As soon as the first stage is completed, the total workload is distributed among the clusters, enabling the parallel computation of the independent rays.

3.2.3 Physical Models

During propagation the transmitted signal interacts with surrounding objects, experiencing changes of amplitude, phase or polarization. The goal of the physical models below is to describe all these transformations according to GO and UTD methods. Thus, if a signal propagates from TX to RX located at a distance s' without any intermediate interaction with the scene objects (LOS case) the E-field at the observation point is described by the following equation:

$$E_{los} = E_0 \frac{e^{-jks'}}{s'}, \quad (3.9)$$

where E_0 is initial E-field and k is the wave vector. When a signal impinges on a flat surface (e.g. the wall of a building) the reflected field is represented by the following equations [59]:

$$E_r = \begin{bmatrix} E_i^{\parallel}(Rp) \\ E_i^{\perp}(Rp) \end{bmatrix} \cdot \begin{bmatrix} R_{\parallel} & 0 \\ 0 & R_{\perp} \end{bmatrix} \cdot \frac{e^{-jks'}}{s'}, \quad (3.10)$$

$$E_t = \begin{bmatrix} E_i^{\parallel}(Tp) \\ E_i^{\perp}(Tp) \end{bmatrix} \cdot \begin{bmatrix} T_{\parallel} & 0 \\ 0 & T_{\perp} \end{bmatrix} \cdot \frac{e^{-jks'}}{s'}. \quad (3.11)$$

In Eq. (3.10) and (3.11) E_i^{\parallel} and E_i^{\perp} are vectors resolved in the ray-fixed coordinate system, s' is the distance from the reflection (Rp) or transmission (Tp) point to RX. Further, the reflection, R , and transmission, T , coefficients are as follows:

$$R_{\perp, \parallel} = \Gamma_{\perp, \parallel} \left(1 - \frac{(1 - \Gamma_{\perp, \parallel}^2) \exp(-2\alpha l) \exp(-2j\beta l) \exp(jkd \sin(\theta))}{1 - \Gamma_{\perp, \parallel}^2 \exp(-2\alpha l) \exp(-2j\beta l) \exp(jkd \sin(\theta))} \right) \quad (3.12)$$

and

$$T_{\perp, \parallel} = \frac{(1 - \Gamma_{\perp, \parallel}^2) \exp(-\alpha l) \exp(-j\beta l)}{1 - \Gamma_{\perp, \parallel}^2 \exp(-2\alpha l) \exp(-2j\beta l) \exp(jkd \sin(\theta))}. \quad (3.13)$$

In Eq. (3.12) and (3.13), θ is the angle of incidence, α and β are the propagation

coefficients specifying a lossy medium, l is the penetration distance of a ray inside the wall, and d is the gap between two adjacent rays produced by the mechanism of internal reflection. Finally, Γ_{\perp} and Γ_{\parallel} are Fresnel coefficients perpendicular and parallel to the plane of incidence. More detailed information about each of these coefficients can be found in [59].

If a signal impinges on a sharp wedge, diffraction occurs which is specified by GTD/UTD. A single-order diffracted E-field originating from a sharp wedge with zero curvature is calculated as follows [89]:

$$E_d^{UTD} = \begin{bmatrix} E_i^{\parallel}(Dp) \\ E_i^{\perp}(Dp) \end{bmatrix} \cdot D \cdot \sqrt{\frac{s}{s'(s+s')}} \cdot e^{-jk(s')}. \quad (3.14)$$

In Eq. (3.14) s is the distance from the source to the diffraction point (Dp) and s' is the distance between the diffraction point and the RX. Additionally, incident E-field is resolved in an edge-fixed coordinate system on the E_i^{\parallel} and E_i^{\perp} components. The diffraction coefficient D is 4×4 array, whose elements specify polarization properties [89].

A signal reflecting from a rough plane undergoes additional attenuation, which is represented by the roughness factor $f(\sigma_s)$. The attenuation rate depends on the angle of incidence θ , the wavelength λ , and the root-mean square of the size of the irregularity σ_s as follows [90]:

$$f(\sigma_s) = \exp(-0.5(4\pi\sigma_s \cos(\theta)/\lambda)^2). \quad (3.15)$$

In addition to the attenuated specular (coherent) signal, the rough surface produces a diffuse-scattering (incoherent) signal as well. The relation of both these components should be balanced according to the energy conservation law. Accordingly, the amplitude of the signal created by the Lambertian diffuse scattering mechanism is expressed by the following equation [91]:

$$E_s^2 = K_0^2 S^2 \frac{\Delta S \cos(\theta_i) \cos(\theta_s)}{\pi} \frac{1}{r_i^2 r_s^2}, \quad (3.16)$$

where $K_0 = \sqrt{60G_t R_t}$ and S is ratio between scattered and incident fields, varying from 0 to 1. Moreover, ΔS is the tile size, θ_i and θ_s are the incident and scattered ray angles and r_i and r_s are the TX-to-tile and tile-to-RX distance.

The models mentioned above are typical for modern RTs. Nevertheless, there are a number of other models which have the potential to improve the overall accuracy of RT. For example, ITU-R proposes models [92] for a frequency range of 1 - 100 GHz. This evaluates the signal attenuation as a function of rain rate and polarization. Furthermore, other formulas have also been proposed [93] to characterize the attenuation of a signal by foliage on frequencies up to 100 GHz.

4 METHODOLOGY

This chapter explains the proposed RT-based methodology exploited in this thesis. In addition to that, the utilized mmWave sounding equipment is described at the end of this chapter.

4.1 Proposed Ray-Tracing Tool

The RT developed during this research was designed to be a key element of the utilized methodology. The accuracy of it was validated by measurements in [94]. Architecture of the RT was divided into four independent parts so that it could be adapted to solve various mmWave 5G problems by taking into account directive antennas, roughness, and a wide range of deployments. Thus, the RT comprises an input stage, a propagation engine, and physical and post-processing stages. Depending on the task at hand, each of these parts can be adapted and fine-tuned separately to reduce the computational load. Additionally, the architecture of the RT was extended with a number of external functions which offered new capabilities for processing and optimizing the input/output data. The architecture and functions were programmed in Matlab to speed up the whole development process. Having so many built-in features and toolboxes, Matlab is undoubtedly one of the preferred programming environments for a resource-limited development environment. Further information about the RT architecture and its capabilities are described below.

4.1.1 First Stage: the Validation and Conversion of the Input Data

The input data for the RT should include four essential components, namely a 3D model of the environment, the antenna's properties and its location, and the physical parameters. The first stage of the tool preprocesses the input data into an appropriate format compatible with the requirements of the propagation engine (second stage).

The model of the 3D environment can be uploaded into the simulator in readily accessible formats such as *.STL, *.OBJ, *.SHP. It can also be created using CAD software, such as SolidWorks, PTC Creo or FreeCad, or with various game engines such as Blender and Unity, among others. In some exceptional cases, the input scenario can be drawn by the developed graphical-user-interface (GUI) attached to the simulator. The output of the first stage consists of structures whose fields are represented by polygons, normals, vertexes, planes, and wedges. An adjacency matrix may also be introduced to establish the mutual dependency between these fields.

It may be that one file, for instance an *.OBJ file, has various formats specified by polygons (3-vertexes, 4-vertexes) and the orientation of the normal and bounding box specifics. As a result, even if the uploaded file has the correct extension, the first stage is not able to handle it because of a mismatch in the formats. Therefore, a validating function which tests the input file format has been developed to avoid such situations. It verifies the presence/absence of various properties of the input OBJ-file, and also compares the relative orientations of the elements to each other.

Spatial division (see Sec. 3.2.2) is also performed at this stage. This is represented by an adjustable tree of boxes partitioning the entire scene, or part of it. The fine-tuning elements here are the density of the scene's polygons per box, the hierarchy depth and the number of children in the tree.

4.1.2 Second Stage: the Propagation Engine

The propagation engine searches for all the possible MPCs in a site-specific environment. For the simulation of mmWave networks in this thesis, the 3D and simplified 2D versions of the propagation engine are utilized. The 3D version produces the most accurate results, but the simulation time can take many hours, while the simplified 2D version can execute a rather complicated scenario within a few minutes. Because the 2D propagation engine is a special case of the 3D one, only the 3D need be explained in further detail.

RL (see Sec. 3.2.1.2) was selected as the primary propagation engine for the second stage (see Fig. 4.1). The reason for this choice is based on the mentioned in literature [77] linear dependence of the simulation time on the complexity of the deployment. Additionally, it utilises an intuitive and straightforward algorithm that supports any 3D-polygonal model. A geodesic sphere was chosen as the source for

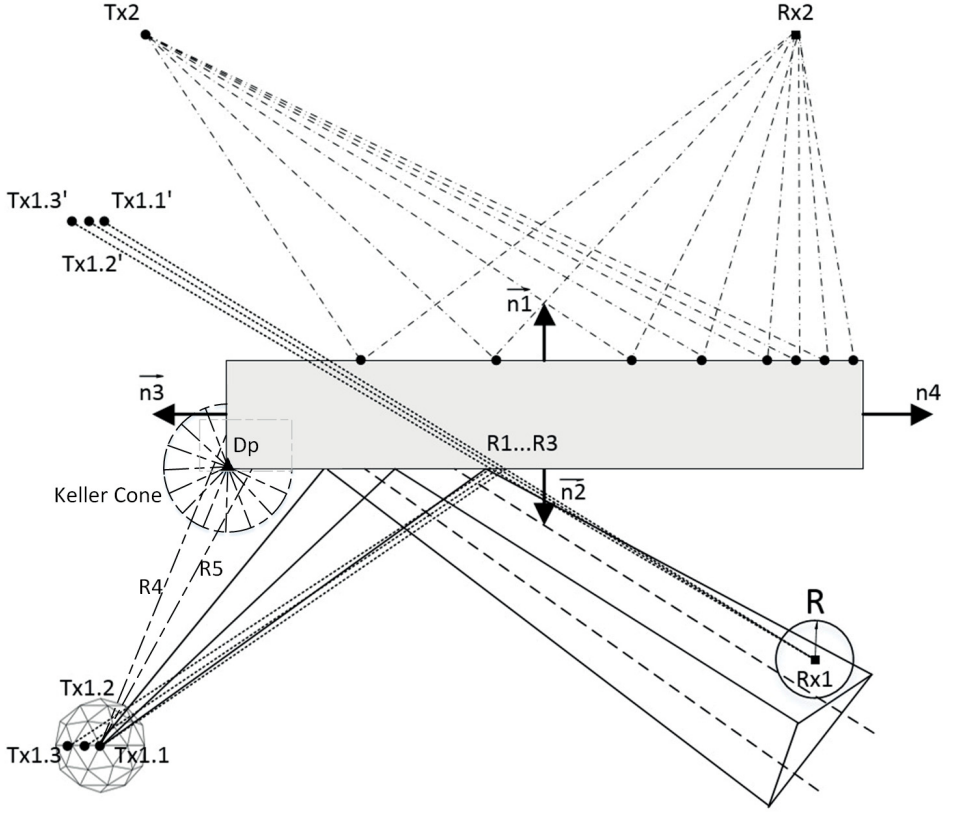


Figure 4.1 Propagation engine employed in the proposed RT tool.

the rays to guarantee their uniform, all-directional density. Employing Smith's algorithm [95] each of the rays is tested on the intersection with the boxes dividing the scene space (not shown in Fig. 4.1). Furthermore, for the intersected box a ray-polygon intersection test [96] is executed to identify the ray-object intersection points, and, as a result, to determine the reflected path (solid lines, intersected the Rx1 in Fig. 4.1).

Also, if two adjacent rays $R4$ and $R5$ in Fig. 4.1 intersect two different sides (polygons) of the object(s), then diffraction potentially may occur. To recognise this effect, first, we search a wedge located between the rays using the ray-triangle intersection test (Moller-Trumbore algorithm). In this algorithm, the ray represents a wedge, while $R4$ and $R5$ form the triangle. If the intersection point Dp exists, then the Keller cone is created, starting from the Dp point. Basically, it consists of hundreds of secondary rays. It should be noted that the presence of the wedge

diffraction can be limited by the threshold angle between the polygons, forming the wedge. For example, it is possible to specify that the diffraction occurs at the wedge angle below than 120 degrees. Such a procedure might be useful when the geometry of the loaded 3D model is inaccurate.

An algorithm calculating the shortest point-to-line distance is introduced to test the intersection of the rays with the receiving sphere. However, because of the fundamental limitation of the RL associated with the finite radius of the receiving sphere (see Sec. 3.2.1.2), it is impossible to calculate the propagation distance (or the time and signal phase) of an MPC accurately. Even a small variation of the distance at the mmWave (wavelength less than a centimetre) leads to a noticeable phase error. Thus, any straightforward utilization of the RL makes modelling the most critical mmWave 5G technologies, such as multiantenna arrays and MIMO channels, impossible. Therefore, an additional image-based RT method was introduced on top of the RL, to overcome this limitation. Consequently, the propagation engine performs a two-stage approach. In the first stage, the intersection of rays with objects and RX(s) occurs. The second stage uses the image method to precisely describe the paths found in the first stage (see Fig. 4.1).

When modelling large areas (e.g. a city) the problem of ray spreading, which results in skipping rays at the receiving sphere, is unavoidable. The straightforward method of increasing the ray density prevents any significant rise in the preprocessing and computational time. Another tempting algorithm that increases the radius of the RX, may cause a propagation error. This only becomes clear when, due to its large size, the sphere starts intersecting the surrounding objects. In this case, artificial densification of the rays after each interaction with objects is introduced. This approach results in a almost linear relationship between the computational time versus the size and complexity of the scenario, when the workflow is multi-threaded (explained later).

Besides a mirror surface, rough one may also be observed in practical deployments. However, straightforward modeling of such surfaces, rendered as 3D models, is quite problematic due to the huge calculation time. Even a small square centimeter of the rough surface may include hundreds of polygons. Therefore, the number of imitating models was proposed that describe the effect of roughness and surface heterogeneity. In this thesis, single-order, diffuse scattering model [91], [97] is employed to complement the GO and UTD methods. This model simulates reflection

from a wall with roughness. The propagation geometry of the diffuse scattering is based on the surface tessellation principle, where each element (tile) behaves as the source of the secondary diffuse scattered rays. Each tessellation round reduces the size of a single tile until its linear size, D , satisfies the far-field conditions as follows:

$$r > 2D^2/\lambda, \quad (4.1)$$

where r is the tile-RX distance, and λ is the wavelength. The black dots in Fig. 4.1 denotes the centre of these tiles, while the dashed lines, proceeding from this points, represent the diffuse scattering paths. In practice, the level of roughness can be determined visually (done in the thesis), by video processing [98], or by using specialized device such as roughness tester.

4.1.3 Applied Accelerating Methods in the Second Stage

Both algorithmic and hardware acceleration approaches are proposed to reduce computational time. Additionally, the RT architecture was developed in line with the recommendations for efficient Matlab coding described in [99].

Besides the conventional acceleration techniques mentioned in Sec. 3.2.2, a novel algorithm is introduced. This filters out the shadowed polygons, which cannot even hypothetically interact with any of the rays. Specifically, a polygon whose normal, \mathbf{n} , is shaded from a ray with direction, \mathbf{e} , should satisfy the following equation so that $(\mathbf{n} \cdot \mathbf{e}) > 0$. In practice, this algorithm reduces the number of polygons to be processed by almost 50%.

Furthermore, all the RT internal processes are divided into time-critical (intersection tests) and time non-critical (routine procedures) groups. The first group is converted to the standalone C/C++ code using the built-in Matlab Coder Toolbox to improve the overall performance of the RT. These transformations resulted ¹ in an additional gain in computational time to the order of $\times 1.5$. Additionally, the Parallel Computational Toolbox is actively exploited in the tool to further reduce the computation time. This resolves the computational and data-intensive tasks in concurrent processes using multicore processors. The most distinct advantage of this toolbox is that it supports the high-level programming style. The observable assess-

¹However, before beginning this implementation, the Matlab code should be reviewed first, because, for example, the recursion and cell array may not be supported by the Matlab Coder Toolbox.

ment of the acceleration gain contributed by the Parallel Computational Toolbox is $\times 2.5 - 3.5$. The resulting contrast between the non-accelerated and accelerated RTs is shown in Fig. 4.2.

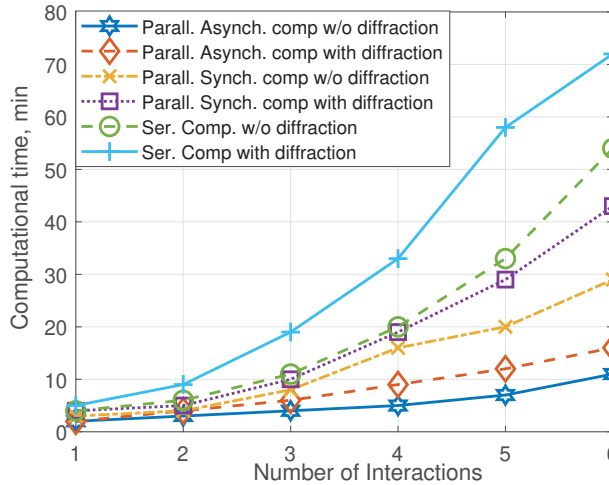


Figure 4.2 Comparison of computational time versus different accelerating techniques in Matlab. Simulated scenario is urban topology with square buildings.

An accelerating algorithm that optimizes the simulation of the MIMO channel is also applied. By default, a typical RT completes one simulation round as soon as all the possible paths between a single TX and all the RXs are established. Consequently, in the case of a MIMO channel consisting of N uncorrelated antennas, the simulation time rises by N -times as well. Taking this into account means that any straightforward utilization of the RT looks challenging. Therefore, the following assumption is proposed: *the paths established by the MIMO system interact with identical objects but have different intersection points*. This assumption is reasonable at the mmWave band when the inter-antenna distance is much smaller than the size of the scene objects. At the level of an algorithm, it means that if the path $TX1.1-R1-RX$ in Fig. 4.1 is determined, then the paths $TX1.2-R2-RX$ and $TX1.3-R3-RX$ can be found without restarting the propagation engine. Consequently, the output results show that 4×4 MIMO increases the computation time $< 5\%$ in the case of a single antenna.

Finally, it should be emphasised that it is impossible to build an ideal accelerated propagation engine that performs efficiently in all of the 5G deployments. The sim-

ulating methods and settings should be selected individually, according to the task at hand. For example, the topology, size and shape of the scene, as well as the number, type and location of the antennas involved in the simulation will specify that choice.

4.1.4 Fourth Stage: Post-processing

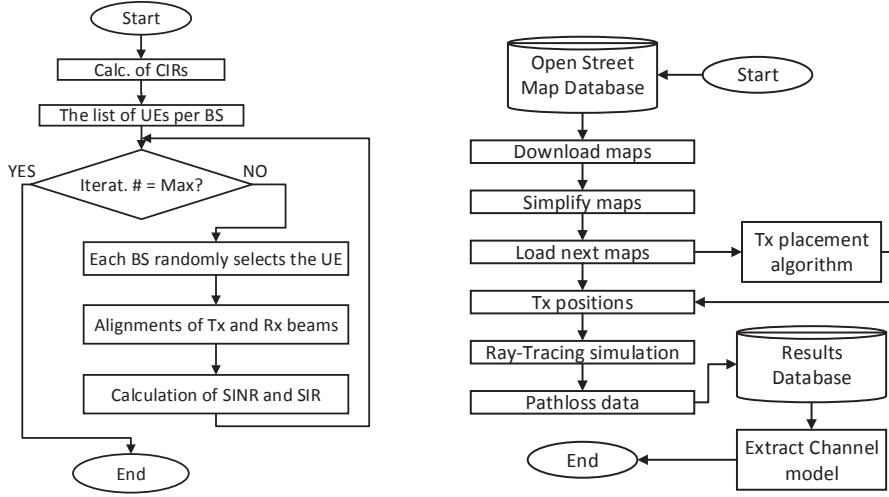
The goal of the post-processing stage is to transform the physical E - and H -fields into typical communication parameters, such as total received power, delay/angular spreads, and some other ones mentioned in Sec. 2.1. For this thesis, additional metrics such as signal-to-interference noise ratio (SINR) and interference-to-noise ratio (INR) [100] are introduced to characterize the interference properties described in Sec. 6.4. These interference metrics fit comfortably into the post-processing stage due to the physical origin of their power components.

4.2 RT-based Framework

RT-based frameworks, illustrated in Fig. 4.3, extend the basic capabilities of the RT by employing additional algorithms around it. In this thesis, two frameworks are considered: i) the framework for MAC-abstraction, and ii) the map-based framework. Both of these are described in detail below.

4.2.1 The RT-based Framework for MAC-abstraction

The purpose of this framework is to calculate the interference metrics, accounting for the detailed antenna model and MAC-abstraction represented by a Round-Robin scheduling algorithm. In practice, the framework imitates the network operation, when the BS serves only one user equipment (UE) from the list of those in a certain time-stamp. This MAC-abstracting framework, demonstrating in Fig. 4.3a, is executed as follows. In the first stage, the RT calculates the CIRs between the TXs (mmWave BSs) and RXs (UE). The output data from this is an array whose cells describe the wireless channel properties of every TX-RX pair. Then, using the best signal-to-noise ratio (SNR) criterion, a list of serving UEs is created for each of the BSs. The UEs are selected from these lists (one UE per list) to be served further by its BS. The beam alignment between the BS and the selected UE is arranged along the most dominant path, while the antenna patterns are chosen from the predefined



(a) The framework enabling the MAC-abstraction.

(b) The framework for the map-based RT simulation (modified from [101]).

Figure 4.3 A block-diagrams of the two utilized RT-based frameworks.

codebook. Finally, once all the links are established, the algorithm calculates the interference metrics (SIR, INR), accounting for CIR, transmitted power and antenna gain. These steps are repeated many times to collect enough statistics on the interference behavior.

4.2.2 The Framework for the Map-based RT Simulation

The framework shown in Fig. 4.3b was used to complete the massive simulations of the deployment. First of all, this framework cuts the whole map into overlapping pieces and stores all of them, one by one. In the next stage, a specific algorithm (described in Sec. 5.1.3) installs the mmWave BS in each of those pieces and covers the area with the RX-grid (see Fig. 5.1c). After these preparatory steps, the 2D RT simulates the channel properties in each of the stored small maps. The output results are accumulated for further processing and plotting.

Cutting the whole city map into pieces and adapting them for the 2D RT simulation makes massive simulations feasible. Instead of many hours of straightforward 3D RT running in a large urban area, the map-based framework takes up less than half an hour.

4.3 mmWave Sounding Equipment

Besides the RT tool and the frameworks explained earlier, the mmWave measurements are performed to produce the calibrating data as a part of the proposed methodology. Specifically, the wideband 28 GHz channel sounding assembled in Aalto University's Department of Radio Science and Engineering is illustrated in Fig. 4.4.

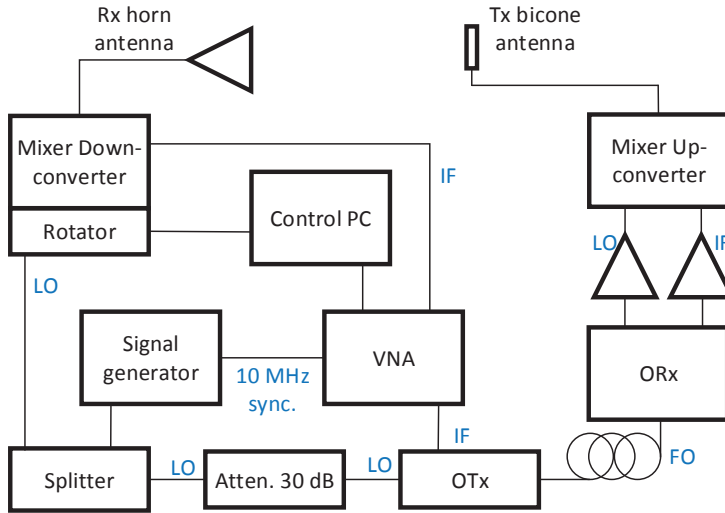


Figure 4.4 28/60 GHz sounding equipment (modified from [94]).

Its key component is the vector network analyzer (VNA). This setup was utilized in [94], which studied signal blockage by a vehicular body, as well as validated the proposed RT tool. The TX side is represented by a 2 dBi omnidirectional antenna, having elevation half-power beamwidth (HPBW) of 60°. The RX side is a 19 dBi horn antenna with HPBW = 10° in the azimuth, and 40° in the elevation plane. The RX system is mounted on a rotator to perform the directional measurements of S21 parameters over the azimuth angular range of 0 to 360°. The frequency and power of the local oscillator (LO) are 12.5 GHz and 6 dBm, respectively. The intermediate frequency (IF) varies from 2 to 2.9 GHz and -15 dBm power at the VNA. The essential 28 GHz frequency was achieved with an up-converter combined with a frequency doubler for the LO signal. Additionally, a 30 dB attenuator is included to prevent any possible damage to the down-converter. The 10 MHz cable does the

synchronization between the VNA and the signal generator. A more detailed description of the channel sounder, as well as the scenario of interest, can be found in [102].

A wideband 60 GHz channel sounding setup was utilized in [103], which studied the effect of input data accuracy on the output results of RT. It was built on the 28 GHz channel sounding, in which the antennas, up- and down-converters operating at 28 GHz were replaced by ones supporting 60 GHz.

5 DEPLOYMENTS

In order to apply the methodology described in Chapter 4, 3D models of the following deployment were created and utilized: i) mmWave urban cellular networks, ii) mmWave backhaul links, iii) mmWave urban vehicular links, and iv) mmWave network for the drone detection. The general assumption applied for all of these scenarios was associated with a limited level of detalization of the 3D models. This enables to focus on the most significant phenomena on the one hand, and also reduces the calculation time down to several hours.

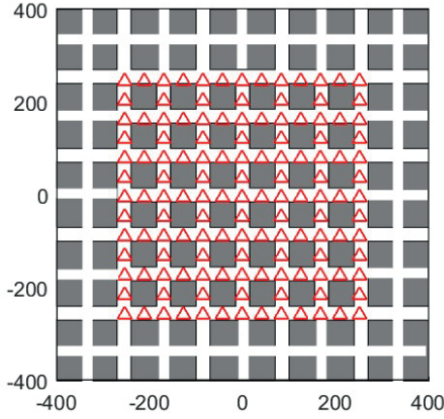
5.1 mmWave Cellular Networks

Variations of the Manhattan grid scenarios (Fig. 5.1) were selected to investigate the underlying propagation effects and performance of cellular mmWave networks. The distribution of buildings is common to both small towns and giant metropolises, which makes it a good reference topology [104]–[106]. Geometrically small objects, such as kiosks, lampposts and even people, are excluded from the scenario. Thereafter, it is the buildings which appear to be the main source of signal blockage. In this study, three variants of the Manhattan grid topologies are considered: i) idealized without the central square (Fig. 5.1a), ii) idealized with the central square (Fig. 5.1b), and iii) a map-based topology (Fig. 5.1c).

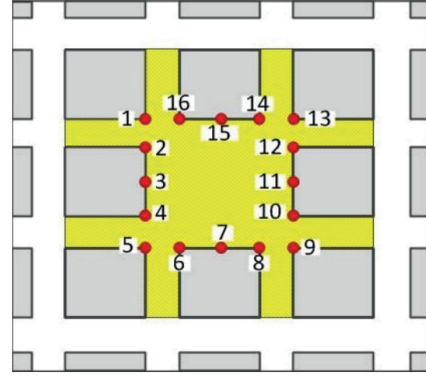
5.1.1 Idealized Manhattan Grid with the Open Square

The Manhattan grid with the open square [110], [108], [109] represents a variety of downtown environment, such as Brooklyn, New York [111] for instance. This scenario was selected to evaluate the diffuse scattering effect caused by mmWave networks as described in Sec. 6.1.

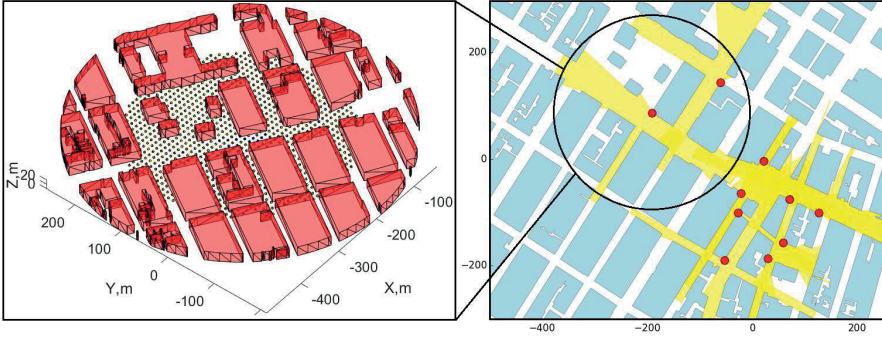
The distributed TXs (the red dots in Fig. 5.1b) represent the mmWave BSs. These are installed on the building walls around the central open square at a height of 5 m.



(a) Idealized without open square [103]



(b) Idealized with open square [107]



(c) Based on the real city map [101]

Figure 5.1 Manhattan grid mmWave cellular deployments

Their primary operating frequency is 28 GHz, but 2.4 GHz is also performed by way of comparison. The RXs (yellow zone in Fig. 5.1b) are uniformly distributed in the central area and partially overlap the adjacent roads. The height of the RX-grid is 1.5 m. All of the elements of the MAC-layer are excluded in order to focus only on the propagation effects. Additionally, all the antennas are assumed to be isotropic to obviate any impact from the antenna functionality. Concrete was selected as the reference material to specify the physical properties of the building walls. Dielectric permittivity ϵ is equal to $5.3-0.3j$ at 28 GHz and $5.3-0.5j$ at 2.4 GHz [112] respectively. The roughness σ is set at 0 for a specular surface and 1 mm for an irregular one.

5.1.2 Idealized Manhattan Grid Scenario Without the Open Square

The scenario illustrated in Fig. 5.1a is a generic version of the Manhattan grid that has regularly periodically distributed buildings and roads. It is used for the detailed analysis of interference in the high-density mmWave networks described in Sec. 6.4 and the depolarization effects described in Sec. 6.5. Transmitting antennas, TXs, which act as mmWave BSs, are uniformly distributed between the buildings (see the red triangles in Fig. 5.1a). As with the open square deployment, the RXs (representing the UEs) are collected into the RX-grid. The heights of the UE antennas and the mmWave BS are 1.5 m and 10 m respectively. Each of the antennas is equipped with a directive pattern, specified by the codebook. The operating frequency is 28 GHz. Additionally, the concrete selected as a reference material for the building walls has a dielectric permittivity of $\epsilon = 5.3 - 0.3j$ [112].

5.1.3 Map-based Manhattan Grid Topology

The Open Street Map [113] (OSM) project is used to obtain the real geospatial data of Manhattan Island. It facilitates evaluation of the performance of massive RT simulations in map-based topologies with reduced spatial dimension (from 3D to 2D) as described in Sec. 6.2. The TX placement conforms with the algorithm proposed in [114], which searches for the best LOS condition for a certain antenna location. The carrier frequency of the transmitted signal is 28 GHz. The receiving antennas are aggregated into the equidistant RX-grid (the dots in the middle of Fig. 5.1c). As with the other idealized deployments, the MAC-layer is suppressed and antennas with an isotropic pattern are activated. Additionally, all the TXs and RXs are installed at heights of 10 m and 1.5 m, respectively. The material for the building walls is concrete, specified by $\epsilon = 5.3 - 0.3j$ [112].

5.2 The mmWave Backhaul Links

The buildings of the School of Electrical Engineering in Aalto University were selected as a real world environment in which 60 GHz backhaul links are deployed on the rooftops. Two versions of this deployment were built with PTC Creo [116] software: i) non-precise, outlined by Google Earth, and ii) precise (Fig. 5.2), refined

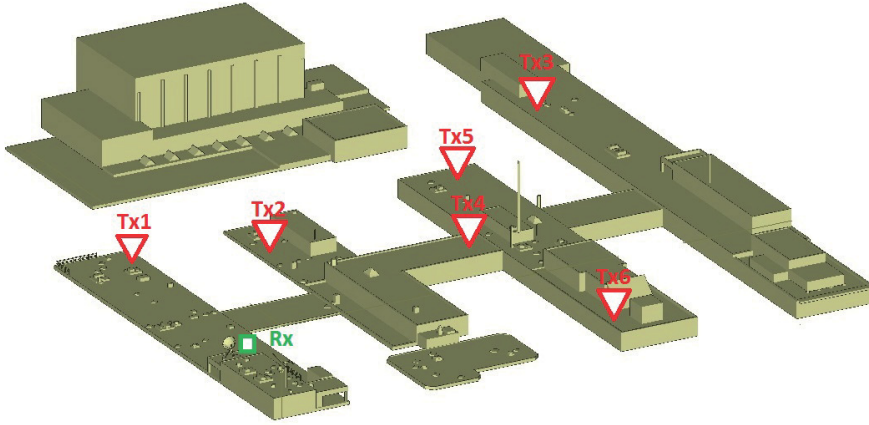


Figure 5.2 mmWave Backhaul Link Deployment (modified from [115]).

using the photogrammetry method. These two replicas have different levels of detail and accuracy. For example, the precise version includes many electrically-large objects such as boxes, pipes and rooftop antennas which are invisible in the Google Earth application. Then, these two 3D models are uploaded and simulated by the RT to show the impact that the precision of the input data has on the output results, as described in Sec. 6.6. A comparison of these two simulated data sets with their measurement results is regarded as a figure of merit in this thesis. The rooftop antenna positions are shown in Fig. 5.2 as a green rectangle (RX) and red triangles (TX). Each of the building walls is specified by $\epsilon = 2.55 - 0.43j$ [117].

5.3 The mmWave Network Deployment for Drone Detection

The idea for exploiting mmWave 5G networks for the detection of invasive drones is outlined in Fig. 5.3. The transmitting system generates an mmWave wideband signal into the upper hemisphere. As soon as a drone appears in a prohibited zone, a signal is reflected from the drone's body. Furthermore, this signal can be detected by multiple receiving BSs, forming a so-called multistatic radar operation. The multiplexer in Fig. 5.3 synchronizes the cooperative operation of the TXs and RXs, while the data processing centre decides whether detection has occurred or not, based on

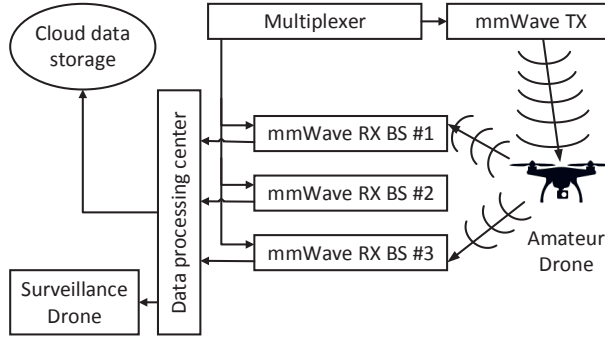


Figure 5.3 Block-diagram of the mWave networks assistance to detect the violating drones (modified from [118]).

signatures in cloud data storage. Finally, in the case of a positive identification, a surveillance drone can intercept the intruder.

Two deployments were created to simulate this concept in RT. The first one focuses on the investigation of a drone's reflectivity as described in Sec. 6.3. To this end, a dense RXs-grid is introduced to capture the signals scattering from the drone's body. A single TX antenna is located immediately beneath the drone. The distance from the drone to TX and RX-grid is 10 m. Any LOS-paths are suppressed, while the reflected and diffracted ones contribute to the total power on the RXs. An isotropic radiator was selected to avoid any impact from the antenna pattern. The carrier frequency is 28 GHz.

The second deployment represents a simplified 100×100 m Manhattan grid scenario, where mmWave BSs are uniformly distributed at a specified density. As soon as a drone appears, the nearest mmWave TX system irradiates the drone with a signal. The other mmWave BSs behave as RXs, capturing portions of the scattered rays coming from the drone body. The goal of this deployment is to estimate the detection probability of the violating drone as a function of the RX density. The mmWave BSs are equipped with the directive antenna pattern proposed by 3GPP [109].

The carrier for the TX signal in both of these deployments was 28 GHz. The 3D model of the drone consists of plastic and metal parts with $\epsilon = 2.54 - j0.002$ [119] and $\epsilon = 1 - j6.5 \times 10^6$ [120].

5.4 mmWave Urban Vehicular Links

The urban street canyon (see Fig. 5.4 and 5.5), in which the vehicle(s) behave(s) as the main source of the blockage, was used as a reference scenario for the RT simulation and channel measurement at 28 GHz (see Sec. 6.7). The objectives of this research were: i) to evaluate the blockage caused by the vehicle(s) and identify alternative/backup propagation paths to link the TX and RX reliably, ii) to tabulate excess loss, specifying the propagation mechanisms, and iii) to validate the accuracy of the developed RT with measured data. The scenario consists of buildings on the left and right, as well as foliage growing on the right side of the road. The distances between the TX and the RX antennas are 12 and 10 m.

The locations and orientations of the vehicle(s) are varied (see Fig. 5.4) to isolate

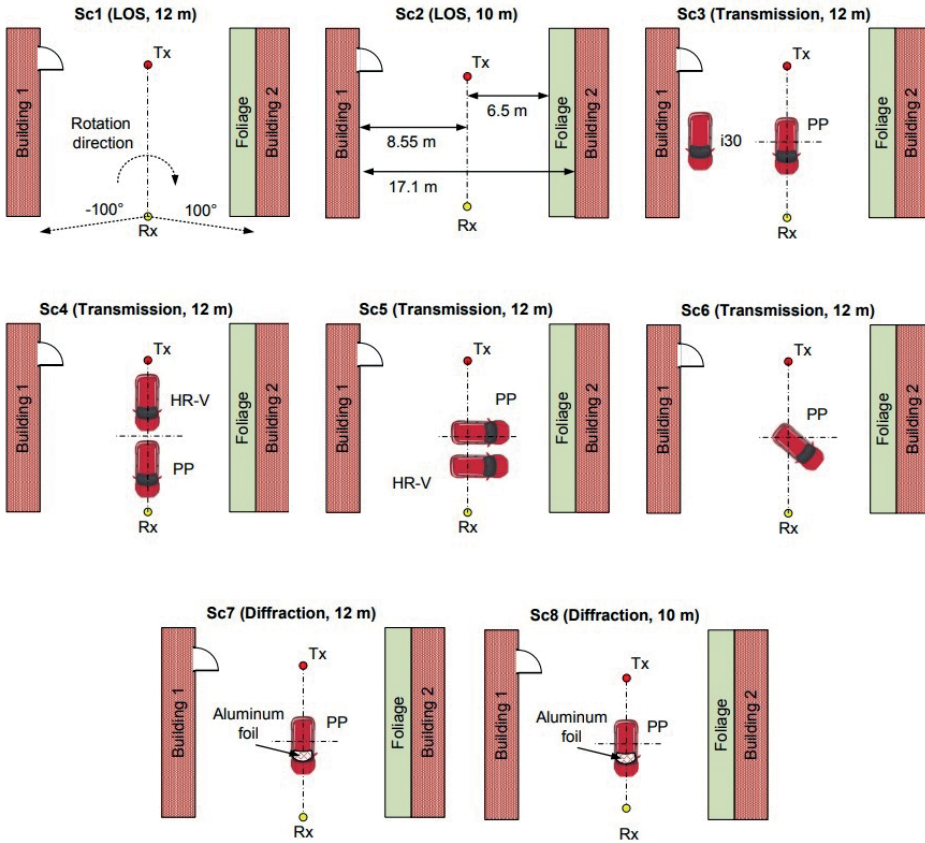


Figure 5.4 Street-canyon urban deployment with vehicular blockage [94].

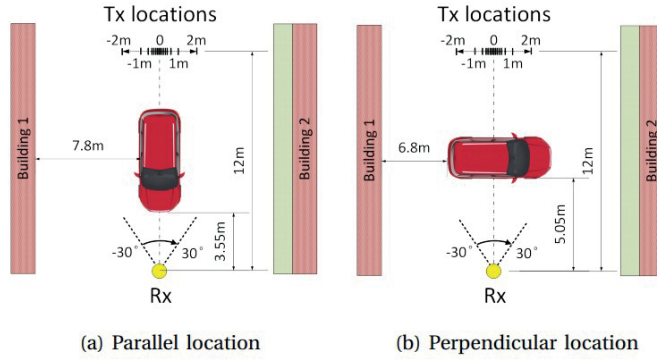


Figure 5.5 Deployment for in-depth analysis of transmission through the vehicular cabin [94].

a particular propagation mechanism. For example, an empty scenario (no vehicles) is used to calibrate the mmWave sounding equipment with the LOS transmission. Additionally, parallel or perpendicular orientation of the vehicle(s) to the TX-RX link is used to study the transmission through the vehicle and the diffraction around it. Finally, Scenario 3 (Sc3 in Fig. 5.4) has the vehicle next to the left wall, which demonstrates the reflection excess loss from the vehicular body.

Two additional deployments (Fig. 5.5) were introduced to carry out an in-depth analysis of transmission through the vehicular cabin, in which the TX-RX 5 m link is obstructed by the vehicle under test. As with the previous set of measurements, the orientation of the car is changed by 90 ° relative to the TX-RX link, resulting in the signal being transmitted either along or across the cabin of the vehicle. To obtain the

Table 5.1 Utilized physical properties

Parameter	Value	Ref.
Building walls	Brick, $\epsilon = 3.75 - j0.0244$	[120]
Ground	Dry ground, $\epsilon = 5 - j0.053$	[121]
Veh. body	PEC, $\epsilon = 1 - j6.5 \cdot 10^6$	[120]
Veh. windshield	Glass, $\epsilon = 6.27 - j0.15$	[120]
Veh. interior	Polystyrene, $\epsilon = 2.54 - j0.002$	[119]
Veh. tires	Resin, $\epsilon = 3 - j0.08$	[122]

dependence of signal strength as a function of antenna position, TX was displaced from 0.1 to 2 m relative to its original position. The material and physical properties of these deployments are listed in Table 5.1. Specifically, the building wall is made of brick, while the blocking vehicle consists of many parts with distinct materials.

6 RESULTS

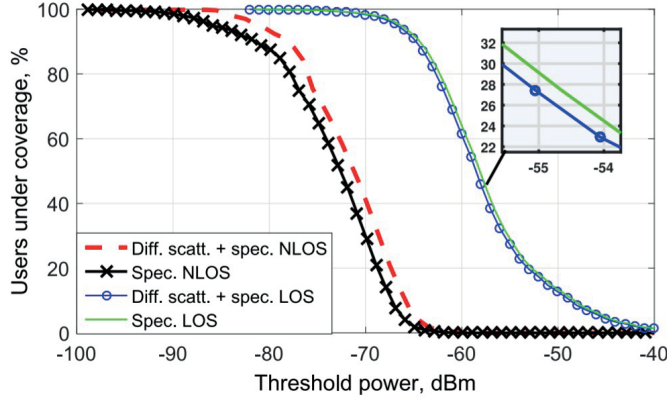
6.1 The Power Contribution of the Diffuse Scattering

The objective of the study in [107] was to evaluate the power contribution of the diffuse scattering caused by the mmWave cellular TXs to the total received power at the RXs. The primary carrier frequency is 28 GHz, while an additional 2.4 GHz is only introduced to make the output results available for comparative analysis. The idealized Manhattan grid with the open central square described in Sec. 5.1 was selected. Being surrounded by multiple building walls that scatter the signal, the central area seems an appropriate place for such research.

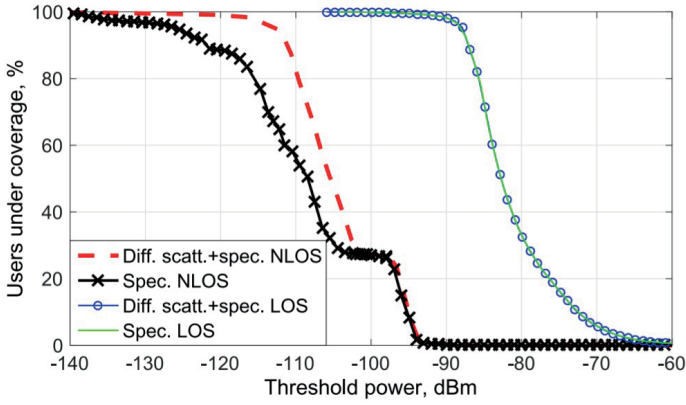
The building walls have reasonably practical irregularities of $\sigma = 1$ mm, leading to the potential formation of diffuse scattering components whose gain is specified by the Lambertian pattern. The proposed RT tool described in Sec. 4.1 was utilized to perform both the specular reflection and diffuse scattering components. The output results shown in Fig. 6.1 demonstrate the distribution of the total received power on the RX grid through the cumulative distribution function (CDF). According to this, the power contribution of the diffuse scattering is almost zero (around the accuracy of the RT) in LOS conditions at both frequencies (Fig. 6.1b and Fig. 6.1a). The reason for this is the tremendous difference between the LOS power and the power contributed by the diffuse scattering components.

The power distribution in NLOS TX-RX conditions behaves differently at both frequencies. The power contribution of the diffuse scattering at 2.4 GHz is several dBs. The reason for that is the long wavelength, which does not sense those irregularities whose dimensions are many times smaller. Accordingly, the reflected components of that signal mostly carry the specular part.

In contrast, the 28 GHz band produces a plateau in NLOS power CDF whose dimensions are linearly dependent on the level of roughness. Accordingly, this effect may define the amount of diffuse scattering components formed by reflection of a



(a) CDF of the total received power 2.4 GHz data.



(b) CDF of the total received power 28 GHz data.

Figure 6.1 CDFs of the total received power [107].

signal. The Lambertian diffuse scattering model applied on top of that partially compensates for this plateau. However, because first-order diffuse scattering is used, this model does not fully compensate for this effect. The power contribution of the diffuse scattering at 28 GHz is roughly 6 dB.

6.2 The RT Methodology for the Massive Simulation of Manhattan Island

The deployment shown in Fig. 5.1c, and the algorithm described in Sec.4.2.2 are utilized to demonstrate a 2D RT-based methodology capable of simulating scenarios

built on real maps. The channel properties listed in Sec. 2.1 were selected as comparative metrics to evaluate the total accuracy of the proposed methodology. For that purpose the K-factor, DS, AS, and LOS probability were compared with similar metrics proposed by the 3GPP model in [109]. The results of this comparison are shown in Tab. 6.1.

Table 6.1 Comparison with 3GPP parameters [101].

Parameter	Improved 2D SBR	3GPP
Rician K-factor	$\mu = 13.7$	$\mu = 9, \sigma = 5$
$\log_{10}(\text{Delay spread, s})$	LOS: $\mu = -7.3$ NLOS: $\mu = -6.8$	LOS: $\mu = -7.49, \sigma = 0.38$ NLOS: $\mu = -7.18, \sigma = 0.51$
$\log_{10}(\text{AoA spread, } ^\circ)$	LOS: $\mu = 1.5$ NLOS: $\mu = 2.1$	LOS: $\mu = 1.61, \sigma = 0.30$ NLOS: $\mu = 1.69, \sigma = 0.37$
$\log_{10}(\text{AoD spread, } ^\circ)$	LOS: $\mu = 1.3$ NLOS: $\mu = 1.4$	LOS: $\mu = 1.13, \sigma = 0.41$ NLOS: $\mu = 1.19, \sigma = 0.49$

The mean values of the channel properties are fairly similar, but some of them are outside the standard deviation limits. The main reason for this is the violation of the periodical behaviour in a real Manhattan grid scenario (see Fig. 5.1c).

Next, the 3GPP PL is compared to the simulated one, and this is shown in Fig. 6.2.

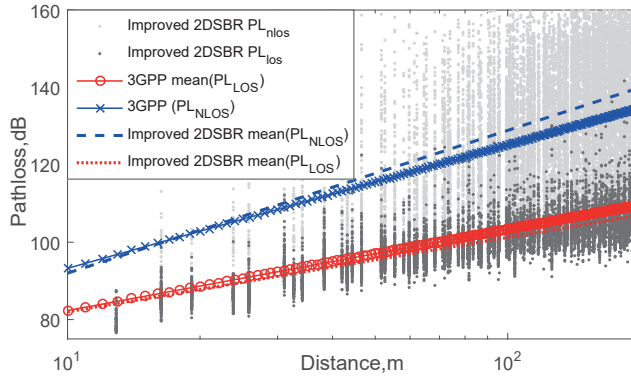


Figure 6.2 Omnidirectional path loss [101].

Finally, the 3GPP LOS probability is compared to the simulated one. The result of this comparison, shown in Fig. 6.3, is almost identical to the 3GPP one.

Within the framework of this research, artificially-generated ground-reflecting beams are introduced to the 2D RT to try and achieve a similar accuracy to the 3D one. The CDF shown in Fig. 6.4 demonstrates the accuracy of this approach. Here,

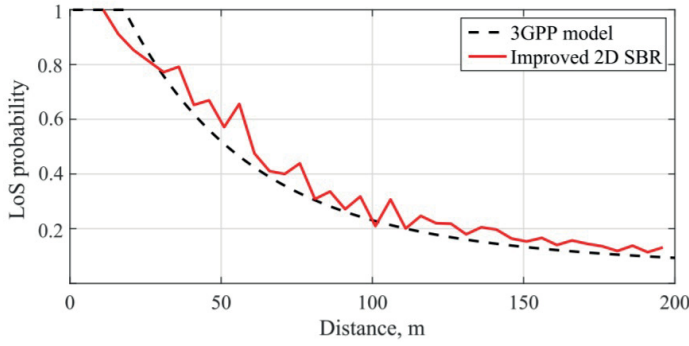


Figure 6.3 LOS probability [101].

Δ_1 and Δ_2 are the differences between the total received power produced by the 3D RT and the 2D RT with and without the ground-reflecting beams. The difference is estimated at the same RX points.

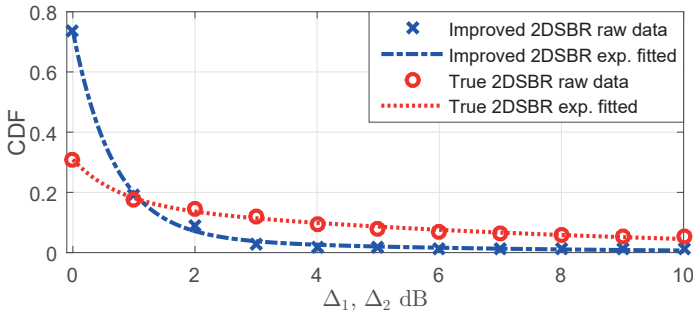


Figure 6.4 The total received power difference between 3D and 2D RT results [101].

The proposed methodology can accurately parametrize analytical and empirical models and collect the mmWave channel statistics from multiple realistic city maps $\times 15$ times faster than a typical 3D RT can. Additionally, these artificially-generated ground-bouncing rays can significantly improve the model’s accuracy without wasting extra computational time. Nevertheless, the 2D RT based methodology has two limitations. First, it only works accurately when it is deployed in environments with flat building walls that are perpendicular to the ground. Second, the antenna position should be significantly below the rooftops.

6.3 Drone Detection Assistance with mmWave Networks

Using the deployment in Sec. 5.3 and the RT tool in Sec. 4.1 introduced the possibility of using an mmWave network to detect drones flying into restricted areas [118]. The decision to use the mmWave band is based on the following factors. First, the small wavelength enables the detection of relatively small drones that would be invisible in the uWave band. This capability relies on the principle that objects which are larger than the wavelength scatter a stronger incident signal. Secondly, the mmWave spectrum makes use of a huge bandwidth, which improves the detection probability and enables the distinction of multiple individual drones within a swarm. For example, a bandwidth of 1 GHz can provide a spatial resolution of only 15 cm.

Fig. 6.5 demonstrates the body reflectivity of (left) a small unloaded drone with a linear size of 0.6 m, and (right) a large loaded drone with a linear size of 1.5 m.

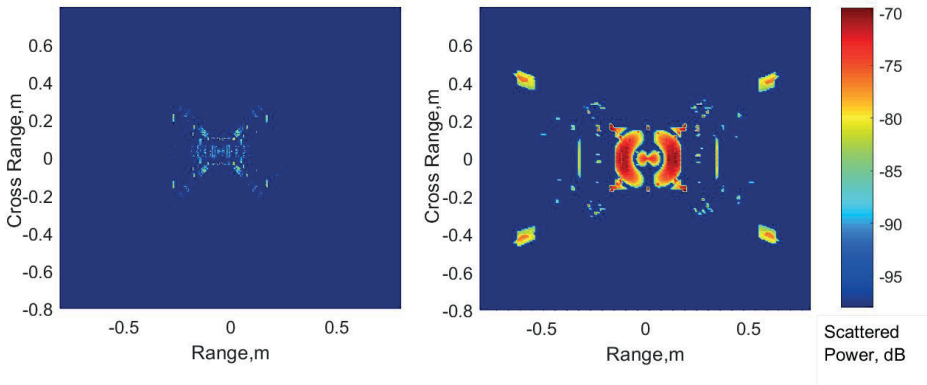


Figure 6.5 The reflectivity of the small unloaded drone (left image) and large loaded drone (right image) [118].

The loaded drone carries a square box attached to the bottom of its body. The red colour in this figure corresponds to the intensively reflected area (scattering centres), while the blue colour indicates either low or none reflected power. This figure was obtained as follows. Initially, the scattered points¹ on the drone's body are projected onto a plane, i.e. an orthogonal representation of a 3D object is projected onto a 2D plane. Further, each of the projected points specified by the (X, Y) coordinates is assigned a third Z -coordinate, showing the scattering power coming from a certain point of the drone body.

¹In RT jargon, a scattered point means the same as a ray-polygon intersection point.

It is clear that the presence of intense red zones in the right-hand image and the absence of these in the left-hand one indicate that the size and shape of the drone play a crucial role in its detection. However, it is also clear that the structure of the patterns shown in Fig. 6.5 is somewhat discontinuous. Therefore, the spatial orientation of a drone, as well as the density of the mmWave BS on the ground, may also play an important role. Therefore, simulations showing the probability of detecting an invasive drone as a function of the BS density have been performed. The results of these simulations are shown in Fig. 6.6, and they indicate that a typically-sized drone might be reliably detected when the network density is one BS per 100 m².

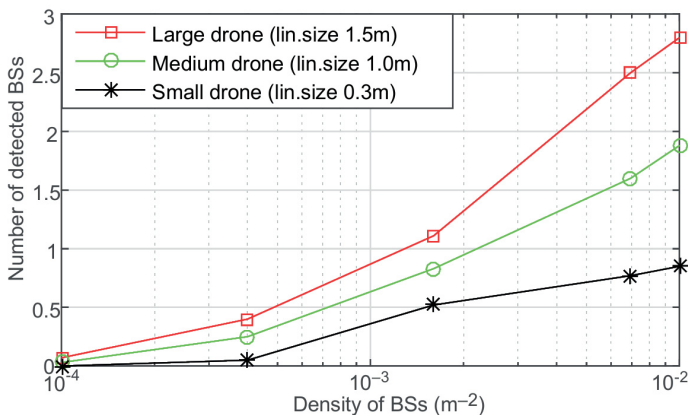


Figure 6.6 The mean number of the mmWave BSs detected the violating drone [118].

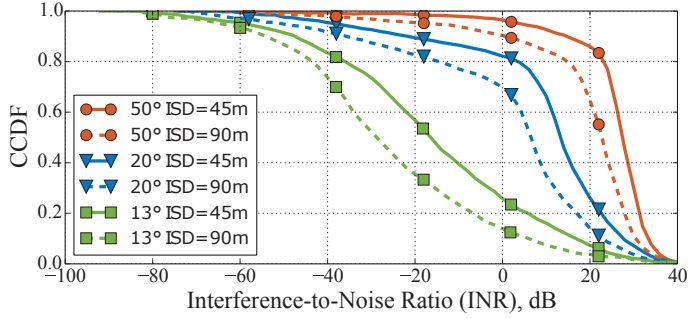
However, drones of less than half a meter cannot be detected at all using these mmWave network capabilities, as a consequence additional solutions must be applied.

6.4 Interference Analysis

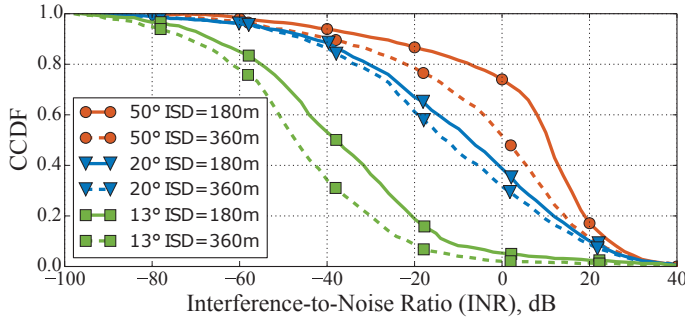
There are two extreme regimes in which an mmWave network may operate, an interference-limited one and a noise-limited one. The first one defines the conditions when the interference behaves as a dominant factor, reducing the SINR, and thus, the mmWave network's capacity. In contrast, the noise-limited regime is activated when the noise level crucially impacts on the SINR.

Although directive antenna is intended to suppress interference, the impact of HPBW in an ultra-dense deployment looks questionable. Thus, the deployment described in Sec. 5.1 and the methodology proposed in Sec. 4.2.1 are applied to

show how inter-site distance (ISD) and HPBW affect the interference metrics and the network regimes. For this purpose, the CCDF of the INR is obtained as a function of the ISD and HPBW as shown in Fig. 6.7. Fig. 6.7a shows the INR distribution when the ISD is 45 m and 90 m, while Fig. 6.7b shows the INR as a function of ISD = 180 m and ISD = 360 m, accordingly. When $\text{INR} < 0$ dB then the network



(a) Interference-to-noise ratio for Inter-site distances of 45 m and 90 m.



(b) Interference-to-noise ratio for Inter-site distances of 180 m and 360 m.

Figure 6.7 CDFs of the total received power [103].

operates in the noise-limited regime, but when $\text{INR} > 0$ dB the network operates in the interference-limited one. Following this concept, three curves can be observed in Fig. 6.7 (dashed green in 6.7a and both green plots in Fig. 6.7b) where about 80 % of the RXs operate in the noise-limited regime ($\text{INR} < 0$ dB). All of them have similar narrow $\text{HPBW} = 13^\circ$, which mostly constrains the cellular network to work in this regime. At the same time, $\text{HPBW} = 50^\circ$ commits about 80 % of the RXs, represented by red plots in Figs 6.7a and 6.7b, to be in the interference-limited regime ($\text{INR} > 0$ dB). The ISDs, corresponding to this regime, are 45 m and 90 m, accordingly. Other

combinations of HPBW and ISDs produce an intermediate regime, where neither noise nor interference dominates across all of the UEs.

An evaluation of the mean SINRs as a function of HPBW and ISD has been carried out, the results of which are shown in Fig. 6.8. Increasing the ISD reduces the

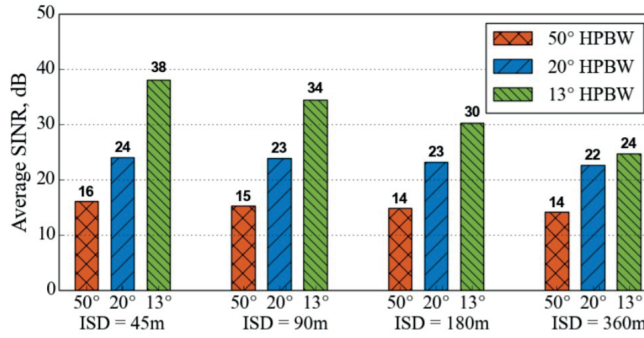


Figure 6.8 Mean SINR as a function of HPBW and ISD [103].

average SINR of mmWave networks from 38 dB to 24 dB when HPBW = 13°. At the same time, the mmWave BS equipped with antennas whose HPBW = 50° are almost independent of the ISD. The reason for this is the compensation for a signal's power by the interfering one.

6.5 The Capacity Gain of Dual-Polarized Antenna in Environment with Diffuse Scattering

In the context of this topic, polarization diversity is considered when there is the potential for a signal to be transmitted from TX to RX by two uncorrelated channels with mutually orthogonal (cross-polarized) polarizations. According to MIMO theory, two independent channels can transmit twice as much data. However, it is not always the truth, and the relevant results are shown in Fig. 6.9.

For the LOS links, the orthogonality is preserved since the performance of a signal does not change in a homogeneous medium (see Sec. 3.1.4). Conversely, the interaction of a signal with surrounding objects can modify the mutual orientation of the \mathbf{E} and \mathbf{H} vectors (see Sec. 3.1.4). Accordingly, if there is a correlation between two orthogonal antenna branches these channels can no longer be regarded

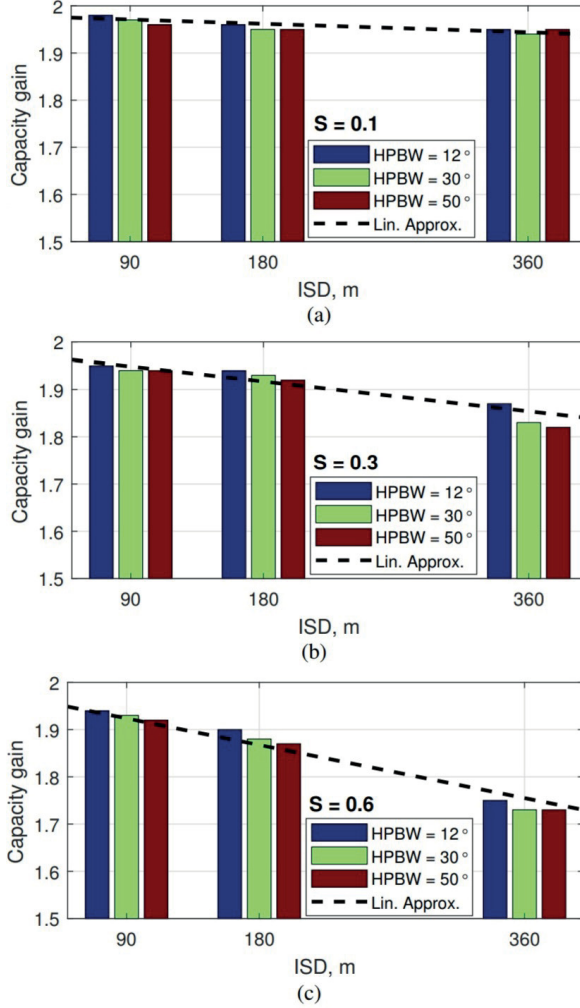


Figure 6.9 The capacity gain as a function of ISD and the level of the diffuse scattering [123].

as independent. Following this assumption, the deployment specified in Sec. 5.1 and the simulation methodology described in Sec. 4.2.1 are applied to study the effect of capacity degradation due to the depolarization mechanism. The transmitting and receiving antennas are represented by an 8×8 slanted $+45/-45$ dipole array, each with dual polarization. The directional pattern of this antenna system is given by the codebook (as per Sec. 6.4). A number of propagation mechanisms such as reflection, diffraction and diffuse scattering are introduced. On top of that, the accelerating algorithm for the MIMO system described in Sec. 4.1.3 is included.

These simulations show that the level of propagation losses is proportional to

the depolarization effect. More specifically, the single order reflection mechanism has relatively small 4 - 7 dB loss, which also introduces a weak depolarization effect. Nevertheless, it becomes 3 dB at a Brewster angle [124] of 60 - 70 ° for horizontal polarization. Furthermore, the reflection order might proportionally increase the depolarization losses.

The next notable observation concerns the diffuse scattering effect. Since the polarization of the diffuse scattering components is random, it may potentially affect the transmission capacity in NLOS conditions, where the role of this diffuse scattering is viable (see Sec. 6.1). The coefficient S , showing the amount of diffuse scattering (see Eq. 3.16), is introduced to investigate this. The first scenario has a small amount ($S = 0.1$) of diffuse scattering, while the third one has a high level of it ($S = 0.6$). The capacity gain is a prime example to show how many times higher the capacity of 2×2 MIMO with polarization diversity is than it is for a single-input and single-output case (SISO). As Fig. 6.9 shows, this improvement range varies from 1.7 to 1.95 and depends on the ISD and HPBW of the antennas. When the TX and RX have a LOS link, the effect of the depolarization is negligible.

6.6 The Impact of the Input Data Quality on the RT Simulations

The aim here is to show the divergence in the simulated results by matching the measured CIR with the one modelled by the RT method using i) the simplified block model, and ii) the accurate photogrammetry-based model. The deployment described in Sec. 5.2, and the Wireless Insite tool described in Sec. 2.2.2 are used for this. The measured data is obtained with the mmWave equipment described in Sec. 4.3, while the comparison metrics, such as PDP and PADP, are explained in Sec. 2.1.

First, a general comparison of the measured and simulated PADPs is obtained for the six RX positions. The result for the first position, shown in Fig. 6.10, demonstrates the low density of the output data points, simulated by the RT in the simple geometrical model. In contrast, the scenario captured by the photogrammetry technique produces a better match. This also holds true for other positions of the receiver as well. The reason for that is the disparate number of objects scatters the signal, which, in turn, arises from the different level of detail in these two scenarios.

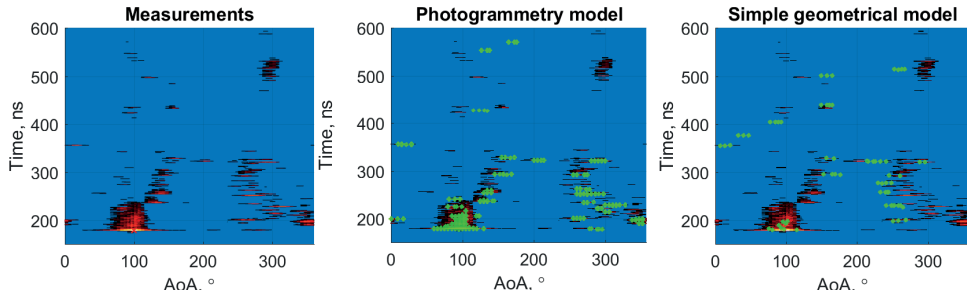


Figure 6.10 Comparison of measured versus simulated (green points) PADP [115].

By using the same PADPs, the MPCs are determined and matched with those obtained from the measurements. Based on this, the mean differences between the RT results for the accurate and simple 3D deployments and those obtained by the measurements are summarized in Tab. 6.2. It is clear that the difference is less with the accurate model, which demonstrates the better performance of the photogrammetry method compared to the simplified Google Map model. Thus, it is recommended that this model should be utilized to capture an accurate 3D model of scenarios for RT simulations.

Table 6.2 Comparison between simple and accurate Models [115].

Pos	Simple			Accurate		
	AoA	Time	Power	AoA	Time	Power
1	3.2	1.2	-7.3	2.1	1.1	-3.1
2	3.8	2.2	-5.1	3.0	2.0	-2.9
3	4.7	3.5	-8.2	3.1	3.1	-3.3
4	4.0	2.9	-4.1	3.9	2.4	-2.0
5	2.2	1.6	-6.7	2.1	0.9	-2.1
6	3.9	2.6	-5.9	2.9	2.0	-2.4

Finally, the RT simulation of the PDP was executed for both the deployments and compared to the measured ones. The results for the first receiver position are shown in Fig. 6.11. It can be seen that a more detailed scenario (the solid black line) shows better agreement with the measured results (thick solid grey line).

This observation reveals an underlying fundamental problem which will be explained further. Nowadays, simplified 3D models are commonly utilized as input

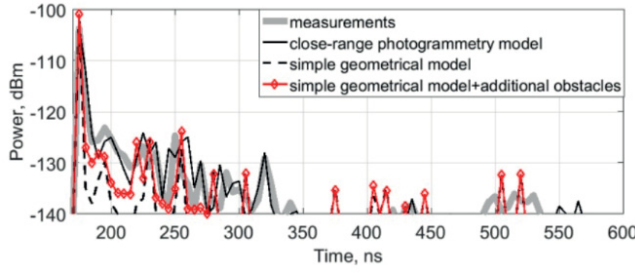


Figure 6.11 Comparison between PDPs obtained by measurement and by RT-simulations of simple and accurate scenarios [115].

data for RT. In principle, such an approximation is adequate to assess the integral (e.g. total received power) or average (e.g. mean time) channel metrics, in most cases. However, when the multipath propagation is the primary target of the research, then even a small object may change the channel statistics. Therefore, neglecting the details of a scenario is to be avoided at mmWave frequencies, since the <1 cm wavelength experiences excellent reflectivity from objects as small as 10 cm.

6.7 Wave Propagation in Urban Deployment with Vehicular Blockage

The three main objectives of this research were as follows: i) to characterize the blockage effect caused by vehicles in an urban canyon scenario, ii) to calibrate the proposed RT, iii) to investigate alternative communication paths in an urban canyon scenario when the LOS link is obstructed by a vehicle. Eight deployments as specified in Sec. 5.4 were simulated by our RT described in Sec. 4.1 and measured by the 28 GHz sounding equipment described in Sec. 4.3.

As it is derived from the PADP metrics, the excess loss value is utilized to characterize the blocking effect caused by the vehicle, as well as to identify any backup propagation paths around the vehicle when the LOS is obstructed. Table 6.3 summarizes the propagation paths and the excess loss values discovered in all eight of the deployments by measurement and simulation. As an example, Fig. 6.12 depicts the paths identified in calibration Scenario 1. As can be seen from Tab. 6.3, the highest measured diffraction around the vehicle is 21.5 dB and 24.1 dB, which prevents it from being a good alternative path. In contrast, the single order reflection from the

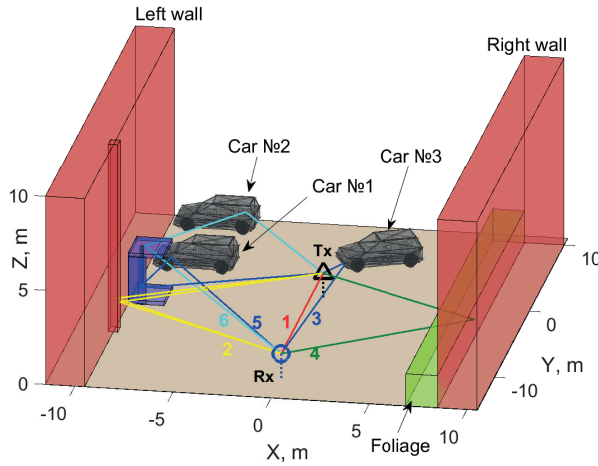


Figure 6.12 Propagation paths in the Scenario 1 [94].

brick wall has the lowest measured 3.4 dB and 5 dB excess loss value, making it the primary communication mechanism to replace the LOS path. However, it should be noted that if any foliage grows near the wall, the loss value increases up to 19 dB due to the attenuation.

Table 6.3 Measurement results of excess loss for different propagation mechanisms in an urban street canyon [94].

Physical effect	Scenario and setup	Meas.Exc. loss	Sim.Exc. loss	Difference
LOS	12 m separation (Sc1)	0 dB	0 dB	0 dB
	10 m separation (Sc2)	0 dB	0 dB	0 dB
Reflection	From the brick (Sc1)	3.4 dB	3.1 dB	+0.3 dB
	From the car (Sc3)	5 dB	2.8 dB	+2.2 dB
	From the door (Sc6)	11.7 dB	11.0 dB	+0.7 dB
Transmission	1 car along (Sc3)	4.5 dB	6.7dB	-2.2 dB
	2 cars along (Sc4)	16.5 dB	13.3 dB	+3.2 dB
	2 cars side (Sc5)	9.5 dB	10.8 dB	-1.3 dB
	1 car at 45° (Sc6)	7.5 dB	5.5 dB	+2.0 dB
Diffraction	1 car, 12 m sep. (Sc7)	21.5 dB	23.1 dB	-1.6 dB
	1 car, 10 m sep. (Sc8)	24.1 dB	24.5 dB	-0.4 dB
Scattering	foliage, 12 m sep. (Sc1)	19.4 dB	15.2 dB	+4.2 dB
	foliage, 10 m sep. (Sc2)	16.4 dB	12.1 dB	+4.3 dB

Additional propagation phenomena, such as the transmission of the signal through the cabin of the vehicle, is examined by measuring the real vehicle and the simulation of a highly-detailed car model. The results of this are shown in Fig. 6.13. The plot suggests that the interior elements of the vehicle produce fluctuations in the total received power up to the level of 25 dB on the RX. The maximum excess loss is achieved when the signal is blocked by the front and rear standing pillars of the vehicle body. Moreover, a protective film glued to the surface of the windscreen may add up to 10 dB of extra excess loss. The outcome of our investigation is that signal transmission through a car is possible when the front and rear windshields are in place and made of clear glass. However, this phenomenon is more likely to conform to probabilistic behaviour, since there is a non-zero probability of the signal being blocked by interior elements. Therefore, transmission through a car may not have the highest priority when selecting alternative paths in beam-searching procedures.

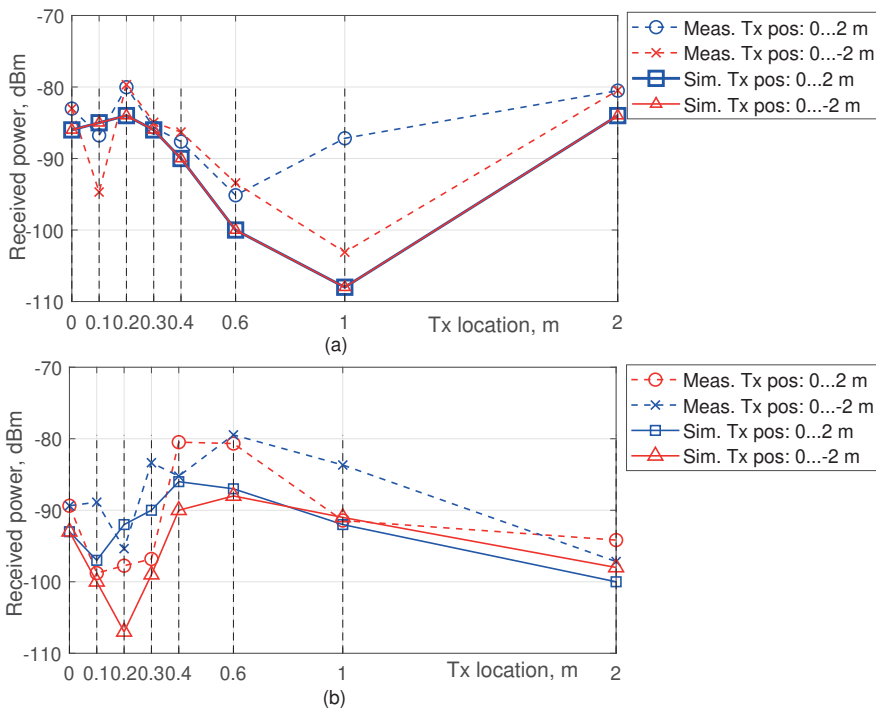


Figure 6.13 Comparison between measured and simulated transmission through cabin [94].

In turn, the position of the mirrors, the seats, the curvature of the windows, and the relative antenna positions can influence the output results of an RT simulation.

Since it is quite challenging to reproduce the 3D model in full, the average inaccuracy of the simulation results is around 8 dB (see Fig. 6.13).

The measured and simulated PADPs were also compared to each other to calibrate the proposed RT tool. The heat-maps shown in Fig. 6.14 show the PADPs obtained in Scenario 3. The modelled data accurately reflects the measured data in both temporal and angular coordinates. The RT also distinguished two almost identical reflecting paths between the left wall and the vehicle (square 2 in Fig. 6.14).

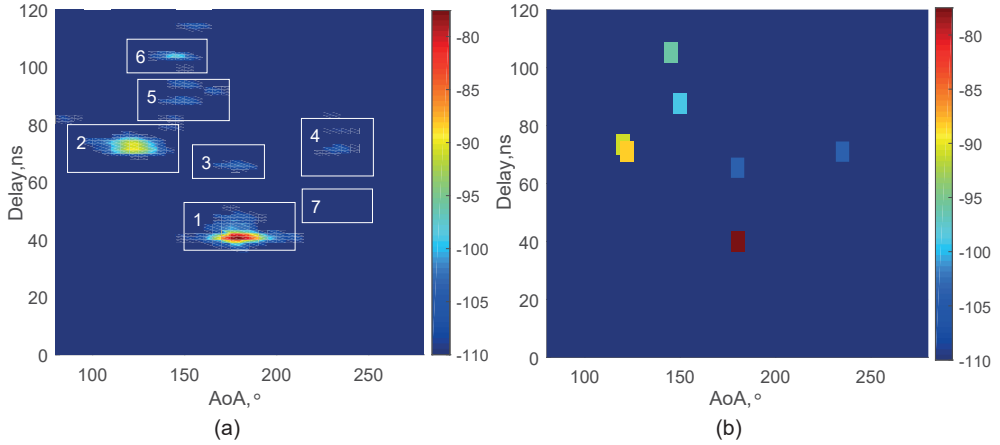


Figure 6.14 Comparison of measured and simulated PADPs (modified from [94]).

Moreover, the RT helped to recognize the propagation mechanism in square 4, which might be caused by: i) reflection from the right wall and attenuation in the foliage, ii) diffuse scattering from the foliage without interaction with the right-hand wall. The propagation delay should be compared first in order to determine which one creates the MPC in square 4. Because the link TX-RX is located in the centre of the street, the MPCs in squares 2 and 4 have identical propagation delay. Consequently, the first mechanism is activated and the proper model accounting for foliage attenuation is used.

7 CONCLUSION

7.1 Summary of Completed Work

In this thesis, a methodology has been developed that characterizes the radio-wave propagation and evaluate the performance of mmWave networks. Recently, our RT methodology has started to be actively exploited in a computing cluster, consisting of eight hosts and 64 nodes in total. The implemented parallelization of concurrent processes enables calculation of complex deployments more than $\times 10$ times faster, which, in the future, also opens up opportunities even for the analysis of moving objects.

However, the same as other deterministic models, the RT-based methodology requires a detailed input model of a 3D scenario. Moreover, a relatively small wavelength at the mmWave gains this demand. To this end, the photogrammetry technique was proposed, that captures a 3D scenario more accurately than the typical Google map services. It grants a more qualitative analysis of communication systems, where the channel-state information plays a vital role (for example, the beam-managing algorithms).

Because of a short wavelength, the mmWave band may 'feel' a surface roughness, which leads to the formation of scattered components. In the framework of this thesis, a RT model was introduced that characterize the power and polarization effects of the diffuse scattering. As a result, the power contribution and depolarization effects in urban Manhattan grid deployments were studied

The densification of mmWave networks is the primary way to solve the problem of significant losses in the wireless channel. However, this cannot be done intensively, since the networks may switch from noise-limited to interference-limited regimes. In this thesis, we demonstrated the application of the RT-based framework for the massive simulation and evaluated in which conditions the mmWave network operates in the interference or noise regimes.

7.2 The RT in 5G mmWave

The research carried out within the framework of this thesis has enabled a critical evaluation of RT capabilities for modelling 5G mmWave networks. For example, globally RT is an appropriate tool for resolving a number of practical tasks. Unlike analytical or empirical models, which mainly support idealized scenarios, RT accurately characterizes a specific real-life deployment with measurable metrics (Sec. 6.7 and Sec. 6.6), such as VNA or multimeters, for instance. Moreover, RT can successfully complement or add accuracy to other existing methods. For instance, it may interpret measured results and append any missing information. Additionally, RT can successfully be employed to parametrize the analytical or empirical models using some fine-tuning parametrizing coefficients.

Unlike full-wave methods, RT works consistently in the promising mmWave 28 GHz–100 GHz range. Since GO was initially constructed to describe the behavior of photons (see Sec. 3.1.1), a step up to the THz spectrum is theoretically justified. Finally, RT efficiently supports the simulation of an ultra-wideband signal (Sec. 6.6) as well.

Ultimately, it is the simulations of depolarization which look most challenging, since this effect depends on many factors such as spatial density, materials, and the distribution, size and orientation of any surrounding objects (Sec. 6.5). Unfortunately, at present there are no alternative methods for RT to simulate this phenomenon accurately at an acceptable speed. Despite the fact that 3GPP proposes a model to describe the depolarization effect [112], its simplicity renders it unable to solve many practical tasks as it does not take site-specific conditions into account.

The widespread use of antenna arrays opens up a number of new practical problems that might successfully be solved by the use of RT. For example, all of the beam management algorithms require an appropriate beam pattern for the channel-state information to be selected from the codebook (Sec. 6.4 and 6.5). In contrast to other analytical models, which do not account for the spatial environmental specifics, RT has huge potential to verify a particular beam-tracking algorithm in any environment, including mobile ones.

Given all the facts obtained from this research, it seems reasonable to assert that RT is a very accurate and flexible method to characterize the wireless channels of mmWave networks. It has excellent capabilities for investigating mmWave 5G, and

beyond. As the number of carrier frequencies increases and the cost of computational calculation falls, the demand for RT will rise in the future.

7.3 Potential Improvements of the RT

This research has identified several directions in which RT will intensively progress.

Utilization of Platforms. Graphics and gaming platforms should be actively exploited for RT implementations. This avoids the need to develop many routine functions such as displaying, converting or transforming faceted 3D models. Such platforms enable the use of different types of static and dynamic mmWave 5G deployments as they are relatively fast and are built on flexible and user-friendly architectures.

Extra Physical Models. The propagation mechanisms associated with a small wavelength, such as depolarization, diffuse scattering and the impact of foliage become visible at the mmWave level. Although many such models already exist, more comprehensive parametrization using actual measurements should be performed in the future. It is also clear that such a short wavelength requires more accurate scenarios, since even a small object such as a cup on a table may produce a reasonably good reflection at mmWave frequencies.

Hybridization RT is well suited to be combined with other deterministic and stochastic models. For example, aggregation with the FDTD method may enable the calculation of both far- and near-field EM fields. Hybridization with stochastic EM fields is commonly related to the calculation of diffuse scattering and other weak phenomena.

REFERENCES

- [1] *Ericsson Mobility Report*. Oct. 2018. URL: <https://www.ericsson.com/4932c2/assets/local/mobility-report/documents/2019/emr-q4-update-2018.pdf>.
- [2] *Cisco Visual Networking Index: Global Mobile Data Traffic Forecast Update, 2017–2022 White Paper*. Feb. 2019. URL: <https://www.cisco.com/c/en/us/solutions/collateral/service-provider/visual-networking-index-vni/white-paper-c11-738429.html>.
- [3] T. S. Rappaport, S. Sun, R. Mayzus, H. Zhao, Y. Azar, K. Wang, G. N. Wong, J. K. Schulz, M. Samimi and F. Gutierrez. "Millimeter wave mobile communications for 5G cellular: It will work!": *IEEE Access* 1 (2013), 335–349.
- [4] F. Hu. *Opportunities in 5G networks: A research and development perspective*. CRC Press, 2016.
- [5] T. S. Rappaport, Y. Xing, G. R. MacCartney, A. F. Molisch, E. Mellios and J. Zhang. Overview of millimeter wave communications for fifth-generation (5G) wireless networks—with a focus on propagation models. *IEEE Transactions on Antennas and Propagation* 65.12 (2017), 6213–6230.
- [6] A. Osseiran, F. Boccardi, V. Braun, K. Kusume, P. Marsch, M. Maternia, O. Queseth, M. Schellmann, H. Schotten, H. Taoka et al. Scenarios for 5G mobile and wireless communications: the vision of the METIS project. *IEEE Communications Magazine* 52.5 (2014), 26–35.
- [7] *Samsung Electronics Sets 5G Speed Record at 7.5 Gbps, Over 30 Times Faster Than 4G LTE*. Oct. 2014. URL: <https://www.samsung.com/global/business/networks/insights/news/samsung-electronics-sets-5g-speed-record-at-7-5gbps-over-30-times-faster-than-4g-lte/>.

- [8] *Nokia Networks showcases 5G speed of 10Gbps with NI at the Brooklyn 5G Summit.* Apr. 2015. URL: <https://www.nokia.com/about-us/news/releases/2015/04/08/nokia-networks-showcases-5g-speed-of-10gbps-with-ni-at-the-brooklyn-5g-summit/>.
- [9] *Mitsubishi Electric and NTT DOCOMO Achieve World's First 27Gbps Throughput in 5G Outdoor Trials.* Nov. 2018. URL: https://www.nttdocomo.co.jp/english/info/media_center/pr/2018/1122_00.html.
- [10] *Samsung, Qualcomm and Verizon Showcase Rapid Progress Towards 5G NR Commercialization.* Dec. 2018. URL: <https://news.samsung.com/us/samsung-qualcomm-verizon-demonstration-spotlighting-rapid-progress>.
- [11] S. Rangan, T. S. Rappaport and E. Erkip. Millimeter wave cellular wireless networks: Potentials and challenges. *IEEE Proceedings* 102.3 (2014).
- [12] A. Ghosh, T. A. Thomas, M. C. Cudak, R. Ratasuk, P. Moorut, F. W. Vook, T. S. Rappaport, G. R. MacCartney, S. Sun and S. Nie. Millimeter-wave enhanced local area systems: A high-data-rate approach for future wireless networks. *IEEE Journal on Selected Areas in Communications* 32.6 (2014), 1152–1163.
- [13] P. F. Smulders and L. Correia. Characterisation of propagation in 60 GHz radio channels. *Electronics & Communication Engineering Journal* 9.2 (1997), 73–80.
- [14] M. Shafi, J. Zhang, H. Tataria, A. F. Molisch, S. Sun, T. S. Rappaport, F. Tufvesson, S. Wu and K. Kitao. Microwave vs. millimeter-Wave propagation channels: Key differences and impact on 5G cellular systems. *IEEE Communications Magazine* 56.12 (2018), 14–20.
- [15] J.-J. Park, J. Lee, K.-W. Kim, K.-C. Lee and M.-D. Kim. Vehicle antenna position dependent path loss for millimeter-wave V2V communication. *IEEE 11th Global Symposium on Millimeter Waves (GSMM)*. 2018, 1–3.
- [16] Q. Xue, P. Zhou, X. Fang and M. Xiao. Performance analysis of interference and eavesdropping immunity in narrow beam mmWave networks. *IEEE Access* 6 (2018), 67611–67624.

- [17] N. Valliappan, A. Lozano and R. W. Heath. Antenna subset modulation for secure millimeter-wave wireless communication. *IEEE Transactions on Communications* 61.8 (2013), 3231–3245.
- [18] A. F. Molisch. *Wireless communications*. John Wiley & Sons, 2012.
- [19] A. Karttunen, J. Järveläinen, S. L. H. Nguyen and K. Haneda. Modeling the multipath cross-polarization ratio for 5 to 80 GHz radio links. *IEEE Transactions on Wireless Communications* (2019).
- [20] X. Mao, J. Jin and J. Yang. Wireless channel modeling methods: Classification, comparison and application. *IEEE 5th International Conference on Computer Science & Education*. 2010, 1669–1673.
- [21] S.-K. Yong, P. Xia and A. Valdes-Garcia. *60 GHz technology for Gbps WLAN and WPAN: from theory to practice*. John Wiley & Sons, 2011.
- [22] X. Yin and X. Cheng. *Propagation channel characterization, parameter estimation, and modeling for wireless communications*. John Wiley & Sons, 2016.
- [23] R. Aquino-Santos. *Wireless technologies in vehicular ad hoc networks: Present and future challenges: present and future challenges*. IGI Global, 2012.
- [24] A. G. Kanatas, K. S. Nikita and P. T. Mathiopoulos. *New directions in wireless communications systems: From mobile to 5G*. CRC Press, 2017.
- [25] G. R. MacCartney, J. Zhang, S. Nie and T. S. Rappaport. Path loss models for 5G millimeter wave propagation channels in urban microcells. *IEEE Global Communications Conference (GLOBECOM)*. 2013, 3948–3953.
- [26] M. K. Samimi and T. S. Rappaport. 3-D millimeter-wave statistical channel model for 5G wireless system design. *IEEE Transactions on Microwave Theory and Techniques* 64.7 (2016), 2207–2225.
- [27] S. Hur, S. Baek, B. Kim, Y. Chang, A. F. Molisch, T. S. Rappaport, K. Haneda and J. Park. Proposal on millimeter-wave channel modeling for 5G cellular system. *IEEE Journal of Selected Topics in Signal Processing* 10.3 (2016), 454–469.
- [28] G. Steinböck, A. Karstensen, P. Kyösti and A. Hekkala. A 5G hybrid channel model considering rays and geometric stochastic propagation graph. *IEEE 27th Annual International Symposium on Personal, Indoor, and Mobile Radio Communications (PIMRC)*. 2016, 1–6.

- [29] L. Tian, V. Degli-Esposti, E. M. Vitucci and X. Yin. Semi-deterministic radio channel modeling based on graph theory and ray-tracing. *IEEE Transactions on Antennas and Propagation* 64.6 (2016), 2475–2486.
- [30] G. Steinböck, M. Gan, P. Meissner, E. Leitinger, K. Witrisal, T. Zemen and T. Pedersen. Hybrid model for reverberant indoor radio channels using rays and graphs. *IEEE Transactions on Antennas and Propagation* 64.9 (2016), 4036–4048.
- [31] *METIS channel models*. Deliverable ICT-317669-METIS/D1.4. METIS, 2015.
- [32] *Channel Modeling and Characterization*. Deliverable FP7-ICT-368721/D5.1. MiWEBA, 2014.
- [33] G. R. Maccartney, T. S. Rappaport, S. Sun and S. Deng. Indoor office wide-band millimeter-wave propagation measurements and channel models at 28 and 73 GHz for ultra-dense 5G wireless networks. *IEEE Access* 3 (2015), 2388–2424.
- [34] T. S. Rappaport, G. R. MacCartney, M. K. Samimi and S. Sun. Wideband millimeter-wave propagation measurements and channel models for future wireless communication system design. *IEEE Transactions on Communications* 63.9 (2015), 3029–3056.
- [35] M. K. Samimi and T. S. Rappaport. Local multipath model parameters for generating 5G millimeter-wave 3GPP-like channel impulse response. *IEEE 10th European Conference on Antennas and Propagation (EuCAP)*. 2016, 1–5.
- [36] *6–100 GHz channel modelling for 5G: Measurement and modelling plans in mm-MAGIC*. White Paper ICT-671650-mmMAGIC/W2.1. mmMAGIC, 2016.
- [37] S. Jaeckel, L. Raschkowski, K. Börner and L. Thiele. QuaDRiGa: A 3-D multi-cell channel model with time evolution for enabling virtual field trials. *IEEE Transactions on Antennas and Propagation* 62.6 (2014), 3242–3256.
- [38] *Spatial Channel Model for Multiple Input Multiple Output (MIMO) Simulations*. Technical Report TR 25.996 V12.0.0. 3GPP, 2014.
- [39] *WINNER II Channel Models*. Deliverable IST-4-027756/D1.1.2 V1.2. WINNER, 2007.

- [40] S. Sun, T. S. Rappaport, M. Shafi, P. Tang, J. Zhang and P. J. Smith. Propagation models and performance evaluation for 5G millimeter-wave bands. *IEEE Transactions on Vehicular Technology* 67.9 (2018), 8422–8439.
- [41] Y. Yu, Y. Liu, W.-J. Lu and H.-B. Zhu. Propagation model and channel simulator under indoor stair environment for machine-to-machine applications. *IEEE Asia-Pacific Microwave Conference (APMC)*. Vol. 2. IEEE. 2015, 1–3.
- [42] *Trends in the Cost of Computing*. URL: <https://aiimpacts.org/trends-in-the-cost-of-computing/>.
- [43] *NVIDIA web-site*. URL: <https://www.nvidia.com>.
- [44] F. Fuschini, M. Zoli, E. M. Vitucci, M. Barbiroli and V. Degli-Esposti. A study on millimeter-wave multiuser directional beamforming based on measurements and Ray tracing simulations. *IEEE Transactions on Antennas and Propagation* 67.4 (2019), 2633–2644.
- [45] D. He, B. Ai, K. Guan, L. Wang, Z. Zhong and T. Kürner. The design and applications of high-performance ray-tracing simulation platform for 5G and beyond wireless communications: A tutorial. *IEEE Communications Surveys & Tutorials* 21.1 (2018), 10–27.
- [46] J. S. Lu, E. M. Vitucci, V. Degli-Esposti, F. Fuschini, M. Barbiroli, J. A. Blaha and H. L. Bertoni. A discrete environment-driven GPU-based Ray Launching algorithm. *IEEE Transactions on Antennas and Propagation* 67.2 (2019), 1180–1192.
- [47] *Remcom Wireless InSite*. URL: <https://www.remcom.com/wireless-insite-em-propagation-software>.
- [48] *Wireless InSite Features. Diffuse scattering*. URL: <https://www.remcom.com/wireless-insite-diffuse-scattering>.
- [49] *5G and MIMO Simulation Software*. URL: <https://www.remcom.com/5g-mimo>.
- [50] *WinProp - Propagation Modeling*. URL: <https://altairhyperworks.com/product/Feko/WinProp-Propagation-Modeling>.
- [51] *Ranplan*. URL: <https://ranplanwireless.com/>.
- [52] *Forsk Atoll*. URL: <https://www.forsk.com/>.

- [53] D. B. Davidson. *Computational electromagnetics for RF and microwave engineering*. Cambridge University Press, 2010.
- [54] K. S. Kunz. *The finite difference time domain method for electromagnetics*. Technology and Engineering, 2018.
- [55] *Ansys HFSS web-site*. URL: <https://www.ansys.com/products/electronics/ansys-hfss>.
- [56] *CST web-site*. URL: <https://www.cst.com/>.
- [57] *EMPro 3DEM web-site*. URL: <https://www.keysight.com/en/pc-1297143/empro-3d-em-simulation-software?cc=FI&lc=fin>.
- [58] *SEMCAD web-site*. URL: <https://speag.swiss/products/semcad/solutions/>.
- [59] D. A. McNamara, J. Malherbe and C. W. Pistorius. *Introduction to the uniform geometrical theory of diffraction*. Artech House, 1990.
- [60] B. H. Walker. *Optical engineering fundamentals*. Vol. 82. Spie Press Bellingham, 2008.
- [61] R. K. Verma. *Ray optics*. Discovery Publishing House, 2006.
- [62] B. S. Guru and H. R. Hiziroglu. *Electromagnetic field theory fundamentals*. Cambridge university press, 2009.
- [63] M. Kline. *Electromagnetic theory and geometrical optics*. Tech. rep. Air Force Cambridge Research Labs, 1962.
- [64] J. B. Keller. Geometrical theory of diffraction. *Josa* 52.2 (1962), 116–130.
- [65] R. G. Kouyoumjian and P. H. Pathak. A uniform geometrical theory of diffraction for an edge in a perfectly conducting surface. *IEEE Proceedings* 62.11 (1974), 1448–1461.
- [66] R. C. Dorf. *The electrical engineering handbook*. CRC Press, 1997.
- [67] A. Sommerfeld and J. Runge. Anwendung der vektorrechnung auf die Grundlagen der geometrischen optik. *Annalen der Physik* 340.7 (1911), 277–298.
- [68] R. Luneberg. *Mathematical theory of optics*. 1944.
- [69] M. Kline. An asymptotic solution of Maxwell’s equations. *Communications on Pure and Applied Mathematics* 4.2-3 (1951), 225–262.
- [70] A. Sommerfeld. *Lectures on Theoretical Physics: Optics*. Academic Press, 1954.

- [71] V. Lakshminarayanan, A. Ghatak and K. Thyagarajan. *Lagrangian optics*. Springer Science & Business Media, 2013.
- [72] G. A. Deschamps. Ray techniques in electromagnetics. *IEEE Proceedings* 60.9 (1972), 1022–1035.
- [73] A. S. Glassner. *An introduction to ray tracing*. Elsevier, 1989.
- [74] L. Azpilicueta, M. Rawat, K. Rawat, F. M. Ghannouchi and F. Falcone. A ray launching-neural network approach for radio wave propagation analysis in complex indoor environments. *IEEE Transactions on Antennas and Propagation* 62.5 (2014), 2777–2786.
- [75] L. Azpilicueta, F. Falcone and R. Janaswamy. A hybrid ray launching-diffusion equation approach for propagation prediction in complex indoor environments. *IEEE Antennas and Wireless Propagation Letters* 16 (2016), 214–217.
- [76] F. Casino, L. Azpilicueta, P. Lopez-Iturri, E. Aguirre, F. Falcone and A. Solanas. Optimized wireless channel characterization in large complex environments by hybrid ray launching-collaborative filtering approach. *IEEE Antennas and Wireless Propagation Letters* 16 (2016), 780–783.
- [77] G. Durgin, N. Patwari and T. S. Rappaport. An advanced 3D ray launching method for wireless propagation prediction. *IEEE 47th Vehicular Technology Conference. Technology in Motion*. Vol. 2. 1997, 785–789.
- [78] Z. Lai, N. Bessis, G. De La Roche, P. Kuonen, J. Zhang and G. Clapworthy. A new approach to solve angular dispersion of discrete ray launching for urban scenarios. *Loughborough Antennas & Propagation Conference*. IEEE. 2009, 133–136.
- [79] F. A. Agelet, A. Formella, J. H. Rabanos, F. I. De Vicente and F. P. Fontan. Efficient ray-tracing acceleration techniques for radio propagation modeling. *IEEE transactions on Vehicular Technology* 49.6 (2000), 2089–2104.
- [80] P. Combeau, L. Aveneau, R. Vauzelle and Y. Pousset. Efficient 2-D ray-tracing method for narrow and wideband channel characterisation in microcellular configurations. *Proceedings-Microwaves, Antennas and Propagation* 153.6 (2006), 502–509.

- [81] T. Alwajeeh, P. Combeau, R. Vauzelle and A. Bounceur. A high-speed 2.5 D ray-tracing propagation model for microcellular systems, application: Smart cities. *IEEE 11th European Conference on Antennas and Propagation (EuCAP)*. 2017, 3515–3519.
- [82] M. Catedra, J. Perez, F. S. De Adana and O. Gutierrez. Efficient ray-tracing techniques for three-dimensional analyses of propagation in mobile communications: application to picocell and microcell scenarios. *IEEE Antennas and Propagation Magazine* 40.2 (1998), 15–28.
- [83] J.-K. Bang, B.-C. Kim, S.-H. Suk, K.-S. Jin and H.-T. Kim. Time consumption reduction of ray tracing for RCS prediction using efficient grid division and space division algorithms. *Journal of Electromagnetic Waves and Applications* 21.6 (2007), 829–840.
- [84] H. Kim and H.-S. Lee. Accelerated three dimensional ray tracing techniques using ray frustums for wireless propagation models. *Progress In Electromagnetics Research* 96 (2009), 21–36.
- [85] E. M. Kenny and E. O. Nuallain. Convex space building discretization for ray-tracing. *IEEE Transactions on Antennas and Propagation* 65.5 (2017), 2578–2591.
- [86] D. Shi, X. Tang, C. Wang, M. Zhao and Y. Gao. A GPU implementation of a shooting and bouncing ray tracing method for radio wave propagation. *Applied Computational Electromagnetics Society Journal* 32.7 (2017).
- [87] A. M. Cavalcante, M. J. de Sousa, J. C. W. A. Costa, C. R. L. Frances and G. P. dos Santos Cavalcante. A new computational parallel model applied in 3D ray-tracing techniques for radio-propagation prediction. *IEEE Asia-Pacific Microwave Conference*. 2006, 1859–1862.
- [88] A. M. Cavalcante, M. J. de Sousa, J. C. W. A. Costa, C. R. L. Francês, G. P. dos Santos Cavalcante and C. de Souza Sales. 3D ray-tracing parallel model for radio-propagation prediction. *International Telecommunications Symposium*. IEEE. 2006, 269–274.
- [89] W. Burnside and K. Burgener. High frequency scattering by a thin lossless dielectric slab. *IEEE Transactions on Antennas and Propagation* 31.1 (1983), 104–110.

- [90] A. Aragón-Zavala. *Indoor wireless communications: From theory to implementation*. John Wiley & Sons, 2017.
- [91] V. Degli-Esposti, D. Guiducci, A. de’Marsi, P. Azzi and F. Fuschini. An advanced field prediction model including diffuse scattering. *IEEE Transactions on Antennas and Propagation* 52.7 (2004), 1717–1728.
- [92] *Specific attenuation model for rain for use in prediction methods*. Recommendation ITU-R P.838-3. ITU, 2005.
- [93] *Attenuation in vegetation*. Recommendation ITU-R P.833-4. ITU, 2016.
- [94] D. Solomitckii, V. Semkin, A. Karttunen, V. Petrov, S. Nguyen, H. Nikopour, K. Haneda, S. Andreev, S. Talwar and Y. Koucheryavy. Characterizing Radio Wave Propagation in Urban Street Canyon with Vehicular Blockage at 28 GHz. *IEEE Transaction on Vehicular Technologies* (2019). Accepted, to appear.
- [95] B. Smits. Efficiency issues for ray tracing. *Journal of Graphics Tools* 3.2 (1998), 1–14.
- [96] D. Badouel. An efficient ray-polygon intersection. *Graphics Gems*. Academic Press Professional, Inc. 1990, 390–393.
- [97] E. M. Vitucci, F. Mani, V. Degli-Esposti and C. Oestges. Polarimetric properties of diffuse scattering from building walls: Experimental parameterization of a ray-tracing model. *IEEE Transactions on Antennas and Propagation* 60.6 (2012), 2961–2969.
- [98] E. Borodina and M. Salin. Estimation of space-time characteristics of surface roughness based on video images. *Izvestiya, Atmospheric and Oceanic Physics* 46.2 (2010), 239–248.
- [99] Y. M. Altman. *Accelerating MATLAB Performance: 1001 tips to speed up MATLAB programs*. Chapman and Hall/CRC, 2014.
- [100] M. Rebato, M. Mezzavilla, S. Rangan, F. Boccardi and M. Zorzi. Understanding noise and interference regimes in 5G millimeter-wave cellular networks. *European Wireless 2016; 22th European Wireless Conference*. VDE. 2016, 1–5.
- [101] D. Solomitckii, M. Gapeyenko, S. Szyszkowicz, S. Andreev, H. Yanikomeroglu and Y. Koucheryavy. Toward massive ray-based simulations of mmWave small cells on open urban maps. *IEEE Antennas and Wireless Propagation Letters* 16 (2016), 1435–1438. DOI: 10.1109/LAWP.2016.2641339.

- [102] R. Naderpour, J. Vehmas, S. Nguyen, J. Järveläinen and K. Haneda. Spatio-temporal channel sounding in a street canyon at 15, 28 and 60 GHz. *IEEE 27th Annual International Symposium on Personal, Indoor, and Mobile Radio Communications (PIMRC)*. 2016, 1–6.
- [103] D. Solomitchii, V. Petrov, H. Nikopour, M. Akdeniz, O. Orhan, N. Himayat, S. Talwar, S. Andreev and Y. Koucheryavy. Detailed interference analysis in dense mmWave systems employing dual-polarized antennas. *IEEE Globecom Workshops (GC Wkshps)*. 2017. DOI: 10.1109/GLOCOMW.2017.8269040.
- [104] S.-C. Lin and I. F. Akyildiz. Dynamic base station formation for solving NLOS problem in 5G millimeter-wave communication. *IEEE Conference on Computer Communications (INFOCOM)*. 2017, 1–9.
- [105] G. R. MacCartney and T. S. Rappaport. Rural macrocell path loss models for millimeter wave wireless communications. *IEEE Journal on Selected Areas in Communications* 35.7 (2017), 1663–1677.
- [106] Y. Wang, K. Venugopal, A. F. Molisch and R. W. Heath. mmWave vehicle-to-infrastructure communication: Analysis of urban microcellular networks. *IEEE Transactions on Vehicular Technology* 67.8 (2018), 7086–7100.
- [107] D. Solomitchii, Q. C. Li, T. Balercia, C. R. da Silva, S. Talwar, S. Andreev and Y. Koucheryavy. Characterizing the Impact of Diffuse Scattering in Urban Millimeter-Wave Deployments. *IEEE Wireless Communications Letters* 5.4 (2016), 432–435. DOI: 10.1109/LWC.2016.2580669.
- [108] *Simulation guidelines*. Deliverable ICT-317669-METIS/D6.1. METIS, 2013.
- [109] *Study on channel model for frequency spectrum above 6 GHz*. Technical Report TR 38.900 ver. 14.2.0 Rel. 14. 3GPP, 2016.
- [110] M. Peter et al. Measurement results and final mmMAGIC channel models. *Deliverable D2 2* (2017).
- [111] G. R. MacCartney, T. S. Rappaport and A. Ghosh. Base station diversity propagation measurements at 73 GHz millimeter-wave for 5G coordinated multipoint (CoMP) analysis. *IEEE Globecom Workshops (GC Wkshps)*. 2017, 1–7.

- [112] *Propagation data and prediction methods for the planning of indoor radiocommunication systems and radio local area networks in the frequency range 900 MHz to 100 GHz*. Recommendation ITU-R P.1238. ITU, 2012.
- [113] *OpenStreetMap Project*. URL: <https://www.openstreetmap.org/>.
- [114] S. S. Szyszkowicz, A. Lou and H. Yanikomeroglu. Automated placement of individual millimeter-wave wall-mounted base stations for line-of-sight coverage of outdoor urban areas. *IEEE Wireless Communications Letters* 5.3 (2016), 316–319.
- [115] V. Semkin, D. Solomitckii, R. Naderpour, S. Andreev, Y. Koucheryavy and A. V. Räisänen. Characterization of radio links at 60 GHz using simple geometrical and highly accurate 3-D models. *IEEE Transactions on Vehicular Technology* 66.6 (2016), 4647–4656. DOI: 10.1109/TVT.2016.2617919.
- [116] *PTC Web-site*. URL: <https://www.ptc.com/en/products/cad/creo>.
- [117] J. Lu, D. Steinbach, P. Cabrol, P. Pietraski and R. V. Pragada. Propagation characterization of an office building in the 60 GHz band. *IEEE 8th European Conference on Antennas and Propagation (EuCAP)*. 2014, 809–813.
- [118] D. Solomitckii, M. Gapeyenko, V. Semkin, S. Andreev and Y. Koucheryavy. Technologies for efficient amateur drone detection in 5G millimeter-wave cellular infrastructure. *IEEE Communications Magazine* 56.1 (2018), 43–50. DOI: 10.1109/MCOM.2017.1700450.
- [119] M. D. Janezic and J. A. Jargon. Complex permittivity determination from propagation constant measurements. *IEEE Microwave and Guided Wave Letters* 9.2 (1999), 76–78.
- [120] *Effects of building materials and structures on radiowave propagation above about 100 MHz*. Recommendation ITU-R P.2040-1. ITU, 2016.
- [121] *Study on channel model for frequencies from 0.5 to 100 GHz*. Tech. rep. TR 38.901 ver. 14.0.0 Rel. 14. 3GPP, 2017.
- [122] K. Rubrice, X. Castel, M. Himdi and P. Parneix. Dielectric characteristics and microwave absorption of graphene composite materials. *Materials* 9.10 (2016), 825.

- [123] D. Solomitckii, V. Petrov, H. Nikopour, M. Akdeniz, O. Orhan, N. Himayat, S. Talwar, S. Andreev and Y. Koucheryavy. Ray-Based Evaluation of Dual-Polarized MIMO in (Ultra-) Dense Millimeter-Wave Urban Deployments. *IEEE 87th Vehicular Technology Conference (VTC Spring)*. 2018. DOI: 10.1109/VTCSpring.2018.8417788.
- [124] J. Lekner. *Theory of reflection: Reflection and transmission of electromagnetic, particle and acoustic Waves*. Vol. 87. Springer, 2016.

PUBLICATIONS

PUBLICATION

I

Characterizing the Impact of Diffuse Scattering in Urban Millimeter-Wave Deployments

D. Solomitckii, Q. C. Li, T. Balercia, C. R. da Silva, S. Talwar, S. Andreev and
Y. Koucheryavy

IEEE Wireless Communications Letters 5.4 (2016), 432–435

DOI: 10.1109/LWC.2016.2580669

Publication reprinted with the permission of the copyright holders

Characterizing the Impact of Diffuse Scattering in Urban Millimeter-Wave Deployments

Dmitrii Solomitckii, Qian (Clara) Li, Tommaso Balercia, Claudio R. C. M. da Silva, Shilpa Talwar, Sergey Andreev, and Yevgeni Koucheryavy

Abstract—In this letter, we characterize the impact of diffuse scattering in dense urban deployments of millimeter-wave (mmWave) systems by using an advanced ray-launching (RL) simulation tool. Specifically, we first construct an RL-based methodology which is well-suited for the proposed analysis, and then investigate the received power distribution both with and without the contribution resultant from the diffuse scattering of rays for both line-of-sight (LOS) and non-LOS (NLOS) conditions. Simulation results are presented which show that, different from lower frequency bands, diffuse scattering makes a noticeable contribution to the total received power for NLOS links in the mmWave band. Therefore, when considering NLOS mmWave propagation in urban settings, it is critical to properly model and take into account specular attenuation due to surface roughness.

Index Terms—Millimeter-wave propagation, ray launching, propagation in urban areas.

I. INTRODUCTION

THE continued proliferation of wireless devices and services which often support very high throughput applications, calls for the development of new wireless technologies that together allow for the network capacity to scale to an unprecedented level. In order to obtain the bandwidth necessary to support higher data rate traffic, for example, it is anticipated that future generations of wireless communications systems, such as the fifth generation (5G) of cellular technology, will make use of frequencies in the mmWave band [1].

Because the wavelengths of mmWave signals are smaller than a centimeter, and thus smaller than most objects in the propagation environment, it is known that mmWave signal propagation is different from that of signals in bands used by current wireless systems. For instance, mmWave signals experience higher pathloss, atmospheric attenuation, and diffraction loss comparing to microwave systems [2], [3]. While the basic mechanisms of mmWave signals are well understood, there still remains a number of open questions regarding mmWave propagation in urban areas. Our goal in this letter is to shed light on one of such questions, namely, the impact of diffuse scattering to the total received power in LOS and NLOS mmWave links. To address this question, we propose an RL-based methodology that allows us to divide the total received

power of a mmWave signal into the individual contributions of each propagation mode, including diffuse scattering.

RL and ray tracing (RT) are popular and effective simulation tools for the analysis of radio propagation. When appropriate models are incorporated, these tools can be used to accurately simulate the propagation of a wavefront by taking into account various propagation modes. However, the incorporation of diffuse scattering in RT and RL tools is typically considered to be a “non-trivial task” [4] and even “impossible” by some authors [5] for a number of reasons. As a result, diffuse scattering is not accounted for in most RT and RL tools; and instead it is implicitly assumed that its contribution is negligibly small and thus ignored. A distinct example of such approach is the popular commercial simulator Wireless InSite which only models specular attenuation on a roughness [6, Chapter 9]. As discussed in what follows, we create our own simulator based on the techniques proposed in [7] and enhancing them significantly in terms of performance as well as by incorporating a diffuse scattering model.

The main contribution of this work is to characterize the joint impact of diffuse scattering and surface roughness induced attenuation for LOS and NLOS mmWave propagation in urban settings. The remaining sections of this letter are organized as follows. The physical models and methodology are introduced in Section II. In Section III, we outline our urban deployment with high user (receiver) density. Simulation results are offered in Section IV. Conclusions are drawn in Section V.

II. PROPOSED RL METHODOLOGY

Because we would like to simulate the received signal power distribution (i.e., make a coverage prediction) in a broadcast system comprising one transmitter (TX) and a large number of receivers (RXs), we chose to use RL as the signal propagation simulation tool. RL methods are preferred over RT simulation mechanisms because conventional RT tools exhibit exponential growth in computational complexity with an increase in the number of receivers [8].

As previously discussed, diffuse scattering is not accounted for in most RT and RL tools for a number of reasons, including computational complexity – which is particularly challenging for mmWave systems since most objects in the environment are larger than the wavelength – and certain limitations of “classical” diffuse scattering models. For instance, diffuse scattering models based on Rayleigh-Rice (RR) perturbation theory are only valid for a wide range of incident and scattered

D. Solomitckii, S. Andreev, and Y. Koucheryavy are with the Department of Electronics and Communication Engineering, Tampere University of Technology, Tampere, Finland (e-mail: {dmitrii.solomitckii, sergey.andreev}@tut.fi, yk@cs.tut.fi).

Q. Li, T. Balercia, C. R. C. M. da Silva, and S. Talwar are with Intel Corporation in Hillsboro, OR, USA, Aalborg, Denmark, and Santa Clara, CA, USA (e-mail: {clara.q.li, tommaso.balercia, claudio.da.silva, shilpa.talwar}@intel.com).

angles when surfaces with small roughness are considered [9]. Other models, such as those based on the Beckman-Kirchhoff approximation (BKA) [10], are only valid for a narrow angular range, which creates difficulty in modeling realistic environments.

In this letter, our RL tool incorporates the model proposed in [11] which was designed for implementation in RT tools and has been validated with experimental studies in urban deployments. The model used takes into account the roughness of a wall with Lambertian surface and with irregularities (such as decorations, pipes, balconies, and window frames, among others). Although the model in [11] was proposed for low operating frequencies, recent reports, such as [12], have demonstrated its applicability to mmWave bands.

The integration of an RL tool with the model proposed in [11] offers a methodology that can effectively simulate urban scenarios with thousands of antennas. The proposed methodology comprises two stages. In the first stage, we use an RL simulator which is based on the theory of geometric optics (GO) and the uniform theory of diffraction (UTD). It mimics wave propagation suffering from free-space loss, reflection, transmission, absorption, and diffraction. The output data after the first stage consists of the angle of arrival, time of arrival, phase, and magnitude of each multipath component (MPC) at each receiver. To reduce phase error associated with a finite RX antenna size [7], we additionally make a highly dense subsampling of rays from TX to RXs as soon as a path is established.

The second stage of our RL simulates the effects of diffuse scattering and begins by converting the walls of the buildings inside the desired urban scenario (to be described in Section III) into flat 3D rectangular surfaces. A preliminary tessellation of all surfaces into tiles (squares, pixels) is then performed, and each obtained tile is assumed to act as a potential source of reflected and diffuse-scattered rays. The size D of each tile is chosen such that the far-field rule is satisfied, that is,

$$r < 2D^2/\lambda, \quad (1)$$

where r is the distance between the tile and the RX, and λ is the wavelength (12.5 cm at 2.4 GHz and 1 cm at 28 GHz).

If the far-field rule is not satisfied after the preliminary tessellation, the surfaces are tessellated further into smaller tiles. From a geometric point of view, when a ray hits a rough surface, it produces a specular-reflected ray (Snell law) together with multiple diffused rays that originate at the ray-surface intersection point and travel in all directions. As a result, in our RL implementation of diffuse scattering, all tiles which have LOS to the TX are first “selected” [11] and then, among these tiles, those that show secondary or diffuse-scattered rays to the RX are connected in such a way that a diffuse scattering path is created.

When a wavefront meets an obstacle, its specular component loses power due to reflection, scattering, and/or penetration. This mechanism is modeled in terms of the effective (or,

generalized) reflection coefficient, which can be defined as

$$R_{eff} = R_{\perp} \left(1 - \frac{(1 - R_{\perp}^2) \exp(-2\alpha s) \exp(-2j\beta s) \exp(jkd \sin(\theta))}{1 - R_{\perp}^2 \exp(-2\alpha s) \exp(-2j\beta s) \exp(jkd \sin(\theta))} \right), \quad (2)$$

where the Fresnel coefficient R_{\perp} can be calculated for vertical polarization as

$$R_{\perp} = \frac{\cos(\theta) - \sqrt{\varepsilon - \sin^2(\theta)}}{\cos(\theta) + \sqrt{\varepsilon + \sin^2(\theta)}}. \quad (3)$$

Also in (2), α and β are the lossy medium propagation coefficients, s is the traveling distance inside the wall, d is the gap between two adjacent rays produced by internal reflection, and θ is the angle of incidence. The parameter ε is the dielectric permittivity of the wall, which is frequency-dependent. In the results given in Section IV, ε is taken to be equal to $5.3 - 0.3j$ and $5.3 - 0.5j$ for 28 and 2.4 GHz [13], respectively.

The power loss of specular component due to scattering in surface roughness is modeled by the coefficient in [11]

$$\rho = R_{\perp} \exp(-8\pi^2(\sigma/\lambda)^2 \cos^2(\theta)), \quad (4)$$

where $0 \leq \rho \leq 1$ and σ is the roughness coefficient (which is taken to be 1.2 mm in Section IV). Furthermore, the relative proportion of the diffused field compared to the incident field is modeled with a scattering coefficient defined as in [11]

$$S = E_s/E_i = \sqrt{(1 - \rho)}. \quad (5)$$

Depending on the deployment properties, the value of S varies between 0 and 1. In Section IV, we make S equal to 0.5, as discussed in the METIS 2020 Project [12]. In (5), the amplitude of the scattered field E_s is defined as in [11]

$$E_s^2 = K_0^2 S^2 \frac{dS \cos(\theta_i) \cos(\theta_s)}{\pi} \frac{1}{r_i^2 r_s^2}, \quad (6)$$

where $K_0 = \sqrt{60G_t P_t}$, dS is the tile size, θ_i and θ_s are the incident and scattered ray angles, respectively, r_i and r_s are the TX-to-tile distance and tile-to-RX distance, respectively, G_t is the antenna gain of the TX, and P_t is the transmit power.

In our RL methodology, we disregard objects that are smaller than the buildings as they make a less significant contribution to the diffuse scattered field at the RX. Further, since the contribution to the total received power coming from the wall penetration is negligible due to significant losses inside walls, this phenomenon is not considered in our evaluation either.

III. TARGET URBAN MMWAVE DEPLOYMENT

To study mmWave propagation in urban areas, we consider the Manhattan grid-like scenario shown in Fig. 1, in which a large number of RXs are located in and around a central square. The considered grid topology is common for various cities in the world and serves as a valid reference scenario for evaluating signal propagation in urban metropolitan areas. It is worth noting, as an example, that this topology has been used in the WINNER-II effort [14].

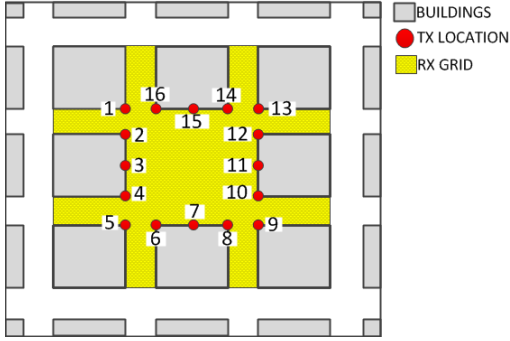


Fig. 1: Urban scenario model (top view)

Concentrating on the first-order evaluation, our deployment does not include smaller objects, such as lampposts, cars, and people, since their smaller surfaces do not produce a significant impact on the diffuse scattering picture. Therefore, it is assumed that buildings are the only source of ray blockage in our model (see Fig. 1). Further, the RXs are carefully positioned in the area of interest (outside of the buildings) forming a square grid, with an accurate step of 5 meters, such that they cover the central square and the “streets” that lead to the square. The algorithm placing the RXs adjusts the receiver grid positions to make them symmetric within our scenario. With the proposed RX distribution, the total number of receivers obtained is approximately equal to 3,500. Specific parameter values used in our simulations are given in Table I.

TABLE I: Simulation scenario properties

Parameter	Value
Building size	120 x 120 x 150 m
Building material	Concrete (50 m)
Receiver grid size	460 x 460 m
Receiver grid height	1.5 m
Transmitter height	5 m

Since it is assumed that the RXs are located in and around the central square, we also impose that the TX (representing a base station or an access point) might be installed on the walls of the buildings in either of 16 positions that surround the central square (represented by red dots in Fig. 1). In our simulations, the TX and RXs are represented as isotropic antennas operating with sinusoidal waves at either 28 or 2.4 GHz. The radiated power of the TX is 25 dBm. Other transmission parameters are selected such that the near-field radiation effects can be ignored. Additionally, it is assumed that the antennas of the TX and RXs are vertically polarized (that is, there is no polarization mismatch).

Because we assume that the TX and RXs are ideal isotropic antennas, radio signal is emitted in all the directions across our deployment uniformly. As a result, neither antenna needs to be re-oriented for different RX positions. Further, each of the transmitted rays interacts with the objects in the physical environment (buildings) through phenomena, such as reflection and scattering, for example. The signals received by a given RX are thus formed by the sum of different rays, which propagated through different paths and thus have different power levels. In the following section, we investigate the

fraction of the total received power that corresponds to rays that experienced specular attenuation due to surface roughness in LOS and NLOS scenarios.

IV. SIMULATION RESULTS

Before considering the contribution of diffuse scattering to the received signal power of LOS and NLOS links, we evaluate the impact of the TX’s position on the received signal power statistics. To this end, the cumulative distribution function (CDF) of the received signal power in all the considered RX positions calculated via simulation for the 16 TX positions is shown in Fig. 2. As seen, the TX locations produce three symmetric groups of CDF profiles: 1,5,9,13 – first group; 2,4,6,8,10,12,14,16 – second group; and 3,7,11,15 – third group. All having the same shape of their curves, the CDFs reside within the maximum variance level of 4 dB. Based on that, we can conclude that the actual TX position does not impact the power distribution significantly.

In what follows, we take TX1 as our reference transmitter.

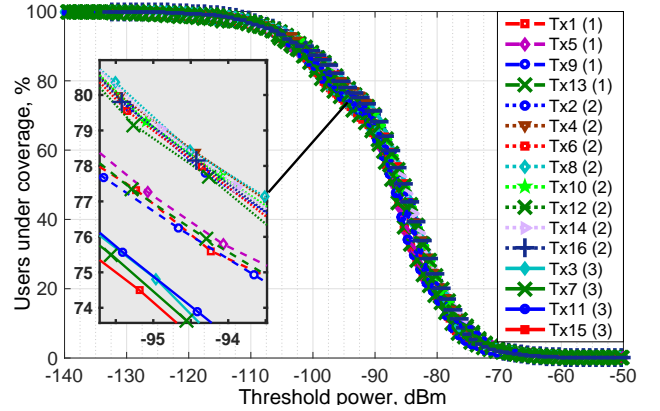


Fig. 2: Coverage CDF for each transmitter in our deployment

As can be seen in Fig. 1, some RXs in the considered simulation scenario can only be reached with higher-order specular rays which do not carry significant power. At the same time, according to the non-Snell propagation law, diffuse scattering has the potential to deliver a certain additional power to such NLOS RXs. To analyze this effect, we divide the RXs into two different groups based on whether the RX has LOS to the TX or not. To determine whether an RX has LOS to the TX, our simulation tool connects the TX and RX with a straight line and checks if it intersects any walls.

Simulation results obtained with the proposed RL methodology are given in Figs. 3 and 4 for 2.4 and 28 GHz, respectively, for the two groups of RXs (namely, LOS and NLOS). By comparing both figures, it can be seen that diffuse scattering contributes to the NLOS received power approximately 2 and 8 dB for 2.4 and 28 GHz, respectively, confirming the fact that rough surface scattering effects are enhanced in the mmWave band.¹ Also visible in both figures is the fact that the impact of

¹It should be noted that for the considered simulation scenario, the total received power level increase of 8 dB due to diffuse scattering corresponds to an increase of approximately 20% in the number of NLOS served users.

diffuse scattering to the received signal power of LOS RXs is negligible, as expected, and fluctuates within the RL accuracy.

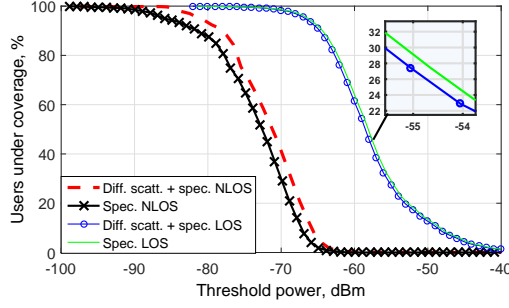


Fig. 3: Coverage CDF at 2.4 GHz for LOS/NLOS receivers

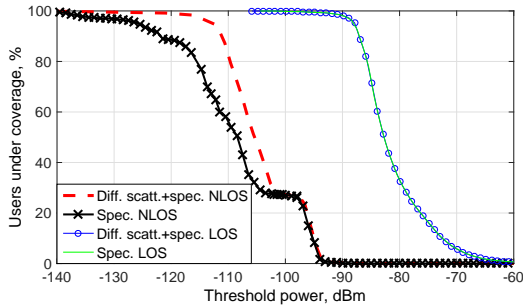


Fig. 4: Coverage CDF at 28 GHz for LOS/NLOS receivers

A closer look at Fig. 4 reveals that, for NLOS links, we have an uncompensated “plateau” in the CDF when non-specular rays are not taken into account. This plateau is *partially* “compensated” when low-order diffuse scattering is considered. The “uncompensated” part of the plateau would probably be reduced if higher-order diffuse scattering rays were taken into account by the simulation tool. While the methodology presented in Section II could be extended to include high-order diffuse scattering, the required computation time can become prohibitive depending on the scenario.

Finally, we note that this work does not focus on MIMO antennas which are the topic of a separate research. However, our preliminary estimation indicates that if each of the isotropic RXs becomes a directional antenna having only the main lobe with half-power beam width (HPBW) of 42 deg and the normalized gain oriented along the most significant arriving ray, we see a reduction in the diffuse scattering contribution at 28 GHz down to 6.6 dB due to antenna selectivity effects.

V. CONCLUSIONS

We showed by using an RL simulation tool that diffuse scattering does make a noticeable contribution to the received signal power of NLOS links in mmWave bands. The contribution of diffuse scattering in mmWave frequencies (28 GHz) was confirmed to be higher than that in low frequencies (2.4 GHz); in the urban area model used in our simulations, the relative difference between the contributions in both bands was of approximately 6 dB. As an example of the impact of this result, we have that propagation simulation tools which

do not model diffuse scattering can underestimate the number of users served by a given TX in urban areas. Also, the impact of diffuse scattering to the received power in LOS links was shown to be negligible in both 2.4 and 28 GHz, as expected, which is due to the significant difference in power between the LOS and reflected/scattered rays in this case.

Our additional results demonstrated that there is no significant difference in Tx locations in terms of power distribution and grouping of CDFs due to symmetry of the environment. The presented simulation findings also showed a plateau in the received power CDF for NLOS receivers in the 28 GHz band, which resulted from the uncompensated attenuation of specular rays on the roughness of the building walls. The plateau was shown to partially disappear when the contribution of diffuse scattering was accounted for. The remaining part of the plateau would probably reduce further if high-order diffuse scattering was considered by the simulation tool. In our future work, we plan to extend the developed RL simulation tool to allow for the analysis of MIMO systems [15].

ACKNOWLEDGMENT

This work is supported by Intel Corporation and the project TT5G: Transmission Technologies for 5G.

REFERENCES

- [1] E. Dahlman, G. Mildh, S. Parkvall, J. Peisa, J. Sachs, Y. Selén, and J. Sköld, “5G wireless access: Requirements and realization,” *IEEE Commun. Mag.*, vol. 52, pp. 42–47, Dec. 2014.
- [2] Y. Niu, Y. Li, D. Jin, L. Su, and A. V. Vasilakos, “A survey of millimeter wave communications (mmWave) for 5G: Opportunities and challenges,” *Wireless Netw.*, vol. 2, pp. 2657–2676, Nov. 2015.
- [3] T. S. Rappaport, G. R. MacCartney Jr., M. K. Samimi, and S. Sun, “Wideband millimeter-wave propagation measurements and channel models for future wireless communication system design,” *IEEE Trans. Commun.*, vol. 63, pp. 3029–3056, Sept. 2015.
- [4] A. F. Molisch, *Wireless Communications*. John Wiley & Sons, 2 ed., 2011.
- [5] R. Aquino-Santos, *Wireless Technologies in Vehicular Ad Hoc Networks: Present and Future Challenges*. IGI Global, 2012.
- [6] Remcom Inc., *Wireless InSite Reference Manual*, Feb. 2014.
- [7] G. Durgin, N. Patwari, and T. S. Rappaport, “An advanced 3D ray launching method for wireless propagation prediction,” in *Proc. IEEE Veh. Technol. Conf.*, Phoenix, AZ, 1997, pp. 785–789.
- [8] N. Bessis, *Development of Distributed Systems from Design to Application and Maintenance*. IGI Global, 1 ed., Dec. 2012.
- [9] S. O. Rice, “Reflection of electromagnetic waves from slightly rough surfaces,” *Commun. Pure Appl. Math.*, vol. 4, pp. 351–378, Aug. 1951.
- [10] P. Beckmann and A. Spizzichino, *The Scattering of Electromagnetic Waves from Rough Surfaces*. Pergamon Press, 1963.
- [11] V. Degli-Esposti, “A diffuse scattering model for urban propagation prediction,” *IEEE Trans. Antennas Propag.*, vol. 49, pp. 1111–1113, Jul. 2001.
- [12] V. Nurmela, A. Karttunen, A. Roivainen, L. Raschkowski, T. Imai, J. Jarvelainen, J. Medbo, J. Vihriala, J. Meinila, K. Haneda, V. Hovinen, J. Ylitalo, N. Omaki, K. Kusume, P. Kyosti, T. Jamsa, A. Hekkala, R. Weiler, and M. Peter, “METIS channel models,” Tech. Rep. ICT-317669-METIS/D1.4, METIS, Feb. 2015.
- [13] “Propagation data and prediction methods for the planning of indoor radio communication systems and radio local area networks in the frequency range 900MHz to 100GHz,” Feb. 2012.
- [14] M. Abaai, G. Auer, Y. Cho, I. Cosovic, M. Döttling, K. George, L. Hamm, P. Jesus, S. Kyriazakos, V. Jungnickel, A. Mihovska, M. Olsson, A. Osseiran, K. Pantelis, D. Schulz, C. Silva, M. Sternad, T. Svensson, Y. Wan, C. Wijting, and Y. Zhu, “Test scenarios and calibration cases issue 2,” Tech. Rep. D6.13.7 v1.00, WINNERII, Dec. 2006.
- [15] M. Park and H. K. Pan, “A spatial diversity technique for IEEE 802.11ad WLAN in 60 GHz band,” *IEEE Commun. Lett.*, vol. 16, pp. 1260–1262, Aug. 2012.

PUBLICATION

II

Characterization of radio links at 60 GHz using simple geometrical and highly accurate 3-D models

V. Semkin, D. Solomitckii, R. Naderpour, S. Andreev, Y. Koucheryavy and
A. V. Räsänen

IEEE Transactions on Vehicular Technology 66.6 (2016), 4647–4656

DOI: 10.1109/TVT.2016.2617919

Publication reprinted with the permission of the copyright holders

Characterization of Radio Links at 60 GHz Using Simple Geometrical and Highly Accurate 3D Models

V. Semkin, D. Solomitckii, R. Naderpour, S. Andreev, Y. Koucheryavy, and A. V. Räsänen

Abstract—In order to effectively deploy high data rate millimeter-wave communication systems in urban environments, accurate information about the radio wave propagation channel is essential. Radio wave propagation in urban scenarios strongly depends on the topography of the immediate surroundings. A measurement campaign has been carried out to evaluate the impact of propagation effects on the radio channel at the rooftop level of buildings. In the simulation part of the paper, we present two 3D models produced with different techniques: firstly, a simple geometrical model and secondly, a highly accurate close-range photogrammetry model; the latter replicates the detailed building geometry. To construct a highly accurate 3D model, images obtained by an unmanned aerial vehicle were utilized together with the photogrammetry technique. In this paper, we provide a thorough comparison between the measured and the simulated power delay profiles by conducting shooting-and-bouncing ray-based simulations for the rooftop scenario using two 3D models of different accuracy. The results show that the use of the close-range photogrammetry model can provide better propagation prediction at millimeter-wave frequencies.

Index Terms—Radio wave propagation, photogrammetry, millimeter-wave, ray-based simulations, unmanned aerial vehicle.

I. INTRODUCTION

OVER the last few years the demand for high data rate mobile communication has steadily increased, consequently, high capacity radio systems with better coverage, higher transmission quality, and more efficient use of the radio spectrum are required. To address these demands, mobile operators have not only to select an appropriate wireless technology for a particular case, but also deploy it effectively based on the specifics of the immediate environment. Wireless networks operating at millimeter-wave (mm-wave) frequencies represent one promising solution to support the multi Gbit/s data rate requirements. In particular, unlicensed frequency bands at mm-wave frequencies can be

attractive for this purpose. Today, 57-66 GHz frequencies are used primarily for indoor communications [1-2]. However, the emergence of new standards, such as IEEE 802.11ay, can dramatically alter this situation. The new technology under development aims to utilize mm-wave frequencies and, possibly, the 60 GHz band will be used also in outdoor scenarios.

Several aspects of mm-wave radio wave propagation in different environments and for various applications have previously been studied, e.g., in [3-5]. For instance, [3] presents physical and analytical radio wave propagation models for multiple-input multiple-output (MIMO) systems and evaluates their performance. In [4], the authors investigate three large-scale path loss models for 5G wireless systems in terms of their prediction accuracy, sensitivity, and parameter stability. The work in [5] presents measurement-based values for the parameters, such as the line-of-sight (LOS) probability, path loss, and shadow fading at frequencies 2, 10, 18, and 28 GHz.

In contrast, the focus of the present study is on the environmental modelling accuracy of radio wave propagation. It is well-known that at mm-wave frequencies, physically small objects begin to impact radio wave propagation due to their electrically large sizes, which substantiates the need for more detailed 3D models of the environment [6]. While works such as [6-8] have attempted to use a Light Identification Detection and Ranging (LIDAR) -based 3D point cloud model of the environment for a better prediction of radio wave propagation at mm-wave frequencies, in this work we use an Unmanned Aerial Vehicle (UAV) -based photogrammetry model to investigate the prediction accuracy improvements achieved over that by a simpler 3D geometrical model.

Shorter wavelengths across mm-wave bands make the objects, which are electrically small at lower frequencies, become a considerable source of scattering, producing additional multipath components between the transmitter and the receiver. In practice, such paths may improve the channel performance and might be exploited by directional antennas. However, prior to hardware design or equipment installation, careful preliminary evaluation has to be carried out. One attractive approach to such pre-estimation is simulation by using deterministic ray-based methods that require an accurate 3D CAD-model of the environment together with specific antenna positions. Ray-tracing (RT) as well as shooting-and-

Manuscript received April 21, revised August 15, accepted September 16, 2016.

V. Semkin would like to thank Nokia Foundation, Walter Ahlström Foundation and Aalto ELEC Doctoral School for support. This work was supported in part by Academy of Finland through the projects Transmission Technologies for 5G (TT5G) and DYNAMITE.

V. Semkin, R. Naderpour, and A. V. Räsänen are with Aalto University, Espoo, Finland (e-mail: vasilii.semkin@aalto.fi).

D. Solomitckii, S. Andreev, and Y. Koucheryavy are with Tampere University of Technology, Finland.

bouncing ray (SBR) belong to the group of models, which are very sensitive to the detailed composition of the scenario.

Based on the high-frequency theory [9], ray-object interaction is only possible, when the object is much larger than the wavelength. Hence, when accurate RT/SBR simulations are needed at mm-wave frequencies, it is crucial to identify an inexpensive, fast, and precise method of capturing a specific 3D environment. We selected the SBR method because it works more efficiently (compared to image-based RT methods) in complicated propagation scenarios, where significantly detailed elaboration is required [10].

The models conventionally used in radio wave propagation simulations are composed of simple geometrical figures [11] and only capture the major factors in the geometry of the environment. One of the potential methods that can improve the quality of coverage prediction is photogrammetry, which is a technique for reconstructing the 3D models of different objects from two or more photographs [12]. To the best of our knowledge, there are currently no studies related to the application of highly accurate photogrammetry models obtained by UAVs for radio-wave propagation prediction. The highly accurate 3D models may include all the smaller details of the environment and thus significantly improve the results of RT/SBR simulations. Such 3D models can also be reconstructed using the LIDAR technology [8, 13-14].

We note that photogrammetry can achieve the levels of accuracy similar to laser scanning [15-16] and it can be more cost-effective compared to the LIDAR technology. Furthermore, in some scenarios it is not easy to use the LIDAR if the information about rooftops of a group of buildings is needed. The utilization of (ultra) small UAVs equipped with cameras together with the photogrammetry software has the potential to solve this challenge. There are published works where the authors combine the LIDAR technology and the UAV in order to construct the 3D models of the environment, see e.g., [17]. Such an approach is more expensive and can pose a threat if the measurements are taken in densely populated areas, since the weight of the UAV with the LIDAR is high. Another issue is that using the LIDAR on the UAVs requires more time to acquire data since the vertical field of view (FOV) is usually limited on the LIDAR devices.

The major goal of our present work is to demonstrate the difference in the output results by comparing the measured channel impulse response with the one produced by the SBR simulations based on I) a low-detail block model and II) an accurate model constructed with 3D photogrammetry. Another purpose is to highlight the applicability of the photogrammetry approach, which produces highly-accurate 3D-models of the environment for the RT/SBR simulations. Even though 28 GHz is an attractive candidate band for future 5G cellular applications [18], the 60 GHz frequency range is considered here, as it more clearly articulates the difference in simulations when using the two models with different accuracy. The surrounding objects can impact the multipath propagation at 60 GHz more than at lower microwave frequencies.

The results of our work might be useful for design engineers and researchers involved in analytical

characterization of wireless channels operating at mm-wave frequencies. We also demonstrate the applicability of photogrammetry reconstruction methods for propagation channel modeling.

The structure of this paper is the following: Section II describes the methodology used in this work. Section III provides a detailed description of the utilized channel sounding equipment, as well as the measurement environment and the floor map. Section IV explains how the simple geometrical and the close-range photogrammetry models are created. Section V presents the comparison between the simulation and measurement results. Section VI offers a discussion and concludes the obtained results.

II. METHODOLOGY

A. Measurements

In the framework of this paper, we consider a single-input single-output (SISO) deployment, where an electromagnetic wave propagates from the transmitter to the receiver. A biconical omni-directional antenna has been used at the transmit side and an H-plane sectoral horn antenna, which was rotated along the azimuth plane, was utilized at the receive side. The transmit antenna radiates the electromagnetic field in certain directions, which are defined by the main lobe of the antenna pattern. The electromagnetic wave propagates within the medium and interacts with objects in it. This interaction causes the antenna to receive portions of the electromagnetic wave energy delayed in time. This effect, known as discrete multipath components (MPCs), can be described using the channel impulse response (CIR) in the time domain and the transfer function in the frequency domain. Both domains provide a full description of the wireless transmission between the transmit and receive antennas. The CIR can be written as [19]:

$$h(\tau, \varphi) = \sum_{l=1}^N a_l \delta(\tau - \tau_l) \delta(\varphi - \varphi_l), \quad (1)$$

where a_l , τ , and φ are the complex amplitude, the excess delay, and the angle of arrival (AoA), respectively. This equation demonstrates that N different paths propagate within the same medium from a single transmitter to the receiver having an infinite bandwidth. At the receiver side, we observe a train of delta-functions with the amplitude a_l , arriving with the delay τ and the angle φ (we use a directional antenna at the receiver).

Since the MPCs characterize the dispersion of the transmitted signal, the power delay profile (PDP) can be taken as a measure of this dispersion. It can be calculated as the averaged value of the CIR:

$$p(\tau, \varphi) = |h(\tau, \varphi)|^2, \quad (2)$$

where $p(\tau, \varphi)$ is the instantaneous PDP at the azimuth angle φ . The delta-functions in Eq. (1) correspond to an ideal case with infinitely large bandwidth, which is not achievable in reality as the channel and hardware components are bandwidth limited. Therefore, a practical channel sounding system produces a convolution between the real shape pulse and the ideal channel impulse response:

$$p(\tau, \varphi) = |h(\tau, \varphi) \times h_{\text{ChannelSonder}}(\tau)|^2, \quad (3)$$

where $h_{\text{ChannelSonder}}(\tau)$ is the impulse response of the channel sounder [20].

To bypass some of the negative effects of fading, we apply averaging on the multiple PDPs produced at each step of rotation of the receive antenna. This averaging leads to smoothening the significant spikes and valleys. The averaged power delay profile (APDP) can be written as:

$$APDP(\tau) = \frac{1}{M} \sum_{i=1}^M p(\tau, \varphi), \quad (4)$$

where M denotes the number of azimuth angle steps covering the full 360-degree range. In our measurements, $M = 73$. For the purposes of channel properties estimation, we employ the above methodology in order to describe the measurement as well as simulation results.

B. Simulations

To obtain the APDP at the output of our modeling, a deterministic approach has been selected since it offers adequate accuracy in outdoor scenarios [21]. In this paper, we use the SBR method, which is a component of the commercially available Wireless InSite tool by Remcom. In the SBR method, a transmitter is represented as a source of tubes that may be traced uniformly within the scenario. When the ray hits an object, it is split into a transmitted and a reflected component. The relationship between the angles of incidence and refraction is driven by Snell's law. The diffraction occurs according to Keller's law and can be calculated on the edges and vertices of the objects. When the receive antenna's radiation pattern collides with some of the ray-tubes, it acquires a portion of the electric field, which is associated with the ray.

The physical part of the SBR method is based on the geometrical optics (GO) principles for the reflection and the transmission effects as well as on the uniform theory of diffraction (UTD) [9, 22, 23]. Free space loss propagation can be described by solving the Maxwell-Helmholtz equation:

$$E(r, \theta, \varphi) = E_0(\theta, \varphi) \frac{e^{-j\beta r}}{r}. \quad (5)$$

In order to calculate the electric field reflected from a surface, the incident electric field is expanded into a parallel and a perpendicular component to the plane of incidence:

$$\begin{bmatrix} E_{\parallel}^r \\ E_{\perp}^r \end{bmatrix} = \begin{bmatrix} R_{\parallel} & 0 \\ 0 & R_{\perp} \end{bmatrix} \begin{bmatrix} E_{\parallel}^i \\ E_{\perp}^i \end{bmatrix}, \quad (6)$$

where R_{\parallel} and R_{\perp} are the Fresnel reflection coefficients for the parallel and perpendicular component, which are described as:

$$R_{\perp} = \frac{\cos(\theta_i) - \sqrt{\varepsilon - \sin^2(\theta_i)}}{\cos(\theta_i) + \sqrt{\varepsilon - \sin^2(\theta_i)}}, \quad (7)$$

$$R_{\parallel} = \frac{\varepsilon \cos(\theta_i) - \sqrt{\varepsilon - \sin^2(\theta_i)}}{\varepsilon \cos(\theta_i) + \sqrt{\varepsilon - \sin^2(\theta_i)}}. \quad (8)$$

In (7) and (8), θ_i is the angle of incidence and ε is the dielectric permittivity of the material of a reflective surface. The diffracted electric field can be written as:

$$\begin{bmatrix} E_{\beta}^d \\ E_{\varphi}^d \end{bmatrix} = \begin{bmatrix} D_{ss} & D_{sh} \\ D_{hs} & D_{hh} \end{bmatrix} \begin{bmatrix} E_{\beta}^i \\ E_{\varphi}^i \end{bmatrix} \sqrt{\frac{r_{td} r_{dr}}{r_{td} + r_{dr}}} \frac{e^{-j\beta r_{dr}}}{r_{dr}}, \quad (9)$$

TABLE I. MODELING INPUT PARAMETERS FOR 60 GHz SIMULATIONS

Parameter	Value
PROPAGATION PARAMETERS	
Propagation model	Full 3D (SBR)
Ray spacing	0.005°
Number of reflections	5
Number of diffractions	1
Number of transmissions	0
MATERIAL PROPERTIES	
Wall material	Brick
Dielectric permittivity	2.55-j0.43
Conductivity	1.43 S/m
ANTENNA PARAMETERS	
Tx antenna	Omnidirectional, 2 dBi gain
Rx antenna	Horn, 19 dBi gain
Transmit power	15 dBm

where $D_{ss,sh,hs,hh}$ are the dyadic diffraction coefficients, r_{td} is the distance between the transmitter (Tx) and the diffraction point, r_{dr} is the distance between the receiver (Rx) and the diffraction point, and β is the wave number.

The steps of the simulation procedure are similar to the measurement post-processing technique. For all receiver pointing directions, a single PDP is calculated which is then converted to the APDP. It has to be noted that Wireless InSite offers a possibility to set the required antenna type and adjust its properties for an accurate simulation. The correctness of the antenna properties was verified using the technical specification provided by the antenna manufacturer. The parameters used in the SBR simulations are summarized in Table I. The number of reflections is set to 5 and the number of diffractions to 1. Transmission is not taken into account since at mm-wave frequencies only reflection and diffraction are of significance. The spacing between the rays at the Tx side is set at 0.005°. The wall material is selected to be brick and the electric properties are set according to [24].

III. MEASUREMENT SCENARIO AND EQUIPMENT

The environment where the measurements were conducted is a 3-floor building with a flat roof covered by roofing felt. The sounding setup used for the measurements presented in this paper has been developed at Aalto University's Department of Radio Science and Engineering. This VNA-based system allows for phase-synchronized measurements of

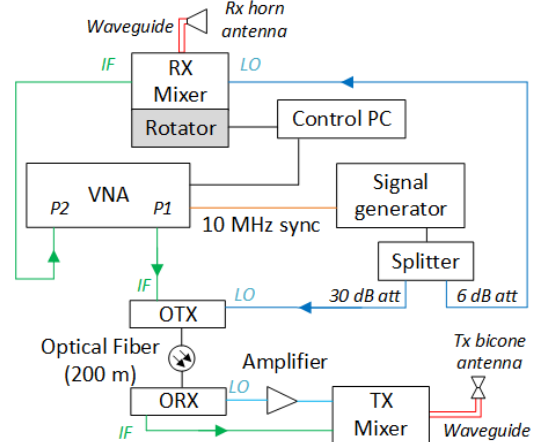


Fig. 1. The 60 GHz sounding setup.

TABLE II. PARAMETERS OF THE MEASUREMENT SYSTEM

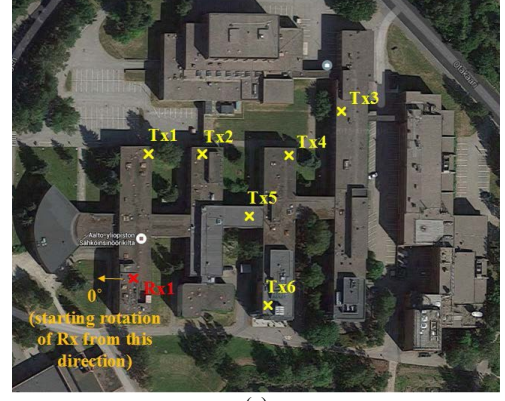
Description	60 GHz setup (measurements)
IF signal	1-5 GHz
LO signal	14.5 GHz
RF signal	59-63 GHz
Center frequency	61 GHz
LO power	+24.5 dBm
VNA power	-15 dBm
Number of sweep points	10001
Tx antenna	Bicone, 2 dBi gain
Rx antenna	Horn, 19 dBi gain
HPBW of the Rx antenna	40° in elevation plane, 10° in azimuth plane
Antenna interface	Waveguide
Back to back calibration	20 dB attenuator

scattering parameters with the radio channels being the device under test [25]. The channel measurements at 60 GHz are conducted using frequency up- and down-converters. The converters are harmonic mixers with internal frequency doublers. To increase the achievable link distance, 1) the conventional coaxial-cable link from the VNA and the signal generator to the Tx antenna is replaced by an optical fiber link and 2) a high-gain directional horn antenna is used at the Rx side to increase the dynamic range of the measurements. A directional horn antenna with a peak gain of 19 dBi and an omni-directional biconic antenna with a 2 dBi gain are used as the receive and transmit antenna, respectively. It is important to note that the 30- and 6-dB attenuators are necessary to prevent possible damage to the optical transmitter and the down-converter, respectively, as a result of high input power. The 10-MHz synchronization cable allows for phase synchronization between the VNA and the signal generator.

The directional measurements are conducted by scanning the Rx antenna over the azimuth angle range of 0 to 360 degrees with steps of 5° by recording S_{21} . In the 60-GHz setup, at each azimuth angle step, the IF signal from port 1 of the VNA and the LO signal from the signal generator are sent to the optical transmitter where these electrical signals are converted to optical. Then, the converted IF and LO signals are transferred to the optical receiver at the Tx side through a 200-meter long optical fiber cable. The optical receiver converts the IF and LO back to electrical signals. The IF is carried directly to the up-converter while the LO is amplified using a 30-dB amplifier. This signal amplification is necessary to meet the minimum RF power requirements of the mixer.

The mixer up-converts the IF and LO to produce the sinusoidal RF signal in the frequency range of 59 to 63 GHz. This RF signal is then transmitted by the omni-directional biconic antenna; it propagates within the channel and is received by the horn antenna. The down-converter at the Rx side uses the LO provided to it via a coaxial cable link from the signal generator to down-convert the received RF signal and retrieve the IF component. The IF is then transferred to port 2 of the VNA using a coaxial cable connection.

The Diamond Antenna Measurement System (DAMS) software, which controls the antenna positioner, reads the measured S_{21} from the VNA at each azimuth angle step.



(a)



(b)

Fig. 2. Measurement scenario: (a) an image of the measurement location from Google Maps with the Rx and Tx antenna positions on the rooftop of Otakaari 5, Espoo, Finland; (b) a photograph of the studied environment.

Eventually, the DAMS software produces a 73x10001 recorded CIR matrix as its output. The number of azimuth angle steps is 73 and the number of frequency points over which the CIR is measured is 10001. A back-to-back calibration was performed prior to the measurements in order to cancel out the effects of the sounding equipment. The block diagram of our 60 GHz measurement setup is presented in Fig. 1 and the parameters of the system are summarized in Table II. The measurements were conducted in the form of the backhaul link scenario on the rooftop of Aalto University's School of Electrical Engineering building. To this end, Fig. 2(a) shows an aerial image from Google Maps of the measurement location as well as the Tx and Rx locations. Further, Fig. 2(b) illustrates a 3D image of the rooftop where there are several metallic and non-metallic objects. These objects are electrically large compared to the wavelengths at 60 GHz frequencies and together with the brick walls of the building, the metallic window frames, and the antenna masts become the potential sources of electromagnetic wave scattering and/or blockage.

The Rx antenna is positioned at the second level of the rooftop, as indicated in Fig. 2(b). In total, 6 LOS Tx locations with different distances were planned for the purpose of conducting measurements.

IV. 3D MODELS OF THE ENVIRONMENT

Two 3D models of the building in question have been created and are presented in Fig. 3: 1) a simple geometrical

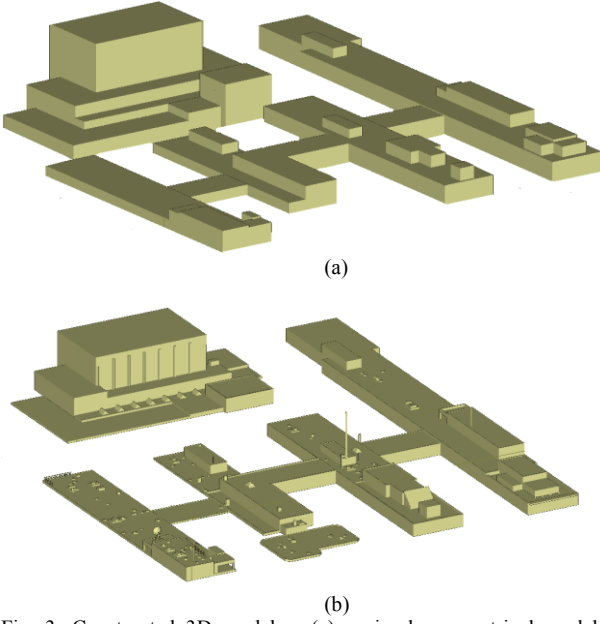


Fig. 3. Constructed 3D models: (a) a simple geometrical model of the environment; (b) a close-range photogrammetry model. Foliage is not shown, but is included in the simulations.

model consisting of cubes and; 2) a highly accurate close-range photogrammetry model.

A. Simple geometrical model

A model of the target building has been created in CAD software PTC Creo by using the outline size adopted from Google Maps and later verified by measuring the actual dimensions of the building. This simple geometrical model is presented in Fig. 3(a). Such an approach gives us a possibility to reconstruct larger parts, including the blocks of the building, but no information is included on the smaller objects on the roof top. To achieve adequate correlation between the simplified and the accurate model – as well as produce a benchmark for comparing the final results – we assume that the height of the simplified building blocks is known. At the stage of CAD-model construction, foliage has not been included since it is considered by the Wireless InSite tool later on.

The traditional approach, i.e., to use the existing built-in function of the Wireless InSite software for recreating the 3D model of the environment automatically via a satellite map translation was not followed. This is because in many cases this automated solution may compromise the surface description accuracy. Hence, the 3D model was built manually to reproduce all of the important geometrical details of the building as accurately as possible, creating a relatively precise environment in terms of bulky details.

B. Close-range photogrammetry model

A highly accurate 3D model is reconstructed from the images taken by the quadcopter DJI Phantom 3 Advanced shown in Fig. 4. The Phantom 3 device has a Sony-made 12-megapixel camera with a 1/2.3-inch CMOS sensor and f2.8 20 mm lens, which gives a 94° FOV. One of the requirements for constructing the highly accurate model is that the acquired



Fig. 4. The 3D point cloud obtained by close-range photogrammetry with the locations of the photographs and the look of the quadcopter Phantom 3.

images should have large enough overlapping areas between each other. The wide FOV of the camera on the Phantom 3 allows for capturing fewer images at the same height compared to many other cameras. The photographs are accompanied by their corresponding GPS information.

First, high contrast ground control points (GCPs) with known GPS coordinates are placed around the building as well as on its rooftop, so that they are visible on the photos taken by the copter. These GCPs become the reference points necessary to improve the accuracy of the model, since there could be errors in the GPS coordinates of the photographs. Then, the nadir and oblique images are obtained. A pre-loaded program on a remote computer is used to control the flight path needed to obtain 33 nadir photographs. Next, the drone is controlled manually to obtain 244 oblique photographs. Several flights at different heights and with various camera angles are performed. The oblique photographs are taken while flying the copter around the building.

In order to reconstruct the mast, which is located on the rooftop in the middle of the building, 69 images were taken while flying around the mast at different heights. In total, 346 images are obtained covering an area of 15600 m². Later, using Pix4D mapper software, 3 different point clouds are created, including two point clouds based on the nadir and oblique photographs of the building, respectively, and one point cloud based on oblique photographs of the mast.

Each photograph has a geotag provided by the GPS device onboard the quadcopter, so that they can be placed according to the coordinates. The software finds similar characteristic points based on the contrast of each photo. When two similar points are found to be the same, they produce matched key points. A group of matched key points forms a single point in the 3D coordinate system. After that, several similar key points in each point cloud are highlighted, so that the three point clouds can be merged into a single one to obtain a full 3D model of the environment. Finally, the densification process of the merged point cloud is performed with the end result displayed in Fig. 4.

The ray launching software requires a mesh model at its input. In the photogrammetry software, it is possible to measure the dimensions of the objects, and based on these measurements the 3D mesh model is created in CAD software

to then be exported into the Remcom Wireless InSite (see Fig. 3(b)). The accuracy of the 3D model is verified by comparing the real dimensions of the objects on the rooftop (measured with a tape-line) to the dimensions measured on the point cloud in the photogrammetry software. The comparison is based on the measurements of 30 objects. The average error is 5.17 cm with the standard deviation of 5.8 cm.

In the highly accurate model, the rooftop is assumed to be the “ground” level. All objects below it are disregarded as they are completely shadowed by the roof and thus do not affect the simulation results.

The foliage is represented as cubes in the simulations with both the simple geometrical and close-range photogrammetry models. Even though it is possible to create the 3D models of trees, simple foliage models are utilized to reduce the number of faces describing the complex geometry of trees and foliage. If foliage is reconstructed with higher accuracy, it may drastically increase the number of faces leading to prohibitive simulation times.

V. SIMULATION AND MEASUREMENT RESULTS

The computational speed related to the simple geometrical and the highly accurate model is summarized in Table III. The time required to obtain the simulation results for the highly accurate model constitutes nearly 3 times that of the simple geometrical model. This is because of a larger number of faces in the highly accurate model. However, the highly accurate model can provide the PDP closer to the measured values, as will be shown later in this section.

Based on the ray-based modeling principles, the MPCs propagate between the Tx and the Rx as well as interact with the surrounding objects. To this end, Fig. 5 illustrates example rays launched from the transmitter at Tx 1 and received at the receiver Rx for a) the simple geometrical model and b) the photogrammetry-based model of the environment. Clearly, in the simulation based on the simple geometrical model, with the exception of the LOS path, all propagating rays are either reflections from the walls or ground reflections. However, it is visible that once the smaller objects are introduced to the model (photogrammetry model in Fig. 5(b)), they act as the effective sources of scattering with multiple rays reaching the receiver after bouncing from such objects.

Further, Fig. 6 presents the measurement results (thick gray plot) of the APDP, as well as the simulation data, by using the close-range photogrammetry model and the simple geometrical model of the environment, respectively. Based on this plot, the MPCs arriving at the Rx can be distinguished in the time domain. There are three possible ways of receiving the signal: LOS, reflection, and diffraction. In our simulations, they contribute to the received signal power in the following manner: LOS is 79%, single reflection is 19%, and diffraction

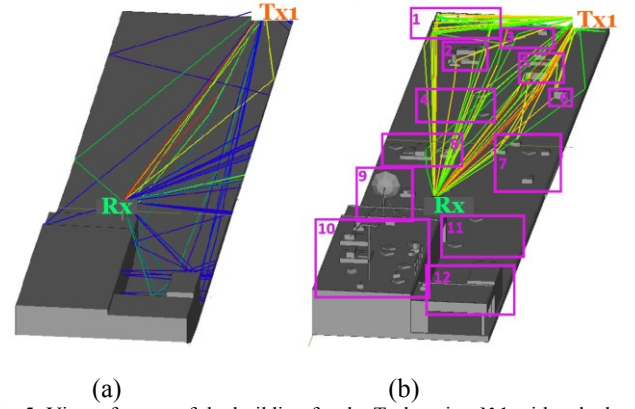


Fig. 5. View of a part of the building for the Tx location №1 with calculated rays, (a) simple geometrical model, (b) close-range photogrammetry model. The color of each ray corresponds to power carried by it. In this color map, dark blue and dark red represent the lowest and highest values, respectively.

is 1.2%. As we can see, diffraction is not the dominant physical phenomenon at mm-wave frequencies as it was assumed in [26-27], because the objects that produce the diffracted paths may be omitted in most of the cases where the LOS is present. Due to significant attenuation in mm-wave bands, the reflected paths become the dominant components for shorter links.

The convergence between the results based on the simple geometrical model and measurements is lower when compared to the simulation results for the photogrammetry model. For example, for the first Tx location, the corresponding APDP shows that within the initial 200 nanoseconds the Rx obtains a significantly lower amount of power in the simulation based on the simple geometrical model – despite having a similar trend with measured and accurately simulated APDPs. The simple geometrical model fails to predict several MPCs affecting the APDP due to many scatterers present in the real environment but missing in this model because of its limited accuracy.

Further, Fig. 7 presents the angular distribution for each Tx-Rx position. We learn that in the simulations for the close-range photogrammetry model, there are more taps on the power angular delay profile (PADP). This happens since the number of possible paths is higher in the close-range photogrammetry than in the simple geometrical model. It is visible in the following angular ranges: 1) [AoA = 100...200°; t = 250...300 ns], 2) [AoA = 270...300°; t = 250...300 ns], and 3) [AoA = 330...360°; t = 210...250 ns]. The first range represents an area where many small objects are distributed, including the parapet of the building near Tx1. The second and third ranges display the objects that are behind the Rx, such as the parabolic antenna located to its left, which is a major reflecting object. For the shortest link, the Tx1 location (Fig. 5), almost all the obstacles play an important role except for the objects in the areas 7 and 10-12 (Fig. 5(b)).

In order to understand whether this simple geometrical model can produce accurate results, we added to it some of the objects in the area 1 and the parapets. All other obstacles were not included as part of this simulation. The respective PDP can be observed in Fig. 6(a), red line with circle markers. Clearly, the PDP is significantly improved in relation to the measurement results. This means that the obstacles producing the most significant MPCs were identified correctly.

TABLE III. COMPARISON OF THE COMPUTATIONAL SPEED FOR TWO MODELS

Parameters	Simple geometrical model	Close-range photogrammetry model
Number of faces	~800 pcs	~28000 pcs
Calculation time	3 hours	8 hours
RAM consumption	< 1 GB	< 8 GB

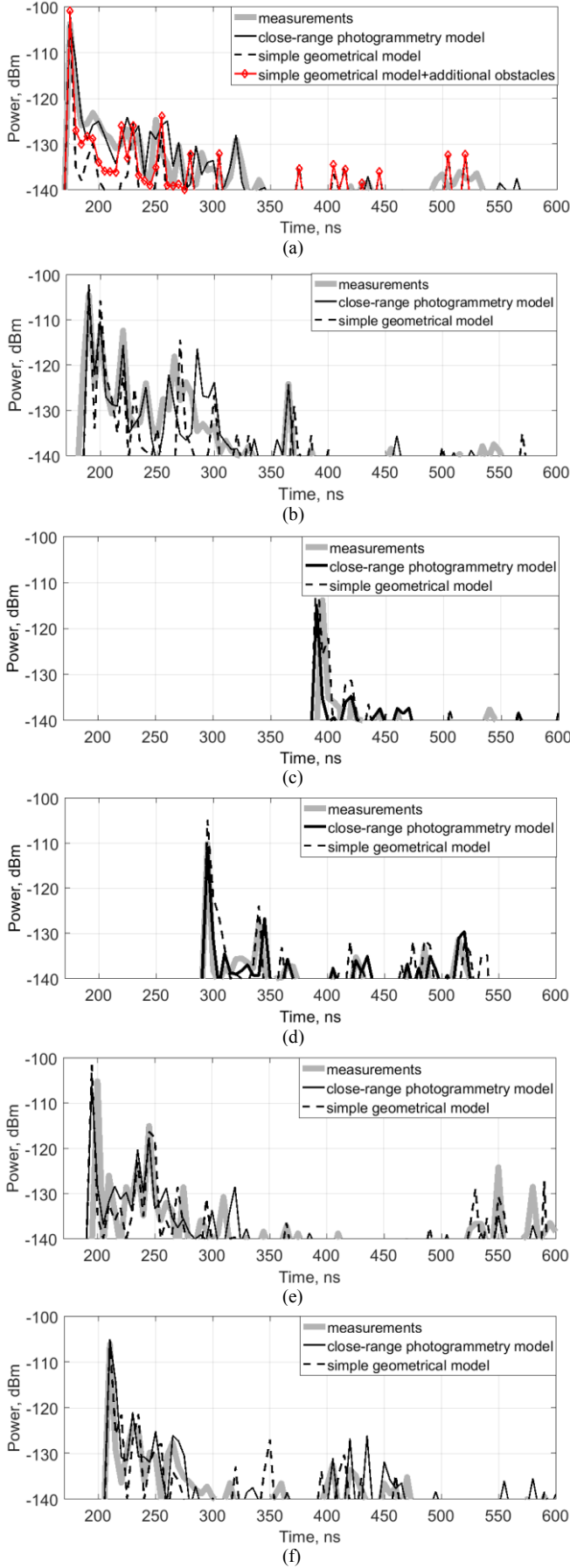


Fig. 6. Averaged PDPs at different Tx positions: (a) position 1, (b) position 2, (c) position 3, (d) position 4, (e) position 5, (f) position 6.

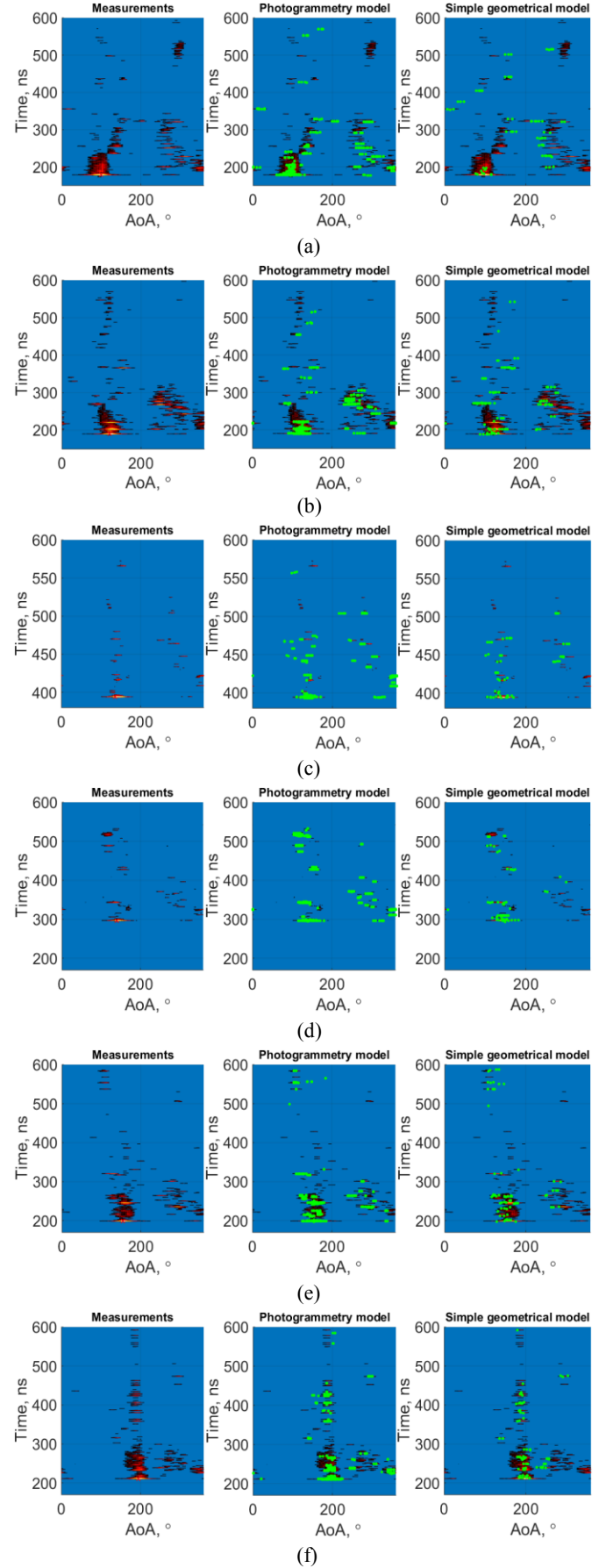


Fig. 7. PADPs at different Tx positions: (a) position 1, (b) position 2, (c) position 3, (d) position 4, (e) position 5, (f) position 6. Left image – measurements, center image – close-range photogrammetry model, right image – simple geometrical model.

TABLE IV. COMPARISON BETWEEN TWO MODELS ON THE MEAN ERRORS AND RECEIVED POWER

Tx position	Measurement results		Simple geometrical model (simulations)			Close-range photogrammetry model (simulations)		
	LOS distance	Received power, P_{tot}	Mean AoA error	Mean time error	$P_{tot}^{Rx}/P_{tot error}^{Rx}$	Mean AoA error	Mean time error	$P_{tot}^{Rx}/P_{tot error}^{Rx}$
1	53.6 m	-93.5 dB	3.2 °	1.2 ns	-100.8/-7.3 dB	2.1 °	1.1 ns	-96.6/-3.1 dB
2	57.0 m	-96.4 dB	3.8 °	2.2 ns	-101.5/-5.1 dB	3.0 °	2.0 ns	-99.3/-2.9 dB
3	118.2 m	-103.5 dB	4.7 °	3.5 ns	-111.7/-8.2 dB	3.1 °	3.1 ns	-106.8/-3.3 dB
4	89.0 m	-99.6 dB	4.0 °	2.9 ns	-103.7/-4.1 dB	3.9 °	2.4 ns	-101.6/-2.0 dB
5	59.7 m	-100.4 dB	2.2 °	1.6 ns	-107.1/-6.7 dB	2.1 °	0.9 ns	-102.1/-2.1 dB
6	63.3 m	-96.9 dB	3.9 °	2.6 ns	-102.8/-5.9 dB	2.9 °	2.0 ns	-99.3/-2.4 dB

Interference is another important effect, which is studied in the obtained results. Analytically, it is described as a phasor component $e^{j\phi}$ rotating the magnitude value in the complex coordinate system. Incoherent summing of all the MPCs arriving at the Rx can result in either constructive or destructive interference. The latter can be observed at 270 ns on the position Tx2 in the PDP plot, where interference arises from a number of significant MPCs arriving from the parapet. As a result, the received power drops down to 7 dB.

Considering the short wavelengths at mm-wave frequencies, it is not always possible to achieve an ideal reconstruction of the environment under study. Generally, interference of non-significant MPCs is averaged in the PADP and is not visible. However, the interfered dominant paths create considerable deep notches (destructive) or high peaks (constructive). The interference error can be reduced by carefully identifying the obstacles that produce the most significant paths, and representing them in details of their geometrical size. In the simple geometrical model, several important MPCs are not simulated, while some non-existing MPCs emerge. For instance, this can be observed for the position Tx2 at 280 ns and for Tx6 at 350 ns. The first non-existing path was generated by the obstacles in area 2 (Fig. 5(b)), whereas the second path was generated by the obstacles in area 12, with a significant 8 dB higher value of the received power in relation to the measured results.

One approach to compare the accuracy of the results from simulations based on the simple geometrical and the highly accurate model is to compare the received power levels with respect to the measurements. These values show the deviation between the simulations and measurements as presented in the sixth and ninth columns of Table IV. The absolute values of power for the close-range photogrammetry model are consistently lower than those corresponding to the simple geometrical model. This indicates a better performance of the highly accurate model in capturing even the insignificant effects of multipath over longer distances. It should therefore be noted that the use of highly accurate models is preferred.

VI. CONCLUSIONS AND DISCUSSION

In this work, we have verified that the more detailed 3D environmental models can provide better agreement between the simulation and the measurement results in terms of the APDP in mm-wave propagation modeling. This is a direct consequence of addressing the need for highly accurate models, since at mm-wave frequencies the small-sized objects

play a critical role in electromagnetic wave scattering and propagation because they become electrically large compared to the wavelength. A better agreement is visible for all the Tx locations when contrasting the simulation results based on the simple geometrical model with those based on the more advanced photogrammetry-based model.

It is shown that the photogrammetry technique can be cost-effective and accurate for the purposes of radio wave propagation prediction in mm-wave bands. A comparison between the measurement and simulation results at 60 GHz by using two 3D models with different levels of detail is presented. The ongoing development process of IEEE 802.11ay specifications promises to make the 60 GHz frequency range readily available for short-range outdoor communications. Photogrammetry makes it possible to create highly accurate 3D models, which can then be used in e.g., ray-optics modeling software. The photogrammetry techniques can also be beneficial in the reconstruction of densely populated city areas, where LIDAR technology is difficult to use. In contrast, the utilization of small and ultra-small UAVs provides an opportunity to obtain the required images and create highly accurate 3D models of complex environments for future planning of the mm-wave network deployments.

We have also produced a similar set of measurements and simulations at 15 GHz. These results reveal that the difference is not significant when the simple geometrical and highly accurate models are employed. This can be explained by the fact that the objects on the rooftop are smaller or almost of the same size as the wavelength. Studying other frequency ranges is a part of our current work. Finally, we verified that more detailed 3D environmental models can achieve a better agreement between the simulation and measurement results in terms of the PDP for the purposes of mm-wave propagation modeling. Specifically, for close-range distances it is observed (Tx positions 1 and 2 with the distance from the Rx of 53 and 57 m, respectively) that the simulations using the close-range photogrammetry model provide higher precision.

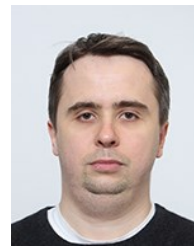
REFERENCES

- [1] IEEE 802.15.3c-2009, Part 15.3: Wireless Medium Access Control (MAC) and Physical Layer (PHY) Specifications for High Rate Wireless Personal Area Networks (WPANs), Amendment 2: Millimeter-wave-based Alternative Physical Layer Extension, Oct. 2009.
- [2] IEEE 802.11ad-2012, Part 11: Wireless LAN Medium Access Control (MAC) and Physical Layer (PHY) Specifications, Amendment 3:

- Enhancements for Very High Throughput in the 60 GHz Band, Dec. 2012.
- [3] P. Almers, E. Bonek, A. G. Burr, N. Czink, M. Debbah, and V. Degli-Esposti, "Survey of channel and radio propagation models for wireless MIMO systems," *EURASIP Journal on Wireless Communications and Networking*, Open Access, pp. 1-19, February, 2007.
 - [4] S. Sun, T. S. Rappaport, T. A. Thomas, A. Ghosh, H. Nguen, I. Z. Kovacs, I. Rodriguez, O. Koymen, and A. Partyka, "Investigation of prediction accuracy, sensitivity, and parameter stability of large-scale propagation path loss models for 5G wireless communications," *IEEE Transactions on Vehicular Technology*, 2016, doi: 10.1109/TVT.2016.2543139.
 - [5] S. Sun, T. A. Thomas, T. S. Rappaport, H. Nguen, I. Z. Kovacs, and I. Rodriguez, "Path loss, shadow fading, and line-of-sight probability models for 5G urban macro-cellular scenarios," *IEEE Globecom Workshops*, San-Diego, CA, 2015, pp. 1-7.
 - [6] J. Järveläinen, K. Haneda, M. Kyrö, V.-M. Kolmonen, J. Takada, and H. Hagiwara, "60 GHz radio wave propagation prediction in a hospital environment using an accurate room structural model," *Loughborough Antennas and Propagation Conference (LAPC2012)*, Loughborough, 2012.
 - [7] U. T. Virk, K. Haneda, V.-M. Kolmonen, J.-F. Wagen, and P. Vainikainen, "Full-wave characterization of indoor office environment for accurate coverage analysis," *International Conference on Electromagnetics in Advanced Applications (ICEAA)*, Torino, 2013, pp. 1197-2000.
 - [8] J. Järveläinen, S. L. H. Nguyen, K. Haneda, R. Naderpour, and U. T. Virk, "Evaluation of millimeter-wave line-of-sight probability with point cloud data," *IEEE Wireless Communication Letters*, vol. 5, no. 3, pp. 228-231, June 2016.
 - [9] R. Mittra, *Computational Electromagnetics*, Springer, New-York, 2014.
 - [10] Z. Yun and M. F. Iskander, "Ray tracing for radio propagation modeling: principles and applications," *IEEE Open Access*, Vol. 3, July 2015, pp. 1089 – 1100.
 - [11] Z. Yun, S. Y. Lim, and M.F. Iskander, "Propagation prediction in urban areas using geospatial data available on the Internet," *IEEE Antennas and Propagation Society International Symposium*, San Diego, CA, July 2007, pp. 1-4.
 - [12] K. Kraus, *Photogrammetry: Geometry from Images and Laser Scans*, Second Edition, Berlin, Walter de Gruyter, 2007.
 - [13] J. Shan and C. K. Toth, *Topographic Laser Ranging and Scanning: Principles and Processing*, CRC Press, Boca Raton, 2009.
 - [14] National Oceanic and Atmospheric Administration (NOAA) Coastal Services Center, *Lidar 101: An Introduction to Lidar Technology, Data, and Applications*. Revised. Charleston, SC: NOAA Coastal Services Center, 2012.
 - [15] B. Draeyer and C. Streacha, *White paper: How accurate are UAV surveying methods?* February, 2014.
 - [16] F. Leberl, A. Irschara, T. Pock, P. Meixner, M. Gruber, S. Scholz, and A. Wiechert, "Point clouds: LIDAR versus 3D vision," *Photogrammetric Engineering & Remote Sensing*, vol. 76, no. 10, pp.1123-1134, Oct. 2010.
 - [17] G. Pop and A. Bucksch, "Combining modern techniques for urban 3D modelling," *IEEE International Geoscience and Remote Sensing Symposium (IGARSS2007)*, Barcelona, July, 2007, pp. 2067-2070.
 - [18] T. S. Rappaport, S. Sun, R. Mayzus, H. Zhao, Y. Azar, K. Wang, G. N. Wong, J. K. Schulz, M. Samimi, and F. Gutierrez, "Millimeter wave mobile communications for 5G cellular: it will work!," *IEEE Access*, 2013, doi: 10.1109/ACCESS.2013.2260813.
 - [19] M. Steinbauer, A. F. Molisch and E. Bonek, "The double-directional radio channel," *IEEE Antennas and Propagation Magazine*, vol. 43, no. 4, pp. 51-63, Aug. 2001.
 - [20] F. P. Fontan and P. M. Espinera, *Modelling the Wireless Propagation Channel*, Wiley, Chichester, UK, 2008.
 - [21] G. de la Roche, A. Alayon-Glazunov, and B. Allen, *LTE-Advanced and Next Generation Wireless Networks: Channel Modeling and Propagation*, John Wiley & Sons, 2012, 568 p.
 - [22] R. G. Kouyoumjian and P. H. Pathak, "A uniform geometrical theory of diffraction for an edge in a perfectly conducting surface," *Proceedings of the IEEE*, vol. 62, no. 11, pp. 1448-1461, Nov. 1974.
 - [23] F. Saez de Adana, O. Gutierrez, I. Gonzalez, M. F. Catedra, and L. Lozano, *Practical Applications of Asymptotic Techniques in Electromagnetics*, Artech House, Norwood, MA, 2011.
 - [24] J. Lu, D. Steinbach, P. Cabrol, P. Pietraski, and R. V. Pragada, "Propagation Characterization of an Office Building in the 60 GHz Band," *European Conference on Antennas and Propagation (EuCAP2014)*, The Hague, The Netherlands, Apr. 2014.
 - [25] K. Haneda, S. L. H. Nguyen, J. Järveläinen, and J. Putkonen, "Estimating the omni-directional pathloss from directional channel sounding," *European Conference on Antennas and Propagation (EuCAP2016)*, Davos, Switzerland, Apr. 2016.
 - [26] P. F. M. Smulders, "Broadband wireless LANs: a feasibility study," *PhD thesis*, Eindhoven University of Technology, The Netherlands, ISBN-90-386-0100-X, 1995.
 - [27] H. Xu, V. Kukshya, and T.S. Rappaport, "Spatial and temporal characteristics of 60-GHz indoor channels," *IEEE Journal on Selected Areas in Communications*, vol. 20, no. 3, pp. 620-630, Apr. 2002.



communications, especially reconfigurable antennas and radio-wave propagation modeling.



digital and mixed systems for critical applications.



European Union's Horizon 2020 project mm-MAGIC from 2015 to 2016. He is currently pursuing his Ph.D. studies at Swiss Federal Research Institute WSL Birmensdorf, Switzerland. His current research interests include application of microwave radiometry for the characterization of terrestrial snow cover and F/T cycles.



more than 90 published research works on wireless communications, energy efficiency, heterogeneous networking, cooperative communications, and machine-to-machine applications.

Vasilii Semkin was born in Saint-Petersburg, Russia, in April 1988. He received B.Sc. degree with honors from Saint-Petersburg State University of Aerospace Instrumentation in 2009 and M.Sc. degree in 2011. He received Lic.Sc. (Tech.) in 2014 and D.Sc. (Tech.) in September 2016 from Aalto University, School of Electrical Engineering, Finland. He is currently working as a postdoctoral researcher at Aalto University, Department of Radio Science and Engineering. He is studying 60 GHz

Dmitrii Solomitskii (dmitrii.solomitskii@tut.fi) is a PhD student in the Department of Electronics and Communications Engineering at Tampere University of Technology, Finland. He received both BSc (2006) and MSc (2008) degree from St. Petersburg Electrotechnical University "LETI". Dmitrii's area of interest in wireless communication focused on propagation physics, antennas, modeling and signal processing. He also has extensive experience in design, manufacturing and testing of analogue,

Reza Naderpour received his M.Sc. degree in electrical engineering from Aalto University, Espoo, Finland in 2014. From 2013 to 2014, he was a researcher with Aalto University, Department of Radio Science and Engineering, where he specialized in SMOS RFI analysis, radiometer calibration techniques and airborne measurements. He did his M.Sc. thesis in the field of Space Weather studies. He has also worked as a researcher in several mobile communications technology projects including the

Sergey Andreev (sergey.andreev@tut.fi) is a Senior Research Scientist in the Department of Electronics and Communications Engineering at Tampere University of Technology, Finland. He received the Specialist degree (2006) and the Cand.Sc. degree (2009) both from St. Petersburg State University of Aerospace Instrumentation, St. Petersburg, Russia, as well as the Ph.D. degree (2012) from Tampere University of Technology. Sergey (co-)authored



Yevgeni Koucheryavy (yk@cs.tut.fi) is a Full Professor and Lab Director at the Department of Electronics and Communications Engineering of Tampere University of Technology (TUT), Finland. He received his Ph.D. degree (2004) from TUT. He is the author of numerous publications in the field of advanced wired and wireless networking and communications. His current research interests include various aspects in heterogeneous wireless communication networks and systems, the Internet of

Things and its standardization, as well as nanocommunications. He is Associate Technical Editor of IEEE Communications Magazine and Editor of IEEE Communications Surveys and Tutorials.



Antti V. Räsänen (F'94 - LF'16) received the D.Sc.(Tech.) degree in EE from the Helsinki University of Technology (TKK) (now Aalto University), Espoo, Finland, in 1981. In 1989, he was appointed Professor Chair of Radio Engineering with TKK, after holding the same position *pro tem* in 1985 and 1987–1989. He has been a Visiting Scientist and Professor with the Five College Radio Astronomy Observatory (FCRAO) and the University of Massachusetts at Amherst (1978–1979,

1980, 1981); the Chalmers University of Technology (1983); the University of California at Berkeley (1984–1985); the Jet Propulsion Laboratory (JPL) and California Institute of Technology (1992–1993); Observatoire de Paris and Université de Paris 6 (2001–2002), and Universidad Carlos III de Madrid (2013–2014).

He supervises research in millimeter-wave components, antennas, receivers, microwave measurements, etc., at the Aalto University, Department of Radio Science and Engineering and Millimetre Wave Laboratory of Finland - ESA External Laboratory (MilliLab). He has authored or coauthored over 500 scientific or technical papers and seven books, e.g., *Semiconductor Terahertz Technology: Devices and Systems at Room Temperature Operation* (Wiley, 2015).

Dr. Räsänen is Fellow of the Antenna Measurement Techniques Association (AMTA) since 2008. He was the recipient of the AMTA Distinguished Achievement Award in 2009. The Chair of Excellence by the University Carlos III of Madrid was awarded to him in 2013. He has been Conference Chairman of several international microwave and millimeter-wave conferences including the 1992 European Microwave Conference and the 2016 Global Symposium on Millimeter Waves. He was an Associate Editor of the *IEEE Transactions on Microwave Theory and Techniques* (2002–2005). He was a member of the Board of Directors of the European Microwave Association (EuMA) (2006–2011). He is currently Head of the Department of Radio Science and Engineering and Chair of the Board of Directors, MilliLab.

PUBLICATION

III

**Toward massive ray-based simulations of mmWave small cells on open urban
maps**

D. Solomitckii, M. Gapeyenko, S. Szyszkowicz, S. Andreev, H. Yanikomeroglu
and Y. Koucheryavy

IEEE Antennas and Wireless Propagation Letters 16.(2016), 1435–1438

DOI: 10.1109/LAWP.2016.2641339

Publication reprinted with the permission of the copyright holders

Towards Massive Ray-Based Simulations of mmWave Small Cells on Open Urban Maps

Dmitrii Solomitckii, Margarita Gapeyenko, Sebastian S. Szyszkowicz, *Member, IEEE*
Sergey Andreev, Halim Yanikomeroglu, *Senior Member, IEEE* and Yevgeni Koucheryavy

Abstract—High-rate access in outdoor urban areas using extremely high frequency (EHF) bands, known as *millimeter-wave* (mmWave) spectrum, requires a dense deployment of wireless small cells in order to provide continuous coverage to served bandwidth-hungry users. At the same time, to be able to collect a sufficient amount of data for constructing detailed EHF propagation models, a considerable number of various landscape maps across different scenarios has to be considered. This letter develops a *shoot-and-bounce ray (SBR)* based methodology capable of characterizing the mmWave propagation in *urban outdoor* conditions. In particular, our methodology aims to capture a large number of small cells within accurate, *real city maps* and utilizes an algorithm of automatic transmitter placement. Hence, our contribution is to provide with a suitable tool that is able to handle *massive ray-based simulations* within a reasonable time frame. In particular, we demonstrate and verify that a shift from simulating 3D to evaluating 2D environments significantly reduces computation time while only slightly decreases the simulation accuracy.

Index Terms—Dense urban deployments; mmWave small cells; shoot-and-bounce ray simulator; massive ray-based simulations.

I. INTRODUCTION AND BACKGROUND

The increase in traffic demand together with the growing needs for higher user data rates and lower latencies require the introduction of innovative concepts as part of the fifth-generation (5G) mobile networks. The extremely high frequency (EHF) band is a promising candidate to support many key requirements of next-generation wireless communication systems. Making larger bandwidths available, the millimeter-wave (mmWave) spectrum operating in the EHF band is expected to provide several Gbps of data rate [1].

In addition to its benefits, mmWave system operation also poses unprecedented challenges. One of these is completely *new channel characterization* that is not applicable in lower frequency bands. Due to the very different nature of mmWave spectrum, one of the potential difficulties is considerable *blockage* caused by smaller objects [2], [3]. In addition, diffuse scattering needs to be accounted for in mmWave systems. All of the above brings the need to comprehensively analyze

the propagation characteristics that are not similar to those in lower frequency bands.

For the above reasons, multiple studies focused on obtaining statistics desirable for channel characterization through real measurements or simulations. Today, deterministic site-specific tools, such as 3D ray-tracing (RT) and ray-launching (RL), remain widely popular to simulate wireless propagation in indoor and outdoor environments alike. Even though there are numerous works describing the RT tools in order to quantify the channel characteristics, the main limitation of the past studies is in their small study regions. Also, although various techniques were employed to speed up the simulations [4], the resultant speed may still not be sufficient to capture larger city maps with many transceivers. A propagation study over a vast urban area has the advantage of being more representative of the entire city, without potential artifacts arising from investigating a particular location. Since placing many transmitters (TXs) by hand is impractical, an algorithm needs to be developed for this purpose, e.g., [5].

In this letter, we outline a methodology that can statistically describe wireless channel properties based on the deterministic data obtained from a *large number of real maps*. The obtained data can be used to gain a deeper understanding of the mmWave propagation properties of the typical city. Moreover, our methodology is also capable of resolving the main challenges that arise from obtaining a large number of statistical inputs needed for channel modeling. As small cells in the EHF bands are expected to offer shorter coverage ranges compared to those in the lower frequency bands [1], [3], it is important to have more TXs for uninterrupted coverage. It leads to reliable connectivity for system operators which should also benefit the connection quality of the end users.

The rest of this letter is organized as follows. The descriptions of the proposed methodology and the map preparation are provided in Section II. In Section III, the deterministic site-specific simulation tool is described. The verification of the proposed methodology is provided in Section IV. The conclusions and future work are highlighted in the last section.

II. PROPOSED METHODOLOGY

In order to simulate a significant number of maps, it is important to have the key components including (i) a large database of maps, (ii) an algorithm for the automatic placement of TXs on a map, and (iii) a fast ray-based simulation tool. The flowchart of the proposed methodology is provided in Fig. 1. The core idea is based on generating multiple maps,

D. Solomitckii, M. Gapeyenko, S. Andreev, and Y. Koucheryavy are with the Department of Electronics and Communications Engineering, Tampere University of Technology, Tampere, Finland (e-mail: {dmitrii.solomitckii, margarita.gapeyenko, sergey.andreev}@tut.fi, yk@cs.tut.fi).

S. S. Szyszkowicz and H. Yanikomeroglu are with the Department of Systems and Computing Engineering, Carleton University, Ottawa, Canada (e-mail: {sz, halim}@sce.carleton.ca).

This research was funded in part by TELUS Corporation and supported in part by the Academy of Finland and in part by the project TT5G: Transmission Technologies for 5G.

automatically producing 'good' TX locations for each one, and uploading the maps into a ray-based simulator one by one. As the maps of interest are processed, the statistical data can be used to derive accurate channel models for large urban areas.

The real maps of 2D buildings can be extracted from the OpenStreetMap project (or similar) as described in [5], [6], where each building is represented by a simple polygon. The adjacent buildings are merged together and the inside areas (e.g., courtyards) are removed. The algorithm that searches for the appropriate TX locations on the facades of the buildings is described in [5]; it identifies the TX positions that lead to the good line-of-sight (LOS) area within a certain distance (200 m based on current mmWave research [1], [3], [5]).

In this letter, we focus on the verification of our methodology by using a typical urban area: Manhattan Island. However, the choice of the urban area is not limited to our example, and we plan to use other areas in the future studies. The Manhattan grid is used as a reference use case in many existing standards, such as [7], and one can therefore reasonably compare these results with other work. In Section IV, we contrast the overall accuracy of our methodology against the models proposed by 3GPP [7] for the urban microcell (UMi) case.

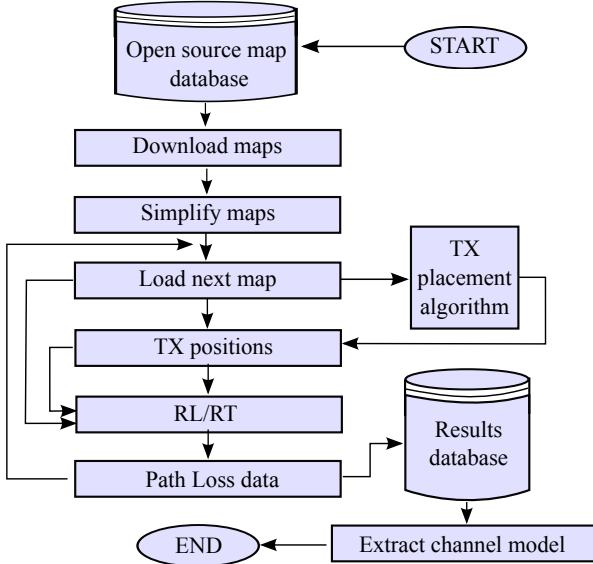


Fig. 1. Flowchart of the proposed methodology.

According to this methodology, we study 9 square maps, each with 10 deployed TXs (see Fig. 2), which are chosen randomly from the candidate points generated by the algorithm in [5]. The middle map of our simulation campaign is shown at the bottom part of Fig. 2. Every map is of size 1000 m x 1000 m, but only the inner 600 m x 600 m square is considered for the TX locations to avoid edge effects. Therefore, different maps may overlap partially to reuse the building-related data. Our simulation scenario is summarized in Table I.

III. SIMPLIFIED RAY-BASED SIMULATOR

A. 3D to 2D conversion

To perform the targeted massive simulations and extract a significant amount of statistical data, one of the key compo-

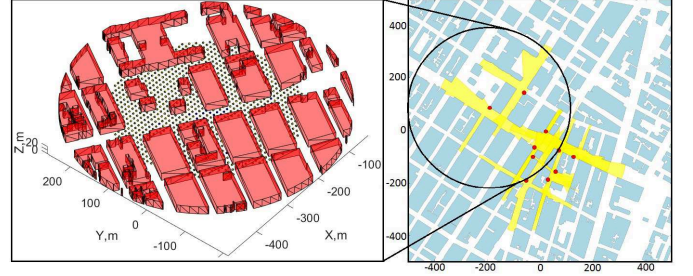


Fig. 2. Sample map of Manhattan Island (right image), centered at (73.99W, 40.73N) with 10 TXs placed on wall sides, with good LOS coverage (shown in yellow). Our simulation campaign comprises 9 of such maps. Each of the maps is divided into areas (left image) with the TX in the center.

nents is to have a ray-based simulation tool that is fast enough. For this purpose, we reduce the space dimensionality of our ray propagation simulator as well as that of the maps from true 3D to 2D. This transformation becomes possible because mmWave access points are expected to be located significantly below rooftop and the rooftop diffraction is discarded. Based on that wave propagation occurs in a 2D XY-plane, when multiple TXs and receivers (RXs) are positioned at the same height. In case the TX height differs from that of the RX, the XY-plane transforms (typically, rotates around X or Y axis), so that both antennas belong to it and the propagation occurs in the modified plane. However, a 2D implementation – due to the absence of the third dimension (Z-axis) – has a limitation in that it does not easily take into account the role of the ground-reflected beams. Thus, we added extra beams reflected from the ground. This was done utilizing the elements of the so-called two-ray model [8], without any additional geometric simulations, which are very demanding in terms of time consumption. The above improvements are valid if it is assumed that all of the building walls are orthogonal to the ground plane, which is common for urban scenarios. If some of these requirements cannot be met, then a true 3D ray-based simulator must be used.

B. Utilized SBR Ray-Launching method

A key element in accelerating ray-based simulations is the image-based SBR method, whose basic principles were described in literature [9]–[11]. Accordingly, the geometrical engine searches paths between mutually visible objects (walls, edges, antennas, etc.) using the image method. Then, the physical engine calculates a number of phenomena, such as reflection, transmission, and diffraction, by following the geometrical optics (GO) approach and employing the uniform theory of diffraction (UTD). Our hybrid technique integrates the image-based RT (ray-tracing) and brute-force ray-launching, removing all the inherent limitations of both models. The main advantage is in lower simulation time with respect to the canonical RT and RL, which plays a crucial role in massive simulations.

To materialize the gains, an enhanced SBR-based geometrical engine was designed, which comprises two stages: (i) construction of a hierarchical visibility tree and (ii) search for all the unique paths between the TX and the RX. The first tree

identifies all the mutually visible objects, whereas the second tree builds a visibility abstraction for the specific TX-RX pairs based on the first tree data. Such a hierarchical approach offers higher efficiency when hundreds of TXs within a complex scenario need to be simulated, but does not provide advantages in simpler scenarios. Once constructed, the first visibility tree for a single scenario may be used repeatedly by all the antennas, which unlocks a significant gain in terms of speed.

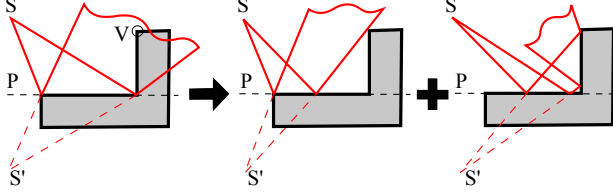


Fig. 3. Decomposition of the first beam (left image) from source S impinging on the internal edge of plane P which produces $N+1$ secondary beams (center and right images), where N is number of occluded vertices V in main beam.

Instead of using thousands of infinitely thin lines as conventional RL does, the SBR operates with fewer beams, modeled by triangles. Such an approach reduces the amount of processing, but requires smart algorithms for beam propagation and interaction modeling. One of the key tasks here is beam partitioning, which occurs when the beam impinges on a wall. Our implementation is based on a search of occluded vertices V within a triangle to perform the beam splitting, as shown in Fig. 3. The algorithm at its second stage builds TX-to-RX paths through the intermediate projections on objects that are included into the visibility tree from the first stage.

IV. SIMULATION RESULTS AND DISCUSSION

In this section, we present our 3D and 2D simulation results for multiple outdoor urban maps, which were obtained from the true 3D SBR, the true 2D SBR (propagation in a plane, without the ground-bouncing beams), and the improved 2D SBR (with ground bouncing beams). The TX positions were automatically planned in the central 600 m x 600 m area, while all the RXs are distributed across the outdoor locations. All of the antennas are isotropic and vertically polarized without any mismatch; their radiated power is 25 dBm and the frequency is 28 GHz. The material properties, such as the dielectric permittivity and conductivity for the considered scenario, were taken from [12].

To verify the accuracy of our improved 2D SBR, we compare its output with the key channel parameters considered by 3GPP, including the K-factor, the delay spread, the angle of arrival (AoA) spread, the angle of departure (AoD) spread, and the LOS probability. This is a crucial step, since all the wireless channel related metrics have to be exploited further on for other environments. Hence, they must first be validated by our study. To make a connection from 3GPP's stochastic/empirical models to the deterministic results, massive simulations need to be performed to collect as much statistics as possible. Finally, we average each of the above parameters, producing the mean value as per 3GPP procedures. The results are summarized in Table II.

TABLE I
OUR DEPLOYMENT PARAMETERS

Parameter	Value
Center of area of interest	73.99W 40.73N
Total area of interest	2000 m x 2000 m
Average coverage by buildings	47 %
Total number of maps	3 x 3
Individual map size	1000 m x 1000 m
Overlap of adjacent maps	by 500 m
Inner area size with Placed Tx	600 m x 600 m
Number of TXs	10 per map, 90 in total
TX height	10 m
RX locations	outdoor, RX-grid
RX height	1.5 m
Number of RXs	1250 per inner area
Building material	concrete ($\epsilon_r = 5.31$, $\sigma_r = 0.484$)
Antennas	isotropic radiator

The LOS probability and the path loss (PL) are compared in Fig. 4 and Fig. 5, respectively. Being a purely geometrical property, the LOS probability verifies our geometrical engine and is calculated in two steps: (i) connect each of the TX-RX pairs by a line and (ii) check for the intersections of the line with any surrounding objects.

TABLE II
COMPARISON WITH 3GPP PARAMETERS

Parameter	Improved 2D SBR	3GPP
Rician K-factor	$\mu = 13.7$	$\mu = 9$, $\sigma = 5$
$\log_{10}(\text{Delay spread, s})$	LOS: $\mu = -7.3$ NLOS: $\mu = -6.8$	LOS: $\mu = -7.49$, $\sigma = 0.38$ NLOS: $\mu = -7.18$, $\sigma = 0.51$
$\log_{10}(\text{AoA spread, }^\circ)$	LOS: $\mu = 1.5$ NLOS: $\mu = 2.1$	LOS: $\mu = 1.61$, $\sigma = 0.30$ NLOS: $\mu = 1.69$, $\sigma = 0.37$
$\log_{10}(\text{AoD spread, }^\circ)$	LOS: $\mu = 1.3$ NLOS: $\mu = 1.4$	LOS: $\mu = 1.13$, $\sigma = 0.41$ NLOS: $\mu = 1.19$, $\sigma = 0.49$

μ : mean parameter value; σ : standard deviation of parameter value

It can be observed that the simulated mean value (μ) of channel properties in Table II, Fig. 4, and Fig. 5 are close to the ones proposed by 3GPP in [7]. However, the properties shown in Table II for some of the RXs in non-LOS (NLOS) conditions are outside of the standard deviation limit (σ) considered by 3GPP for the bands above 6 GHz. The reason for this is the restrictions of the 3GPP environment, which assumes the idealized Manhattan grid. While we also select Manhattan city maps for our simulations, most real layouts still have irregular Manhattan grid topology (see Fig. 2), with blocks and perpendicular roads between them. Hence, real beams may propagate much longer/shorter distances comparing to the paths in the canonical Manhattan grid topology.

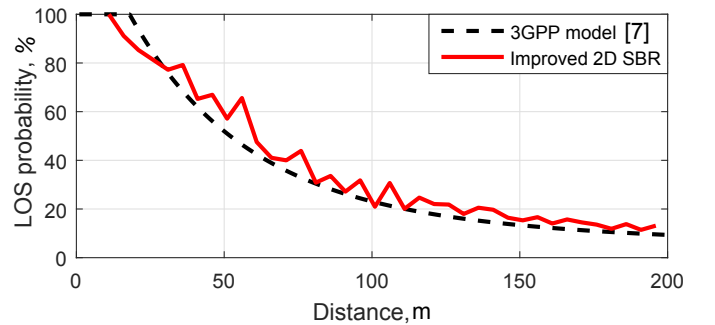


Fig. 4. Comparison of LOS probability: improved 2D SBR with ground-bouncing rays vs. 3GPP model [7].

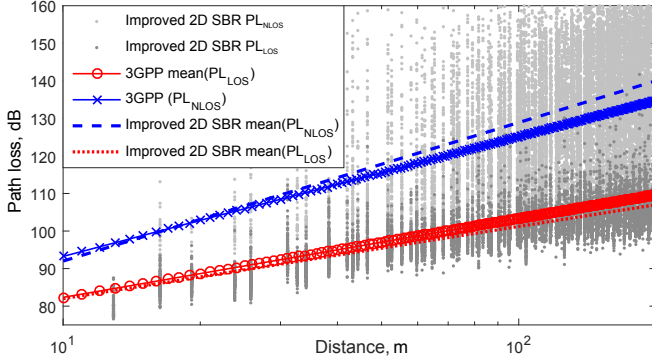


Fig. 5. Comparison of path loss: improved 2D SBR vs. 3GPP model [7]. Dark points are PL from TX to LOS RXs; light points are PL to LOS RXs.

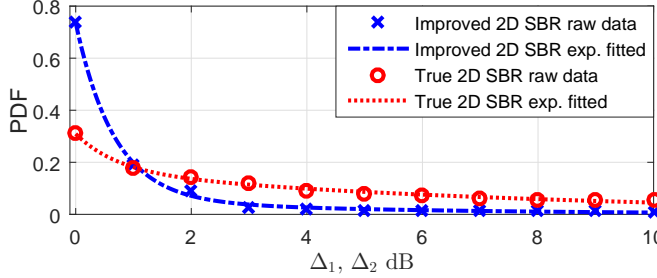


Fig. 6. Total received power difference: improved SBR vs. true 2D SBR.

Another aspect that we cover in this letter is the role and the importance of the ground-bouncing rays for the total received power calculations. Therefore, we compare the true 3D SBR, the true 2D SBR, and the improved 2D SBR (with additional ground-bouncing rays) in terms of the simulation time and accuracy of the total received power estimation. The output results indicate that the true 2D SBR and the improved 2D SBR are approximately 15 times faster compared to the true 3D SBR, since the amount of processing is lower. The accuracy of the total received power calculations is given as the distribution of difference between the true and the improved 2D SBRs versus the 3D SBR as follows:

$$\Delta_1 = |P_{3DSBR_{true}}^{tot} - P_{2DSBR_{true}}^{tot}|, \quad (1)$$

$$\Delta_2 = |P_{3DSBR_{true}}^{tot} - P_{2DSBR_{improved}}^{tot}|. \quad (2)$$

In other words, we characterize the distribution of differences Δ_1 and Δ_2 among RXs in true and improved 2D SBR, respectively (shown in Fig. 6). It can be noted that the results obtained with the improved 2D SBR are closer than those obtained with true 3D SBR, and the additional ground-bouncing beams really make a difference. The maximum observed Δ_2 is about 5 dB (only for 1 % of all RXs) and almost 80 % of the RXs have their total received power similar to the true 3D SBR.

V. CONCLUSION AND FUTURE WORK

The different propagation effects of the EHF band together with the smaller cell coverage ranges require a novel modeling approach that is capable of supporting extensive studies of the mmWave channel. Along these lines, the main focus of this

letter is massive simulations for a large number of mmWave small cells located on multiple maps of a real city. With respect to the existing RL and RT studies focused mainly on simulating a single map of a simplified deployment, our methodology extends the limits of deterministic modeling towards statistical studies. Results produced by the approach might be used to develop new analytical models as well as to complement the existing standards such as COST, WINNER, 3GPP, ITU-R and others. In this letter, we propose a novel 2D SBR-based methodology that is able to collect the mmWave channel statistics from several realistic city maps in a reasonable time. We observe that the computation time for our 2D SBR is about 15 times shorter than that for the true 3D SBR. Further, adding ground-bounce rays to the 2D SBR may significantly improve the total accuracy while maintaining efficient simulation times.

Finally, we compared the output of the 2D RL against the existing 3GPP models and confirmed that the proposed methodology offers an accurate approach to collecting statistical data in the environment of interest. One limitation of our improved 2D SBR is in that it can only work in the deployments where all of the walls are strictly perpendicular to the ground and the antennas are positioned significantly below rooftops. As our next step, we aim to validate our 2D SBR simulator against mmWave measurements. In addition, we may need to design methods that support beamforming antenna arrays, which will become an important consideration in the future mmWave systems.

REFERENCES

- [1] J. G. Andrews, S. Buzzi, C. Wan, S. V. Hanly, A. Lozano, A. C. K. Soong, and J. C. Zhang, "What will 5G be?," *IEEE Journal on Selected Areas in Communications*, vol. 32, pp. 1065–1082, June 2014.
- [2] M. Jacob, S. Priebe, T. Kurner, M. Peter, M. Wisotzki, R. Felbecker, and W. Keusgen, "Fundamental analyses of 60 GHz human blockage," in *Proc. of European Conference on Antennas and Propagation (EuCAP)*, April 2013.
- [3] S. Rangan, T. S. Rappaport, and E. Erkip, "Millimeter-wave cellular wireless networks: Potentials and challenges," *Proceedings of the IEEE*, vol. 102, pp. 366–385, March 2014.
- [4] G. Durgin, N. Patwari, and T. S. Rappaport, "An advanced 3D ray launching method for wireless propagation prediction," in *IEEE Vehicular Technology Conference (VTC)*, vol. 2, May 1997.
- [5] S. S. Szyszkowicz, A. Lou, and H. Yanikomeroglu, "Automated placement of individual millimeter-wave wall-mounted base stations for line-of-sight coverage of outdoor urban areas," *IEEE Wireless Communication Letters*, June 2016.
- [6] M. Mirahsan, R. Schoenen, S. S. Szyszkowicz, and H. Yanikomeroglu, "Spatial heterogeneity of users in wireless cellular networks based on open urban maps," in *IEEE International Conference on Communications (ICC)*, June 2015.
- [7] "Channel model for frequency spectrum above 6 GHz (Release 14)," *3GPP TR 38.900 V2.0.0*, June 2016.
- [8] R. Aquino-Santos, *Wireless Technologies in Vehicular Ad Hoc Networks: Present and Future Challenges*. IGI Global, 2012.
- [9] H. S. Sato and K. Otoi, "Electromagnetic wave propagation estimation by 3-D SBR method," *Electromagnetics in Advanced Applications, ICEAA*, pp. 129–132, September 2007.
- [10] S. H. Chen, "An SBR/image approach for radio wave propagation in indoor environments with metallic furniture," *IEEE Transactions on Antennas and Propagation*, vol. 1, pp. 98–106, February 1997.
- [11] S. Chen and S. K. Jeng, "SBR image approach for radio propagation in tunnels with and without traffic," *IEEE Transactions on Antennas and Propagation*, vol. 3, pp. 570–578, September 1996.
- [12] "Effects of building materials and structures on radiowave propagation above about 100 MHz," *ITU-R P.2040-1*, July 2015.

PUBLICATION

IV

**Detailed interference analysis in dense mmWave systems employing
dual-polarized antennas**

D. Solomitckii, V. Petrov, H. Nikopour, M. Akdeniz, O. Orhan, N. Himayat,
S. Talwar, S. Andreev and Y. Koucheryavy

IEEE Globecom Workshops (GC Wkshps). Ed. by 2017

DOI: 10.1109/GLOCOMW.2017.8269040

Publication reprinted with the permission of the copyright holders

Detailed Interference Analysis in Dense mmWave Systems Employing Dual-Polarized Antennas

Dmitrii Solomitskii*, Vitaly Petrov*, Hosein Nikopour†, Mustafa Akdeniz†, Oner Orhan†, Nageen Himayat†, Shilpa Talwar†, Sergey Andreev*, and Yevgeni Koucheryavy*

*Tampere University of Technology, Tampere, Finland

†Intel Labs, Santa Clara, CA, USA

Abstract—The use of extremely high frequency (EHF) bands, known as millimeter-wave (mmWave) frequencies, requires densification of cells to maintain system performance at required levels. This may lead to potential increase of interference in practical mmWave networks, thus making it the limiting factor. On the other hand, attractive utilization of dual-polarized antennas may improve over this situation by mitigating some of the interfering components, which can be employed as part of interference control techniques. In this paper, an accurate two-stage ray-based characterization is conducted that models interference-related metrics while taking into account a detailed dual-polarized antenna model. In particular, we confirm that narrower pencil-beam antennas (HPBW = 13°) have significant advantages as compared to antennas with relatively narrow beams (HPBW = 20° and HPBW = 50°) in the environments with high levels of interference. Additionally, we demonstrate that in the Manhattan grid deployment a transition from interference-to noise-limited regime and back occurs at the cell inter-site distances of under 90 m and over 180 m, respectively.

I. INTRODUCTION

A significant growth in the number of connected devices (smart phones, smart cars, etc.) and their capabilities leads to unprecedented technical challenges that need to be solved in order to provide the needed data rate, reliability, and availability. These challenges are addressed by the major stakeholders in the telecommunication sector, who currently construct the 5th generation (5G) mobile technologies. These are preparing to utilize new frequency bands above 6 GHz (termed “millimeter-wave” or “mmWave”) with the bandwidth of up to 2 GHz [1].

Despite the benefits made available with larger bandwidths, mmWave frequencies have a number of specific physical properties that are different from those in existing microwave (uWave) bands employed by 3rd and 4th generation of cellular standards. Some of these properties are: significant pathloss (PL), notable penetration losses, and negligible diffraction, all effectively shrinking the coverage radius of the mmWave-based communication systems. We recall that network densification with wireless access nodes is a mainstream trend, mostly motivated by the need to increase the area spectral efficiency. Hence, small inter-site distance (ISD) between mmWave base stations (BSs) is a mandatory requirement for uninterrupted coverage. Hence, realistically, the coverage range of a single mmWave BS in urban environments will not go far beyond several hundreds of meters [2].

The use of directional antennas is another key requirement for large-scale deployment of mmWave systems. First, it

allows to partly compensate for the propagation losses and significant noise levels over wider mmWave channels by keeping the coverage ranges and the ISD values at the desired levels: hundreds of meters instead of tens for omnidirectional mmWave transmissions. Second, high-gain antennas reduce the interference levels at both the user equipment (UE) and the BS sides [3], [4]. It has also been shown theoretically that mmWave systems are primarily noise-limited (in other words, the interference levels are negligible) [5].

At the same time, higher density of mmWave BSs (to further increase the area capacity) as well as the use of wider beams (due to imperfections in the beam alignment algorithms and hardware limitations) may lead to the situation, where the mmWave system begins to experience notable and significant levels of interference. Hence, the noise-limited mmWave system may transition to the interference-limited regime. Therefore, a study on appropriate scaling of interference impact in mmWave systems as a function of the BS density and antenna directivity in realistic environments is of crucial importance for the purposes of network planning and deployment optimization of costly 5G mmWave cellular networks.

There has been some literature coverage aiming to evaluate the realistic levels of interference in mmWave systems. Most of past works use either stochastic or empirical models that represent the environment as a series of random variables or equations based on pre-measured data. For instance, in [6] a stochastic performance characterization of the mmWave communication network is conducted in a constrained area with a finite number of interferers at fixed positions. Another interference-related study has been completed in [7], where a novel interference model was presented with a mixture of Inverse Gaussian and Inverse Weibull distributions.

In [5], [8], and [9] the authors investigated noise and interference limitations of the mmWave network by using empirical/stochastic approaches. In addition, [10] introduced an analytical framework for estimating the collision probability as a function of the antenna patterns and the density of simultaneously transmitting nodes. Recently, deterministic approaches to target the problem of interference modeling have been exploited by [11]. That paper presented a framework for indoor mmWave propagation modeling based on deterministic image-based ray-tracing methods to capture channel properties for specific antennas and environments having multiple transceivers.

While several works offer some insight into the behavior of interference at mmWave frequencies and the associated scaling laws, they do not take into account the specifics of mmWave equipment, such as antenna polarization issues, spatial diversity of mmWave propagation between multi-antenna arrays, as well as imperfections of the practical beamforming patterns. This in practice results in a more complex structure of the interfering signal at the receiver. While some aspects of the described problem have in part been studied by the recent works – for instance, the role of polarization diversity in MIMO systems has been investigated in [12] and the practical codebooks have been taken into account by [13], [14] – to the best of our knowledge there has been no systematic study on interference in mmWave systems, which jointly takes into account the important hardware-related aspects, including realistic antenna radiation pattern, specifics of the mmWave MIMO channel, and polarization of the antenna elements.

In this paper, we conduct this much-needed study. We first introduce our comprehensive in-house modeling framework that is capable of highly-accurate mmWave system modeling and calibrate it against reliable measurement results. We then describe the required functionality that has been developed in order to capture the transition of the mmWave system from the noise-limited to the interference-limited regime. We finally contribute and analyze the results of our performed evaluation for 28 GHz frequency band and Manhattan grid topology, by demonstrating the impact of interference for different values of ISDs and antenna radiation patterns. Our obtained numerical values are grounded in reality and can be used as a reference for calibration of both existing and future interference models for mmWave systems.

The rest of this paper is organized as follows. Our deployment scenario and the target metrics of interest are summarized in Section II. The relevant peculiarities of the mmWave propagation and the details of the utilized evaluation framework are described in Section III. Section IV is dedicated to the obtained numerical results and the corresponding discussion. The paper concludes with some general remarks offered in Section V.

II. TARGET MMWAVE DEPLOYMENT

The standard Manhattan grid scenario has been selected for our interference-centric study. This layout is representative of many real cities in the world that have modern architecture. The Manhattan grid also constitutes the basic reference topology in many wireless standardization documents, such as those by METIS [15], WINNER-II, COST, and 3GPP. However, depending on the geometrical size of buildings and the width of roads, the Manhattan grid maps may differ from each other in terms of radio signal propagation.

For consistency and to calibrate the intermediate results, we followed 3GPP with respect to the geometrical parameters of the Manhattan grid deployment [16]. Multiple mmWave BSs (169 nodes) are distributed according to the BS-grid with the equidistant step of 45 m (see Fig. 1). Since our study is focused on an outdoor case, the BSs inside buildings are not

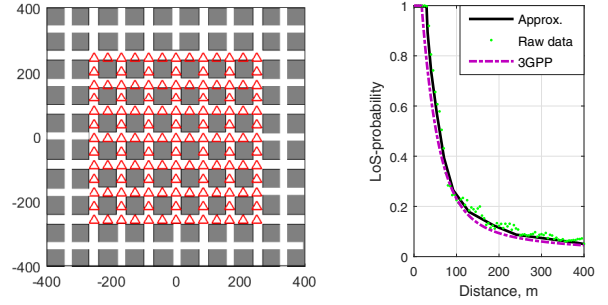


Fig. 1. Top view of the BS deployment (left) and calibration LoS-probability curves for our scenario (right). UEs are uniformly distributed across the area.

considered, which makes the total number of outdoor BSs to be 131. Similarly, we deploy the UE receivers (RXs) (their total number is 14500), where all of the indoor positions are disregarded as well. The number of outdoor RXs is hence 10500, while the distance between them is 5 m. Both the UE RX and the BS TX have 8x8 antenna arrays with double polarization, where additional details are offered in Section III. The remaining parameters are summarized in Table I.

TABLE I
CONSIDERED SCENARIO PARAMETERS

Parameter	Value
Total square, m	800 x 800
Propagation area, m	600 x 600
Building, m	60 x 60 x 100
Road width, m	20
Wall width, m	0.3
Wall material	concrete, $\epsilon = 5.03 - j0.31$ [17]
Selected ISDs, m	45, 90, 180, 360
Selected HPBW, °	13, 20, 50
UE and BS heights, m	1.5 and 10
Carrier frequency, GHz	28
Bandwidth, GHz	0.5
Noise figure, dB	7

Since radio interference is highly dependent on the ISD between the BSs as well as the half-power beamwidth (HPBW), different setups were considered in our simulations. To produce several distinct deployments with different densities of BSs, a dedicated function was implemented that decimates the rows and columns of the BS-grid. The mmWave carrier frequency utilized in all of our simulations is 28 GHz, which is envisioned for the initial 5G mmWave cellular deployments. The constructed scenario has also been cross-verified with the 3GPP reference data [16]. As an example, Fig. 1 (right) presents the line-of-sight (LoS) probabilities versus the distance to the BS for our deployment as compared to the reference data provided by 3GPP.

The commonly used performance metrics, such as signal-to-interference ratio (SIR) and signal-to-interference-plus-noise ratio (SINR) are considered in this work to demonstrate the effects of HPBW and density of mmWave BSs in terms of their impact on interference in urban deployments. Another question that has to be answered is that on the density of BSs and the value of HPBW, which make the mmWave system in question operate in interference- vs. noise-limited regime. The separation between these two modes is based on the parameter capturing the direct relationship between the interference and

noise powers – interference-to-noise ratio (INR). Convenient logarithmic scale helps differentiate between the two regimes as follows: $INR > 0$ dB indicates the interference-limited regime while $INR < 0$ dB corresponds to the noise-limited regime. In what follows, we focus on downlink operation.

III. PROPOSED EVALUATION METHODOLOGY

Generally, our methodology comprises two stages: purely deterministic ray-based modeling and post-processing on top of it to collect statistics. The first stage accurately calculates the channel properties between every TX-RX pair (TX element in the BS and RX element in the UE), while the second stage improves the results by adding a MAC abstraction and an antenna model. Such hybrid approach has a number of advantages, as compared to purely stochastic/empirical and deterministic models. First, it becomes possible to conduct a comprehensive analysis of a complex 3D deployment based on deterministic methods more efficiently. Some authors consider these tasks to be overly complex, or even impossible [18] for the purely deterministic tools. Second, in contrast to fast 2D ray-tracers [11] as well as empirical/stochastic models, our approach offers more accurate results for a specific deployment: for instance, it is feasible to accurately model the beamforming procedure when an antenna serves the selected UE.

A. Polarization-Related Considerations

Stochastic and empirical models used by 3GPP, for instance, consider polarization as well as the metrics associated with it as a stochastic process with log-normal distribution. Such an approach may not be accurate for site-specific modeling, where polarization-related parameters can be calculated deterministically. In electromagnetic analysis, the orientation of electric (E) and magnetic (H) field vectors defines the polarization of the radio wave. Generally, polarization of the propagating wave is not strictly important with respect to the propagation of radiation in free space without any specific antenna models.

However, when an electromagnetic wave interacts with the ground or the surrounding objects, the response of the surface material can be different for various orientations of the vectors. Hence, for an accurate analysis intended in this paper, the consideration of polarization is of crucial importance. Moreover, simulation of dual-polarized antennas (two orthogonal vectors shifting by $\pm 45^\circ$ to vertical orientation), which are not simply “horizontally” or “vertically” polarized, requires advanced polarization-specific considerations. Furthermore, incorrectly calculated polarization may lead to significant errors due to polarization mismatch. A general model utilized in this work represents an arbitrary oriented polarization as a sum of its horizontal and vertical components with respect to the interacting surface: $E = E_{e_{||}} + E_{e_{\perp}}$, where $e_{||}$ and e_{\perp} are the orthonormal basis. This representation remains fair for reflection and diffraction physics, where ray-fixed and edge-fixed coordinate systems are used respectively (see the following subsection).

When an electromagnetic wave arrives at the RX element, the polarization loss-factor (PLF) is modeled for calibration

purposes. It characterizes the cross-polarization losses between the wavefront and the RX element via an angle between these two vectors as $\cos(\alpha)^2$. When the angle is 90° , then the polarization mismatch tends to infinity, while 0° corresponds to the polarization matched case. The PLF as well as other typical wireless propagation metrics, such as cross polarization power ratio (XPR, from 3GPP specification [16]) and cross-polarized discrimination (XPD), have a similar nature and can be mapped onto each other through the components of E-field.

B. Ray-Based Modeler

In this research, we employed our in-house ray-based modeler [19], which is a comprehensive site-specific deterministic tool for signal propagation modeling. Generally, its structure includes two parts: a physical engine calculating the radio physics and a geometrical engine establishing the propagation paths between antennas. Asymptotic high-frequency techniques based on the Geometrical Optics (GO) and the Uniform Theory of Diffraction (UTD), which are an extension of the Geometrical Theory of Diffraction (GTD), form the basis of the physical engine in our tool.

According to these theories, for wavelengths much smaller than the dimensions of the objects ($10\lambda \leq \text{object size}$), it is possible to replace an electromagnetic wave with a line that connects the source of radiation and the receiving part [20]. Based on this premise, our geometrical engine conducts brute-force ray casting, which produces a visibility tree as well as conducts image-based ray-tracing, which calculates the paths between antennas with correct phases. Due to continuity and uniformity properties, a geodesic sphere was selected for the purposes of modeling, which produces near equidistantly positioned rays on its surfaces.

Input data for our ray-based modeler includes geometrical and physical properties of the scenario as well as the antennas. Output data from the ray-based simulation features radio channel properties in power, angular, and time domains per each TX-RX pair of elements. Our ray-based modeler supports a number of radio physics effects, which are central for the ray-based tools. The direct LoS connection between the TX-RX antenna elements separated by the distance of r corresponds to the free-space propagation, which is characterized by solving the Maxwell-Helmholtz equation:

$$E(r) = E_0 \frac{e^{-j\beta r}}{r}, \quad (1)$$

where β is the wave vector and E_0 is the initial E-field of antenna represented as follows:

$$E_0 = \sqrt{\frac{P_{TX} G_{TX} Z_0}{2\pi}}, \quad (2)$$

where P_{TX} is the radiated power in Watts, G_{TX} is the gain of the TX element, and Z_0 is the free-space impedance equal to 120π . At the initial stage, each TX element has $G_{TX} = 1$.

When the E-field E^i falls on a surface, it reflects E^r by losing some of its power. In the ray-based modeler, it is de-

scribed by a Fresnel coefficient for parallel and perpendicular orientations in relation to the plane [21]:

$$\begin{bmatrix} E_{||}^r \\ E_{\perp}^r \end{bmatrix} = \begin{bmatrix} R_{||}^{gen} & 0 \\ 0 & R_{\perp}^{gen} \end{bmatrix} \begin{bmatrix} E_{||}^i \\ E_{\perp}^i \end{bmatrix}, \quad (3)$$

where the generalized reflection coefficient for vertical and horizontal orientations relative to the plane is:

$$R_{\perp,||}^{gen} = R_{\perp,||} (1 - \frac{(1 - R_{\perp,||}^2) \exp(-2\alpha s) \exp(-2j\beta s) \exp(jkd \sin(\theta))}{1 - R_{\perp,||}^2 \exp(-2\alpha s) \exp(-2j\beta s) \exp(jkd \sin(\theta))}). \quad (4)$$

In (4), θ is the angle of incidence in relation to the plane's normal and ϵ is the dielectric permittivity of the material, while α and β are the lossy medium propagation coefficients, s is the distance traveled inside a wall, and d is the gap between two adjacent rays produced by the internal reflection.

When the wavefronts interact with the smaller elements of the environment, diffuse scattering and diffraction effects occur. In this paper, we assume that diffraction takes place if a ray hits the joint of two adjacent faces located in different planes when the angle between them is not 180° . Based on that, the diffracted field E_d is described by the dyadic diffraction coefficients D_{ss} , D_{sh} , D_{hs} , and D_{hh} as follows:

$$\begin{bmatrix} E_{\beta}^d \\ E_{\phi}^d \end{bmatrix} = \begin{bmatrix} D_{ss} & D_{sh} \\ D_{hs} & D_{hh} \end{bmatrix} \begin{bmatrix} E_{\beta}^i \\ E_{\phi}^i \end{bmatrix} \sqrt{\frac{r_{td} r_{dr}}{r_{td} + r_{dr}}} \frac{e^{-j\beta r_{dr}}}{r_{dr}}, \quad (5)$$

where r_{td} is the TX to diffraction point distance, r_{dr} is the diffraction point to RX distance, and β is the wave vector [22].

The power loss of the specular component due to scattering in surface roughness is modeled by the coefficient:

$$\rho = R_{\perp,||} \exp(-8\pi^2(\sigma/\lambda)^2 \cos(\theta)^2), \quad (6)$$

where $0 \leq \rho \leq 1$ and σ is the roughness coefficient. To reduce simulation time, more detailed model of diffuse scattering from [23] was omitted. This simplification affects the accuracy of our output results negligibly, since power contribution from the diffuse scattering per each pair of TX-RX is small.

C. Antenna Modeling

Broadly, an antenna model might be divided into three parts: antenna array geometry, pattern and polarization of a single element, and pre-calculated beamforming codebook. As mentioned previously, antenna geometry is based on 8×8 elements at both the BS and the UE sides with inter-element spacing of 0.5λ . The central point of the array is defined as the location point. In this paper, two types of antenna arrays were investigated (see [16], Sec. 7.3): dual-polarized and single-polarized. The single-polarized antenna has 8×8 elements with the vertically oriented (along Z-axis) polarization vectors, which might be changed (e.g., to horizontal) through rotation of the utilized transformation matrix. In contrast to the single-polarized antenna, the dual-polarized antenna is modeled as two co-located elements with biased polarization vectors.

The pattern for each of the single antenna elements was adopted from the 3GPP documents (see [16], Sec. 7.3),

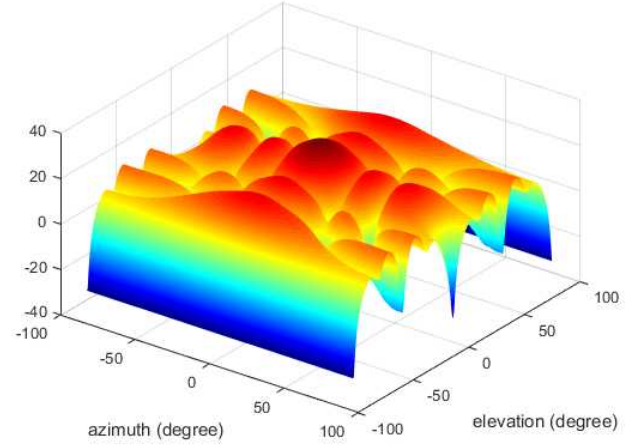


Fig. 2. Example of the pre-generated beam pattern.

while the realistic beamforming codebooks were generated beforehand (see example in Fig. 2). Three different codebooks were used in this paper for three different HPBW: (i) HPBW = 50° , 9 patterns; (ii) HPBW = 20° , 81 patterns; and (iii) HPBW = 13° , 169 patterns. The patterns were generated by taking into account mutually non-overlapping beams with a certain HPBW, which cover all of the directions in a spherical coordinate system.

Each single pattern is associated with a certain direction (azimuthal and elevation) that is represented by an array of weighted coefficients ϕ employed as the initial phases of the transmitted and received signal as $\exp(-j\phi)$. Based on the angular properties of dominant paths, appropriate patterns were selected and assigned to both the BS and the UE sides.

D. MIMO Channel Model

MIMO channel relies on the availability of multiple decorrelated RF-channels on the side of both the UE and the BS for the purposes of improving the channel diversity. In this work, we consider two antennas: single-polarized for calibration purposes and dual-polarized for main simulations. In case of two single-polarized 8×8 element antennas on the BS and the UE sides, 64×64 channels were produced:

$$\begin{bmatrix} x_1 \\ x_2 \\ x_3 \\ \vdots \\ x_{64} \end{bmatrix} = \begin{bmatrix} h_{1,1} & h_{1,2} & \cdots & h_{1,64} \\ h_{2,1} & h_{2,2} & \cdots & h_{2,64} \\ h_{3,1} & h_{3,2} & \cdots & h_{3,64} \\ \vdots & \vdots & \ddots & \vdots \\ h_{64,1} & h_{64,2} & \cdots & h_{64,64} \end{bmatrix} \times \begin{bmatrix} y_1 \\ y_2 \\ y_3 \\ \vdots \\ y_{64} \end{bmatrix}. \quad (7)$$

Since one dual-polarized antenna is represented as a combination of two collocated 8×8 arrays with mutually orthogonal vectors of polarization, the number of channels between a single UE and the BS increases as well:

$$\begin{bmatrix} x_1 \\ x_2 \\ x_3 \\ \vdots \\ x_{128} \end{bmatrix} = \begin{bmatrix} h_{1,1} & h_{1,2} & \cdots & h_{1,128} \\ h_{2,1} & h_{2,2} & \cdots & h_{2,128} \\ h_{3,1} & h_{3,2} & \cdots & h_{3,128} \\ \vdots & \vdots & \ddots & \vdots \\ h_{64,1} & h_{64,2} & \cdots & h_{128,128} \end{bmatrix} \times \begin{bmatrix} y_1 \\ y_2 \\ y_3 \\ \vdots \\ y_{128} \end{bmatrix}. \quad (8)$$

By default, our ray-based modeler can simulate MISO channels straightforwardly, which may take significant time when utilizing multiple antennas. As the number of TX antenna elements increases by N -times, the tool needs to calculate the channel just as often.

To mitigate this complexity, we simplify the modeling such that it would not require channel recalculation for each element of the antenna. Considering that most of the modeling time is spent on the geometrical considerations to find the path between each pair of TX and RX, we make the following assumption. Due to the fact that the size of the antenna array is much smaller than that of the script objects, the paths of all elements interact with the same elements of the scenario. In other words, by constructing the visibility tree for one transmit element, we can map it onto other elements within the same antenna as well. At the same time, the way points are kept unique for each TX-RX pair.

E. MAC Layer Abstraction

As soon as all the necessary channel information is collected between each isotropic TX-RX pair, the following stage begins. The main goal here is to calculate the interference metrics, such as the SIR and INR values, by using the detailed antenna models and MAC-abstraction represented e.g., by a Round-Robin scheduling algorithm. Prior to these operations, the beamforming codebooks are pre-calculated and stored for HPBW = 13°, 20°, and 50°. The weight phase coefficients are utilized further on to achieve the beam alignment between the BS and the UE. The post-processing phase starts by sorting: the BS having the dominant path (i.e., the highest power) to the UE with respect to other BSs is assumed to be the serving one. Using the path sorting procedure, for each of the BSs group of the relevant UEs is assigned. Fig. 3 demonstrates the links as a “star” topology between the BSs and their served UEs. In most cases, the distance is the measure that determines which of the BSs the user belongs to. On the other hand, there are cases when – due to certain physical phenomena (e.g., interference) – the UE can be served by a more remote BS.

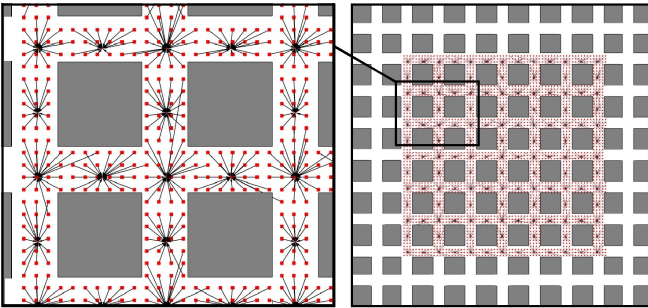


Fig. 3. UEs (red dots) collected in a group, each of which is served by a single BS. Such BS-UE links are represented as a “star” topology.

Finally, Round-Robin considerations are applied, which play the role of a MAC-abstraction in our simulations. From the stored list of UEs, each BS selects one and directs its main beam according to the departure angles (elevation and azimuth) from which the maximum receive power arrives.

IV. REPRESENTATIVE NUMERICAL RESULTS

A. LoS Calibration of Polarization Model

Before conducting our interference study, it is important to calibrate the antenna model, which is based on the classical Maxwell EM equations. A simple deployment was selected, where TX and RX antennas are aligned to each other in the LoS-conditions without any additional obstacles around them. Such alignment follows the equation (1). To verify the polarization modeling, the RX array was rotated with the step of 20° in relation to the TX antenna in the angular range of -90...90° (see Fig.4). In case of one TX and one RX dipoles, cross-polarization occurs when the relative angle is 90°, which corresponds to the theoretical model.

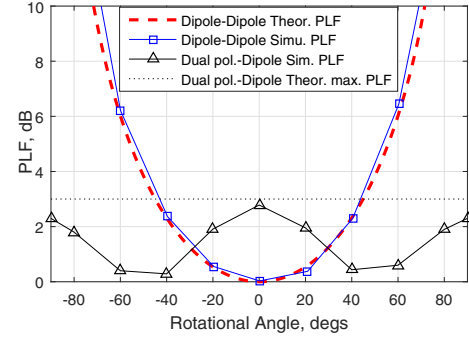


Fig. 4. Rotation of dual-polarized and single-polarized antennas relative to each other produces different magnitudes of polarization loss.

In case of utilizing dual-polarized antenna, two LoS-channels emerge: $TX-RX_{-45}$ and $TX-RX_{+45}$. Such complementary channels make the maximum PLF to be ≤ 3 dB, which also agrees with the theoretical value. Here, summation of the two received signals after RF processing makes the polarization loss to be negligible. When dual-polarized antennas are located on the TX and RX sides, four different channels can be observed. The availability of second TX channel increases the total received power on a single RX element by extra 3 dB.

B. Polarization Model Calibration in Manhattan Grid

As soon as LoS calibration between the antennas is completed, calibration in the Manhattan grid deployment becomes the next step. For this purpose, single-polarized (horizontal and vertical) antennas as well as dual-polarized antennas were utilized in our simulations. Output data from these simulations are represented by three different PLs: horizontally polarized PL (h-pol. PL), vertically polarized PL (v-pol. PL), and dual polarized PL (x-pol. PL). These three PLs should be considered separately, since the corresponding Fresnel coefficients (and their combination) are different.

To validate our preliminary expectations, Fig. 5 demonstrates log-approximated PL data. The difference between the h-pol. PL and the v-pol. PL is up to 12 dB, which is primarily caused by reflection losses. At the same time, being a combination of both v-pol and h-pol, x-pol PL is located in-between. Due to low polarization losses and possibility

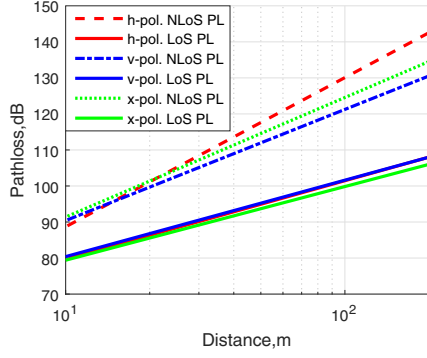


Fig. 5. Behavior of pathloss is different for vertical and horizontal polarization as well as for dual-polarized antenna.

to implement the polarization diversity for mmWave MIMO system, x-pol antenna has been selected and used in our further numerical evaluations.

C. Interference Analysis

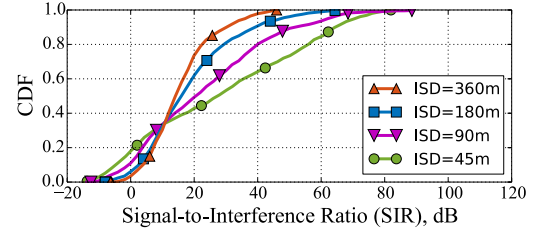
After the antenna model has been verified, further investigation of interference is conducted at different densities of BSs and for variable beamwidths. Particularly, we focus on the CDFs of SIR values in Fig. 6 and the mean values of SINR in Fig. 7. First, when the HPBW is 13° , the highest SIR and SINR values are observed with respect to the HPBW of 20° and 50° . Hence, narrower beams improve both SIR and SINR, since a lower fraction of interfering signals comes to the main beam of the target RX.

Second, there are two competing trends as the ISD begins to increase: the useful signal from the target BS becomes weaker (since the average distance to the BS grows), but also the density of interfering BSs decreases, thus the total power of the interfering components degrades. It has been shown in [4] that the first trend is stronger in free space, so the SIR and SINR values should degrade with the increase of ISD. Here, we can confirm this observation for a practical mmWave deployment in the Manhattan grid topology.

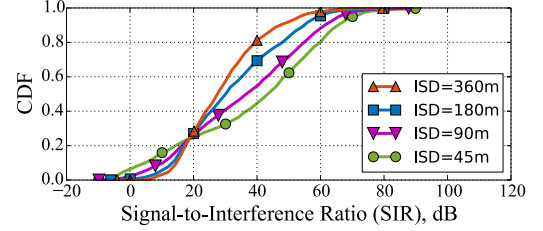
However, the decrease in question is not linear, since the difference between the SINR for HPBW = 13° , 45 m ISD and the SINR for HPBW = 13° , 360 m ISD is over 14 dB, while the same difference for HPBW = 20° is around 2 dB and less than 1 dB for HPBW = 50° . In other words, depending on the target HPBW value, the response of the mmWave system to densification is different, which suggests exploring the difference between the interference-limited and the noise-limited regimes.

D. Noise- vs. Interference-Limited Regimes

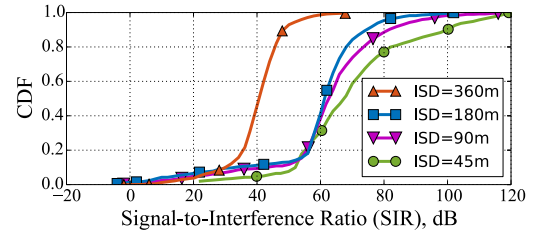
As mentioned above, there are two extreme regimes that the mmWave system may operate in: interference-limited and noise-limited. While the majority of past studies agree that an idealistic mmWave deployment (propagation in open space, narrow beams, perfect beam alignment, etc.) may operate in close to noise-limited regime, we have observed that the impact of interference may remain significant in certain cases.



(a) HPBW = 50°



(b) HPBW = 20°



(c) HPBW = 13°

Fig. 6. CDF of SIR for various densities of BSs and HPBWs.

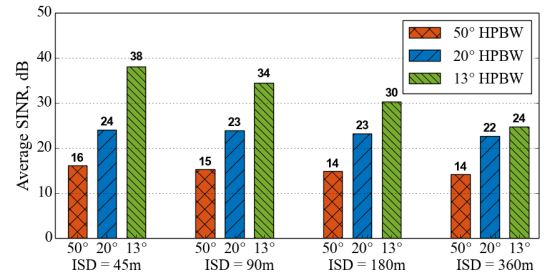
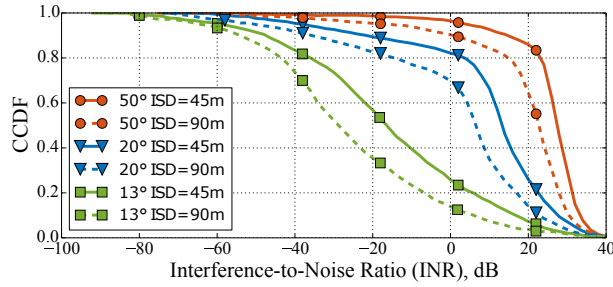
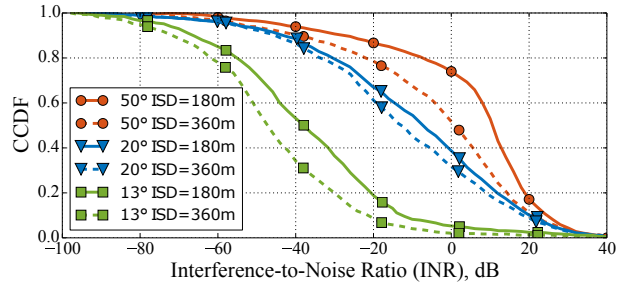


Fig. 7. Mean values of SINR for various densities of BSs and HPBWs.

We continue our numerical study by analyzing the scaling of the representative INR metric, which directly corresponds to the ratio between the levels of interference and noise in the considered system. Particularly, Fig. 8 demonstrates the complementary cumulative distribution function (CCDF) for the INR values in various deployment cases. Observing Fig. 8, we first notice that there are three deployments for which more than 80% of the RXs are in the noise-limited regime ($INR < 0$ dB): all with HPBW = 13° , but at different ISDs. At the same time, there are other three curves for which more than 80% of the RXs are in the interference-limited regime ($INR > 0$ dB), two of which with HPBW = 50° and ISDs equal to 45 m. Other deployments are in the intermediate regime, where neither noise nor interference dominate across all of the UEs.



(a) 45 m and 90 m ISD



(b) 180 m and 360 m ISD

Fig. 8. CCDF of INR for four densities of BSs and three HPBW.

V. CONCLUSIONS

In this paper, we studied the role of interference in the mmWave systems as a function of the deployment parameters, such as the inter-site distance between the base stations and the beamwidth of the antenna radiation pattern. For this matter, we developed a comprehensive ray-based modeling methodology that takes into account not only the geometrical and physical properties of the scenario, but also the specifics of the received mmWave signal impacted by realistic antenna polarization, practical antenna radiation patterns, as well as MIMO mmWave channel.

With our developed tool, we evaluated the impact of interference in various deployment configurations of the 28 GHz mmWave cellular system in the Manhattan grid topology, by obtaining the averages and the CDFs of SIR and INR values. We also illustrated how the clearly noise-limited operation with 360 m ISD and 13° beamwidth transitions into a distinct interference-limited regime with 45 m ISD and 50° beamwidth. These results may become a reference for future deployment optimization of mmWave cellular networks as well as for verification/calibration of more flexible (but typically less accurate, e.g., stochastic) mmWave interference models. At the same time, our systematically described evaluation methodology may be applied for site-specific studies of complex and practical mmWave scenarios.

ACKNOWLEDGEMENT

This work is supported by Intel Corporation as well as by the project TT5G: Transmission Technologies for 5G.

REFERENCES

- [1] S. Rangan, T. S. Rappaport, and E. Erkip, "Millimeter-wave cellular wireless networks: Potentials and challenges," *Proceedings of the IEEE*, vol. 102, pp. 366–385, March 2014.
- [2] M. N. Kulkarni, S. Singh, and J. G. Andrews, "Coverage and rate trends in dense urban mmWave cellular networks," in *Proc. of IEEE GLOBECOM*, December 2014.
- [3] K. Venugopal, M. C. Valenti, and R. W. Heath, "Device-to-Device millimeter wave communications: Interference, coverage, rate, and finite topologies," *IEEE Transactions on Wireless Communications*, vol. 15, pp. 6175–6188, September 2016.
- [4] V. Petrov, M. Komarov, D. Moltchanov, J. M. Jornet, and Y. Koucheryavy, "Interference and SINR in millimeter wave and terahertz communication systems with blocking and directional antennas," *IEEE Transactions on Wireless Communications*, vol. 16, pp. 1791–1808, March 2017.
- [5] J. G. Andrews, T. Bai, M. N. Kulkarni, A. Alkhatieb, A. K. Gupta, and R. W. Heath, "Modeling and analyzing millimeter wave cellular systems," *IEEE Transactions on Communications*, vol. 65, pp. 403–430, January 2017.
- [6] K. Venugopal, M. C. Valenti, and R. W. Heath, "Interference in finite-sized highly dense millimeter wave networks," in *Proc. of Information Theory and Applications Workshop (ITA)*, pp. 175–180, February 2015.
- [7] H. Elkotby and M. Vu, "A mixture model for NLOS mmWave interference distribution," in *Proc. of IEEE GLOBECOM*, December 2016.
- [8] H. Shokri-Ghadikolaei and C. Fischione, "Millimeter wave ad hoc networks: Noise-limited or interference-limited?," in *Proc. of IEEE Globecom Workshops*, December 2015.
- [9] M. Rebato, M. Mezzavilla, S. Rangan, F. Boccardi, and M. Zorzi, "Understanding noise and interference regimes in 5G millimeter-wave cellular networks," in *Proc. of European Wireless Conference*, May 2016.
- [10] S. Singh, R. Mudumbai, and U. Madhoo, "Interference analysis for highly directional 60-GHz mesh networks: The case for rethinking medium access control," *IEEE/ACM Transactions on Networking*, vol. 19, pp. 1513–1527, October 2011.
- [11] D. Steinmetzer, J. Classen, and M. Hollick, "mmTrace: Modeling millimeter-wave indoor propagation with image-based ray-tracing," in *Proc. of IEEE INFOCOM Workshops*, pp. 429–434, April 2016.
- [12] J. Song, J. Choi, S. G. Larew, D. J. Love, T. A. Thomas, and A. A. Ghosh, "Adaptive millimeter wave beam alignment for dual-polarized MIMO systems," *IEEE Transactions on Wireless Communications*, vol. 14, pp. 6283–6296, November 2015.
- [13] U. Schmid, D. Lin, and W. Menzel, "A novel dual polarization antenna array fed by a dual mode non-radiative dielectric waveguide," in *IEEE/MTT-S International Microwave Symposium Digest*, pp. 1–3, June 2012.
- [14] J. Wu, S. Yang, Y. Chen, S. Qu, and Z. Nie, "A low profile dual-polarized wideband omnidirectional antenna based on AMC reflector," *IEEE Transactions on Antennas and Propagation*, vol. 65, pp. 368–374, January 2017.
- [15] "METIS channel models," Tech. Rep. ICT-317669-METIS/D1.4, METIS, February 2015.
- [16] 3GPP, "Channel model for frequency spectrum above 6 GHz (Release 14)," 3GPP TR 38.900 V2.0.0, 2016.
- [17] "Effects of building materials and structures on radiowave propagation above about 100 MHz," *ITU-R P.2040-1*, July 2015.
- [18] F. Baccelli and B. Błaszczyszyn, *Electromagnetics of Body Area Networks: Antennas, Propagation, and RF Systems*. Wiley, 2016.
- [19] V. Petrov, D. Solomitckii, A. Samuylov, M. A. Lema, M. Gapeyenko, D. Moltchanov, S. Andreev, V. Naumov, K. Samouylov, M. Dohler, and Y. Koucheryavy, "Dynamic multi-connectivity performance in ultra-dense urban mmwave deployments," *IEEE Journal on Selected Areas in Communications*, vol. 35, pp. 2038–2055, September 2017.
- [20] H. Singh and R. M. Jha, *Active Radar Cross Section Reduction*. Cambridge University Press, 2015.
- [21] L. M. Correia and P. O. Frances, "Estimation of materials characteristics from power measurements at 60 GHz," in *Proc. of IEEE PIMRC*, September 1994.
- [22] P. D. Holm, "A new heuristic UTD diffraction coefficient for non-perfectly conducting wedges," *IEEE Transactions on Antennas and Propagation*, vol. 48, pp. 1211–1219, August 2000.
- [23] V. Degli-Esposti, D. Guiducci, A. de'Marsi, P. Azzi, and F. Fuschini, "An advanced field prediction model including diffuse scattering," *IEEE Transactions on Antennas and Propagation*, vol. 52, pp. 1717–1728, July 2004.

PUBLICATION

V

**Technologies for efficient amateur drone detection in 5G millimeter-wave
cellular infrastructure**

D. Solomitckii, M. Gapeyenko, V. Semkin, S. Andreev and Y. Koucheryavy

IEEE Communications Magazine 56.1 (2018), 43–50

DOI: 10.1109/MCOM.2017.1700450

Publication reprinted with the permission of the copyright holders

Technologies for Efficient Amateur Drone Detection in 5G Millimeter-Wave Cellular Infrastructure

Dmitrii Solomitckii, Margarita Gapeyenko, Vasilii Semkin, Sergey Andreev, and Yevgeni Koucheryavy

Abstract—Unmanned aerial vehicles also named drones are recently gaining increased research attention across various fields due to their flexibility and application potential. Steady increase in the number of amateur drones demands more stringent regulations on their allowed route, mass, and load. However, these regulations may be violated accidentally or deliberately. In these cases, spying with drones, transfer of dangerous payloads, or losing reliable drone control can represent a new hazard for people, governments, and business sector. The technologies to detect, track, and disarm possible aerial threat are, therefore, in prompt demand. To this end, ubiquitous cellular networks, and especially fifth-generation (5G) infrastructures based on the use of millimeter-wave radio modules, may be efficiently leveraged to offer the much needed drone detection capabilities. In this work, we propose to exploit the 5G millimeter-wave deployment to detect the violating amateur drones. We argue that the prospective 5G infrastructure may provide with all the necessary technology elements to support efficient detection of small-sized drones. We, therefore, outline a novel technology and system design perspective, including such considerations as the density of base stations, their directional antennas, and the available bandwidth, among others, as well as characterize their impact with our ray-based modeling methods.

I. DETECTION OF UAV WITH 5G INFRASTRUCTURE

A. Advent of amateur drones

Initially exploited by the military, unmanned aerial vehicles (UAVs) are currently gaining increased interest from civilian users because of rapid development in electronics. A flying device without a human pilot on board, UAV or simply a drone is a flexible solution suitable for a broad range of applications, such as goods delivery, video monitoring, and aerial mapping, among many others. In fact, drones become so popular that Federal Aviation Administrations (FAA) in the US demanded mandatory registration for new drones as well as restricted any commercial use of them until thorough regulations are issued. It was estimated that by 2018 the number of commercial drones in the air will reach about 600,000 [1].

Today, the research and industry communities are working intensively to facilitate more reliable and flexible drone utilization. A number of technical issues, such as collision avoidance, battery life optimization, reliable connectivity with fixed ground infrastructure (backhaul), and safe take-off and landing, are yet to be solved and thus slow down the mass employment of drones [2], [3]. However, we are approaching the time when the remaining challenges are solved and the fleets of drones will be flying around the city. The use of

UAVs might introduce impressive benefits, but there are also some pitfalls related to their flexibility and the absence of a pilot. Along with responsible drone operators abiding by the regulations, there may be other ones offending against law accidentally or intentionally.

The first type of possible violations includes, for example, anti-social and terrorist acts, while the second type can be attributed to non-acquaintance of regulatory laws. The latter also includes the cases where a partially out-of-order drone behaves unpredictably due to spatial disorientation; so any drone acting in a dangerous, unpredictable, improper, or unsafe manner towards other drones, infrastructure, or humans, is to be considered an air traffic law violator. Therefore, it is extremely important to be prepared for any inconvenience caused by violating the rules for usage of drones. Undoubtedly, early detection of violating drones is among the key elements of aerial accident prevention.

In the scope of this work, we focus on *fast detection* of amateur drones (ADr) that might be launched from the ground close to drone-free regions of an urban scenario. In particular, we assume that ADr might belong to any organization (including illegal, non-certified and, in the extreme, terrorist) or any private operator and carry arbitrary payload, including chemical and explosive substances, as well as various on-board equipment. It might also not carry any on-board systems at all, thus preventing communication and control takeover by a third-party neutralization system. The problem statement is then more complicated, since the ADr is a potential source of the highest level of threat for other drones as well as national institutions and assets, and it should be neutralized as fast as possible.

B. UAV in next-generation cellular

Approaching their initial test deployments, the fifth generation of wireless networks, 5G, is planned to be initially tested in 2018, Seoul, Korea. As 5G broadly represents an umbrella for various technology types, there is room for drones in the future 5G scenarios [4]. According to the latest use case descriptions, drones can be utilized to extend network coverage in highly crowded areas as well as provide emergency coverage in situations of local infrastructure malfunction or disaster. Despite intensifying discussions on applying UAVs to extend radio coverage in future wireless systems, integration of drones into current network infrastructure and human environment still remains an open issue. The important problems of controlling, detecting, tracking, mitigating interference, and optimizing radio resource management [5] need to be resolved before the fleets of drones can fly around freely.

D. Solomitckii, M. Gapeyenko, S. Andreev, and Y. Koucheryavy are with Tampere University of Technology, Tampere, Finland
V. Semkin is with Aalto University, Espoo, Finland

Employing the so-called millimeter wave (mmWave) frequency bands, 5G cellular promises to unlock unprecedented available bandwidths, allowing to support such advanced and throughput-hungry multimedia applications as augmented reality and unmanned vehicle control. However, it has to be noted that due to specifics of the mmWave bands the 5G may not be able to rely on it entirely, thus conventional microwave (uWave) frequencies and related wireless standards will also remain a part of 5G technology [6]. As a result, 5G mmWave base stations (BSs) will soon be integrated into the traditional cellular infrastructure. Having in mind the unique capabilities of 5G, especially the increased bandwidth, we propose to employ some of the spare mmWave capacity to provide means for safe drone interaction with the human environment.

Particularly high frequencies at mmWave bands allow for improved detection of objects, thus effectively serving as a radar. Moreover, the anticipated densification of mmWave BSs, which is important to provide session continuity and improved capacity, should ensure more reliable drone detection as well. We reiterate an important fact that the time to react before potential damage is always limited; hence, fast and reliable detection of violating drones is of extreme importance. Therefore, in this work, we envisage a novel system for early detection of violating drones by employing the powerful 5G mmWave capabilities.

II. CHALLENGES POSED BY UNAUTHORIZED DRONES

As soon as all the necessary regulations are in place and substantial UAV traffic is permitted in the human environment, the question of public safety is due to become crucial. Every functionality of drones aimed to aid people, such as video monitoring or cargo delivery, could then be potentially misused. For instance, drones carrying cameras already violate privacy by monitoring humans without any permission. Further, cargo delivery could pose a major threat in case the payload turns out to be harmful. Therefore, a number of challenges arise that should be considered before an ultimate permit for ADr to operate freely is issued. We distinguish four principal challenges related to the flight of an unauthorized drone, namely: detection, localization, tracking, and deactivation.

Even though every aspect in the above vision has importance and should be considered carefully, the primary challenge is fast *detection*, which becomes the focus of this work. Indeed, before a violating drone is detected it cannot be disarmed. For that purpose, single or multiple distributed detecting sensors [7] need to observe the flight of drones in real time. In addition, all these sensing nodes require an adequate cooperative algorithm for timely detection and identification of UAVs. Another problem to be solved is the *localization* of a drone. Being a highly mobile aerial node, a drone can easily disappear from sight. Hence, precise localization of drones needs to be made available to the authority responsible for drone surveillance and recent research pays particular attention to the drone localization techniques. Conventional methods employ mobile wireless sensor networks, but existing approaches are not fully suitable for accurate drone positioning because of the unique properties of the UAVs.

Alongside with localization, drone *tracking* is another emerging issue due to highly unpredictable 3D mobility patterns of drones. The goal here is to predict further behavior of the UAV by employing tracking algorithms. Since the countermeasures to prevent the violation caused by a drone cannot be taken immediately, the subject drone should be tracked until it is disarmed. Subsequently, tracking is of special importance in order not to lose the drone from sight. The last but not least challenge is drone *deactivation*. It could involve such methods as drone jamming, hunting, etc. To date, numerous techniques for prevention of drone-inflicted damage have been proposed; however, in the worst case, drone deactivation can become a major issue on its own and inflict further damage to the human environment. It is extremely important to react promptly before any such damage is caused; thus, this challenge has to be solved with a proper, time-efficient and safe method.

In this article, we concentrate on techniques for ADr detection in urban environments. To this end, below we review the key technologies and offer examples based on existing equipment. It should be noted that almost all of these techniques were initially tested or adopted for military purposes, and now they are gradually propagating into civilian applications. For that reason, in the commercial market it is already possible to purchase such equipment with reduced (although not fully removed) restrictions on International Traffic in Arms Regulations (ITAR).

III. PRINCIPLES OF 5G DRONE DETECTION SYSTEM

Inspired by the promising 5G capabilities, we envisage that 5G mmWave infrastructures will be capable of supporting two functional modes: provisioning of communication services as well as detection of violating ADr based on multistatic radar techniques [8]. Indeed, as illustrated in Fig. 1, the detection system may partially reuse the elements of 5G mmWave infrastructure. At the same time, the level of sharing the 5G resources may depend on the capabilities of the network and wireless equipment, and not be restricted to the use of mmWave BSs. Based on flexible modular design, our proposed architecture offers versatile utilization and is ready to be adopted for novel communication and detection challenges by replacing certain elements of the system.

In our proposed architecture, multistatic radar transmitting (Tx) system generates a wideband signal into the upper hemisphere. The signal propagating in the site-specific area experiences intermediate interaction with the objects and reaches the receiving systems on multiple paths (named multipath propagation). In Fig. 1, a multistatic radar receiving (Rx) system is represented by a number $(1, 2, \dots, N)$ of different mmWave BSs, each collecting its unique portion of the multipath components of the transmitted signal. It has to be emphasized that both Tx and Rx systems are located at some distance from each other. To synchronize cooperative operation of the Tx and Rx in the radar mode, a multiplexer triggers up single mmWave BS or groups of them, as soon as the Tx begins to radiate signal into space. Additionally, it may (de)activate a mmWave BS for smarter detection, in case one of them is blocked by an object or sends incorrect output data.

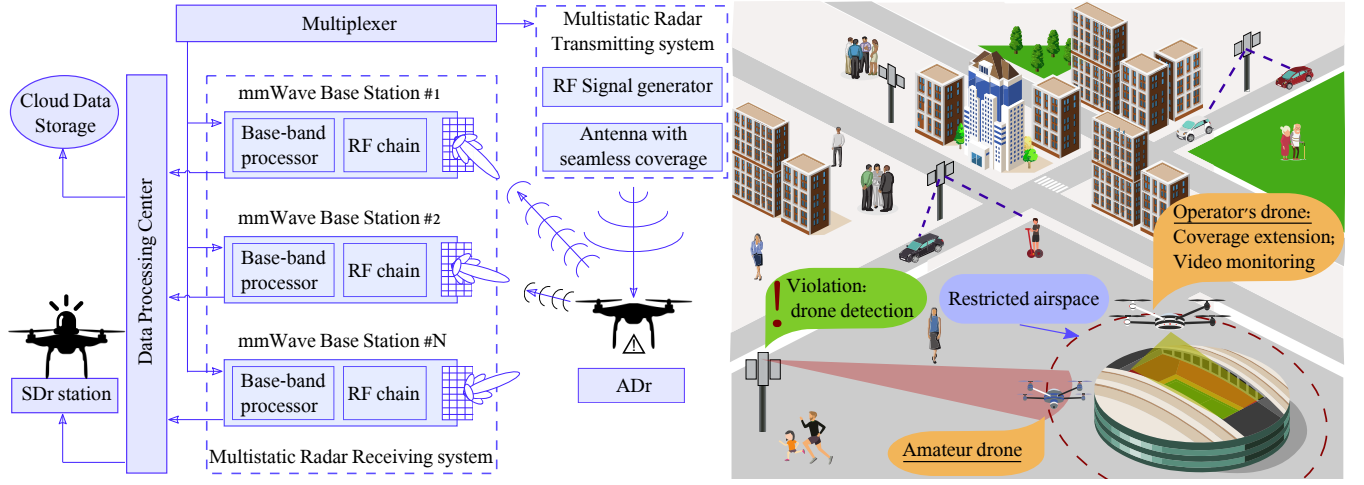


Fig. 1. Proposed 5G-based system architecture for detecting amateur drones (left) and envisioned motivating scenario (right).

Collecting and processing the output data from all (or some) of the mmWave BSs, Data Processing Center (DPC) controls the overall management of the radar system and predicts further actions. It may initiate an additional detection procedure to verify the current results, compare the collected information with the reference data patterns in Cloud Data Storage (CDS), or summon surveillance drones (SDr) to neutralize an intruder. Depending on the amount and the quality of received data, the DPC might detect and potentially recognize the type of the ADr as well as determine its intentions by comparing the collected information against past data stored in CDS. The DPC may also assign the level of threat to one or several detected drones by taking into account multiple probabilistic criteria assessed on-line.

IV. ENABLING TECHNOLOGIES FOR DETECTING DRONES

This section discusses the necessary technology features to implement our target 5G-based ADr detection system.

A. Use of mmWave bands

Frequency band. According to current technology development plans, 5G will incorporate the previous generations of wireless solutions (3G and 4G) as well as introduce the new promising mmWave technology. Hence, there is a choice between two potential carrier frequencies for the intended radar application: uWave and mmWave bands. Owing to the shorter wavelengths of mmWave carrier, small objects in the propagation environment are almost invisible at uWave while remain visible (electrically large) in mmWave. It is, however, clear that the type of roughness and irregularities of reflecting surfaces becomes more significant in mmWave bands, whereas these effects are minor in uWave [9]. Such behavior offers an advantage for usage of mmWave frequencies in detecting miniature drones sized within a range of 0.2 – 1.0 m, which is typical for ADr.

To assess the detection capabilities of uWave and mmWave bands, we employ detailed modeling of radar cross-section (RCS), which demonstrates how an object scatters the incident electromagnetic radiation back to the Tx position [10].

Together with uWave and mmWave bands, two different geometric radii were considered: 0.4 m and 1.5 m. As observed in Fig. 2, the capability to detect small objects is x1000 times (30 dB) higher at mmWave (60 GHz) with respect to that at uWave (2 GHz) if the angle of incidence equals to 0° .

These results confirm a crucial advantage of mmWave in comparison to uWave for ADr detection. The RCS behavior in Fig. 2 can be explained by undermining of the reflected component, which is strong enough due to diffuse scattering and diffraction. Related to the unique properties of an object, the RCS is a base parameter that might be utilized as a measure to distinguish “drone” and “another drone” as well as “drone” and “not a drone”.

Bandwidth. Future 5G mmWave systems will not only support extremely high carrier frequencies but also effectively operate in wider bandwidths (up to 2 GHz). Wider bandwidth helps differentiate between the closely flying ADr more accurately, since the pulses of shorter duration do not overlap each other at the receiver. The potential range resolution cell

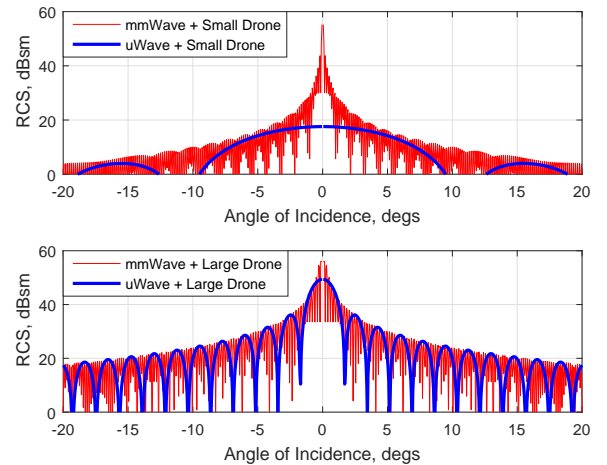


Fig. 2. Reflection from small and large drones in uWave (bottom image) and mmWave (top image).

of a radar system can be calculated as:

$$\Delta C = c/2B, \quad (1)$$

where ΔC is the range resolution, c is the speed of light, and B is the system bandwidth. Using this equation [10], it is possible to demonstrate that a system having 200 MHz of bandwidth (typical for uWave cellular technology) achieves the range resolution of 0.75 m, while 2-GHz bandwidth in mmWave gives us x10 higher precision (0.075 m).

B. Composition of receiving system

MIMO system. Multiple co-located decorrelated antennas on the Tx and Rx sides establish an efficient multi-input multi-output (MIMO) system that looks promising for future 5G communication. It creates additional channel diversity for the multistatic scheme and improves throughput via simultaneous transmission of multiple streams over different spatial channels. Subsequently, a multi-element antenna increases the effective bandwidth of the wireless channel. The receiving MIMO antenna array in mmWave BSs can also be reused for the purposes of multistatic radar functionality to receive the transmitted signal [11].

The MIMO radar system with co-located antennas can achieve higher spatial resolution and provide substantially improved immunity to interference as compared to the conventional technologies, such as phased arrays, where elements are fed by one RF chain. Utilization of all these advantages leads to unprecedented target detection levels, improves parameter estimation, as well as enhances tracking and recognition capabilities. Tentative results obtained with our custom-built ray-based modeler (Table I) demonstrate that utilization of MIMO functionality in mmWave BSs for radar applications improves detection probability in relation to single-input single-output (SISO) systems. The performance data has been collected for a single mmWave BS of interest when a number of scatterers and interfering transmitters around the target mmWave BS is generated randomly, with a certain characteristic density. When the level of interference caused by the scatterers and antennas is equal to or higher than the useful signal from the ADR, detection fails.

TABLE I
ADR DETECTION PROBABILITY USING MIMO AND SISO

#	System	Density of scatterers, m^{-2}	# of interfered BSs	Detection probability
1	SISO	0.05	1	0.59
2	SISO	0.25	3	0.35
3	MIMO	0.05	1	0.82
4	MIMO	0.25	3	0.71

Beamforming. Adjusting the phases and magnitudes of a signal coming to each element of the antenna array allows for producing different types of beam shapes. Two principal blocks are required to implement beamforming: an RF chain for controlling the phases and amplitudes and a baseband processor for handling the signals (see Fig. 1). Three conventional beamforming techniques are known today, namely: analog,

digital, and hybrid [12]. The first architecture is built upon a single RF chain that controls multiple phase shifters feeding an antenna array. Despite the fact that analog beamforming is the most limited option, it also remains the cheapest and least complex technique [12], which is successfully exploited in indoor mmWave technology, including IEEE 802.11ad.

Another architecture is based on digital beamforming, which may potentially support as many RF chains as there are antenna elements. Applying suitable precoding yields higher algorithmic flexibility and may lead to better performance as compared to other beamforming architectures [12]. For example, multi-user coverage supported by the digital beamforming plays a crucial role in promoting the beamforming technology to become the best candidate for intended radar applications. However, higher complexity and stringent hardware requirements increase the total costs and energy expenditures, thus limiting the use of fully digital beamforming to high-end 5G BSs.

Combining the advantages of both analog and digital beamforming architectures [12], hybrid beamforming is also becoming available. Since the number of converters is significantly lower than the number of antennas, there are fewer degrees of freedom for the digital baseband processing. Therefore, the utilization of hybrid and analog beamforming architectures for the combined communication and radar applications remains questionable and requires further research.

Beamsteering. Since 5G mmWave communication is intended to support dynamic deployments, static beamforming may not offer sufficient reliability, as it cannot direct the main beam to the served user. To solve this problem, a beamsteering procedure can be applied in order to adjust the phases and magnitudes in real-time as well as keep the main beam directed at the served user. Once the system is equipped with a beamsteering technique for communication purposes, it becomes possible to achieve some benefits for the radar applications as well. In this case, due to the utilization of directive antennas, the beamsteering procedure may assist in detection of a violating drone through fast scanning.

Using a predefined number of phases per each antenna element, the scanning process allows to extend the beamspace for drone detection in a hemisphere. The localization can also be performed easily as soon as the violating drone is found with a scanning procedure. When such a drone is detected and localized, a tracking procedure is triggered in order to identify its parameters and intentions. This consecutive approach reduces the chances of false assessment of the threat, but it also requires more radio resources and smarter algorithms that may be more difficult to implement in relatively simple BSs.

C. Composition of transmitting system

Generally, the Tx system can comprise two main blocks: an RF generator and an antenna; the latter begins to radiate a signal upon being triggered by a multiplexer. The key technical requirements applied to the transmitting system are high power density and a pattern directed to the upper hemisphere. The first criterion is crucial since it characterizes the detection performance of the entire system, but remains limited by radio

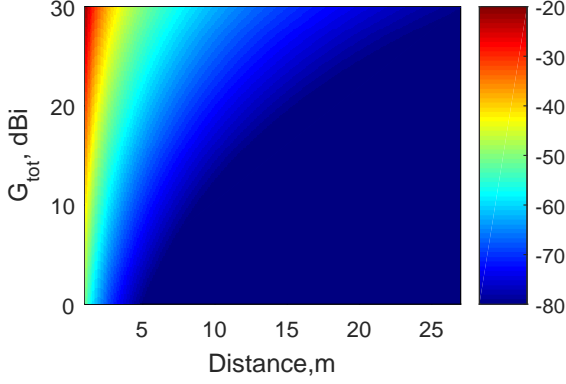


Fig. 3. Received power (color bar on the right) vs. distance and total gain. Dark blue region is the noise level equal to -80 dBm.

frequency regulations in all countries. The importance of the second criterion is in achieving uniform coverage across an area, where an ADr might potentially be detected.

To keep human safety at high levels, the antenna of the Tx system must be installed at the heights of at least 2 m. Recall that the electromagnetic mmWave field attenuates strongly when passing through concrete and brick walls (20 – 40 dB), and thus should not impact the health of humans inside buildings when keeping the power density below the level of 5 mW/cm² [13]. Based on these requirements, a simple and robust candidate for the antenna of the Tx system is a vertical dipole array.

To establish sufficient magnitude of the Tx system gain, it is important to first estimate the link budget. Here, the radar equation may be considered as a function of the distance and the total Tx and Rx gain $G_{tot} = G_{tx}G_{rx}$ as:

$$P_r(d, G_t) = \frac{P_t G_{tot} \lambda^2 \sigma}{(4\pi)^3 d^4}, \quad (2)$$

where P_t is the transmit power, λ is the wavelength, d is the distance to the drone, and σ is the RCS. The noise floor level for the considered 28-GHz carrier is set to 80 dBm by taking into account the $BW = 0.5$ GHz and the noise figure of 7 dB.

In light of the above and based on Fig. 3, the following important observations can be made. First, antenna gain in a radar system significantly improves the detection capabilities, even though the total received power reduces according to d^{-4} – faster than the total gain may compensate for it, since $G_{tx}G_{rx}$. Second, assuming practical magnitude gains of the antenna at the BS side as equal to 20-22 dBi, the antenna at the Tx side should have at least 8-10 dBi of gain (see Fig. 3), which is absolutely feasible to guarantee the detection range of up to 20 m.

D. DPC, controller, and CDS functionality

The main objective of the DPC in our architecture is to collect information from the mmWave BSs and process it at a later time. Data processing algorithms should employ not only standard formulations of signal processing but also specific machine learning techniques as discussed below.

The basic information provided to the DPC by each of the mmWave BSs is the shape of band-limited time-variant channel impulse response (CIR). When the space is free from drones, the properties of CIR do not change significantly, since most of the moving vehicles and humans are located in the bottom area (near ground). A flying drone reflects the transmitted signals thus producing additional taps that are visible in CIR of several mmWave BSs. Such cases have to be recognized by the DPC with high levels of reliability.

Machine-learning procedures are important here, since the surrounding environment is changing continuously, by potentially causing perturbations in CIR. Hence, all the biases have to be accurately examined by a comparison procedure that employs reference data patterns stored in the CDS. Taking into account the object specifics, the DPC should understand that some objects do not pose any threat and do not have to be neutralized. The result of machine learning operation aims to help interpret the data and can be used for forecasting, diagnostics, control, and validation purposes [14].

To further make the operation of Tx and Rx more intelligent, some of the antennas might be (de)activated or adjusted for the task at hand. A corresponding joint operation algorithm may reside in the DPC; however, its specific realization is heavily controller-dependent. The controller – empowered with enhanced hardware periphery – is able to mutually synchronize antennas by following the said algorithm.

To maximize the probability of drone detection as well as identification, the CDS is used. This cloud-based data storage controls an extensive amount of classified drone-specific data patterns; this reference data is then used by the DPC for the purposes of comparison. However, conventional approaches in data analysis may no longer be sufficient, and new methods for efficient analysis are required. Therefore, new interdisciplinary math techniques need to be developed, which encompass statistics, pattern recognition, and machine learning to support the analysis of data and discovery of principles hidden within this data.

E. Densification of Tx and Rx systems

Successful ADr detection is directly and strongly connected to the density of elements in the Tx and Rx system deployments: higher density generally increases the detection probability. Depending on the type of drones, their dimensions, as well as the presence or absence of payload, the scattered signal may propagate in unpredictable directions.

Produced with our ray-based modeling tool, Fig. 4 demonstrates the reflection capability of a relatively small unloaded drone (left side) and a relatively large drone carrying a square box located in its bottom part (right side). In the course of the simulations, accurate 3D CAD models of drones interacted with a single transmitter operating at 28 GHz central frequency and having 0.5 MHz of bandwidth, while multiple (about 1,000) receivers distributed in the X-Y plane collected the reflected/diffracted/scattered electromagnetic field. The displayed image was obtained via the inverse Fourier transform of the said field and has a direct relation to the RCS. The reflected power is represented by a color bar, where red color

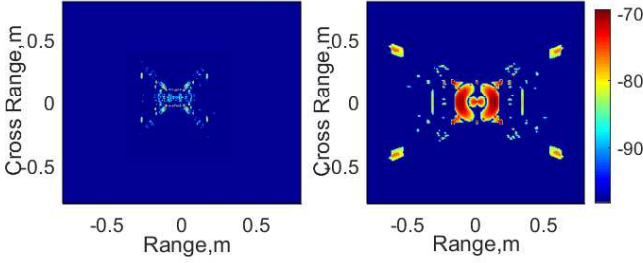


Fig. 4. Reflection capability of a small unloaded drone (left side) and a large drone carrying a box (right side).

corresponds to higher power (scattering centers) and blue color indicates lower power. As one can observe, the right plot has more red-colored areas, which highlight the scattering centers with higher power.

Accordingly, if the directions of the reflected signal are not aligned with the position of the receiving mmWave BSs, this signal may not be detected. Such areas can be observed as blue regions in Fig. 4, e.g., at the coordinates [0 0.2] in the left image and [0 0.5] in the right image. The above mentioned approach is typical for radar application and might be applied for processing of a reflection patterns. The methodology may also be extended for estimation of drone detection probability in urban deployment by adding to simulation elements of architecture (such as buildings), antenna models with properties similar to those obtained in Sec. IV C and adopted physical/postprocessing parts. In the frame of the simulation fixed number of Tx sources and varying density of mmWave BSs for different drone sizes (see Fig. 5) is considered. For each considered density of the BSs, we model up to 100 locations of the drone as well as assess the number of receivers that have acquired the scattered signal above the noise level. To this aim, Fig. 5 reports on the average number of such receivers, which have successfully detected the signal.

In summary, 5G mmWave networks become an attractive candidate technology for the intended radar system implementation, as shrinking the coverage area and densifying the BS deployment are their key inherent properties. Integrating the proposed radar functionality as described above makes

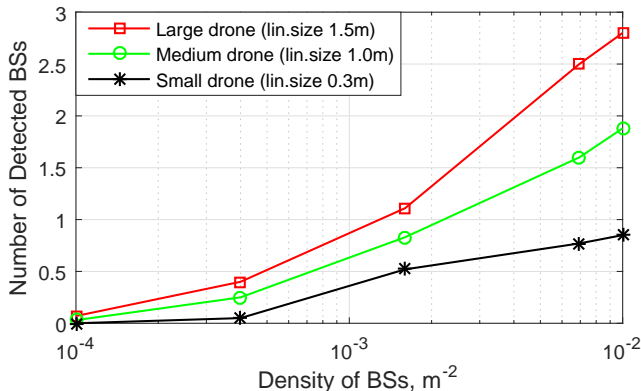


Fig. 5. Detection levels for ADr of different sizes by 5G mmWave BSs.

drone detection more reliable and turns the 5G system into a distributed monitoring network. If required, such distributed network may additionally recognize the type of the flying object, thus reducing the probability of failure. To achieve this, it is required to take into account the RCS samples of Rx (see Fig. 5) and compare those with the data stored in the CDS. Whenever densification with the BSs is not sufficient to achieve reliable ADr detection or pathloss between the antennas remains large, additional transmitting antennas may be installed. However, such situations are unlikely as future networks move toward ultra-dense deployments.

V. FUTURE CHALLENGES AND OPEN ISSUES

Integration of radar functionality into 5G infrastructure gives rise to important further challenges and open research directions, which we outline in this section.

Resource management related aspects. Since radio resources of mmWave BSs remain limited, distributing these resources between communication and radar functionalities while maintaining the quality of operation for both modes on the required level becomes a highly convoluted issue. A potential solution to improve the spectrum sharing efficiency is to employ cognitive radio techniques [15]. Generally, resource management might be addressed at hardware, PHY, and MAC layers. A number of corresponding problems need to be investigated, e.g., defining the minimum technical requirements on the mmWave BS exploited as a receiving element of the multistatic radar system. Accordingly, we distinguish the cases when the system (i) supports switching between radar and communication modes and (ii) supports simultaneous operation of radar and communication modes. Detailed consideration of these cases calls for development of new algorithms for resource allocation and sharing across the two operating modes.

NLoS radar operation. As mentioned above, dense deployment of mmWave BSs is required for both the communication and radar modes. However, some of the BSs might be deactivated for certain reasons, which in turn reduces the levels of drone detection reliability. In addition, because of urban scenario specifics, the nearest BSs may be located in the non-line-of-sight (NLoS) conditions with respect to the deactivated BS(s). To maintain the detection probability reasonably high, the NLoS BSs may also participate in the considered detection procedure.

Noise mitigation techniques. Today, conventional urban deployments are not typical for radar applications, which are primarily optimized to operate in open-space regions. Urban scenarios have a considerable number of noise sources, which may lead to faulty detection. This negative effect can be mitigated by utilizing advanced machine learning algorithms for recognizing and classifying the noise sources together with their location, based on the antenna directivity. Further, such data may be taken into account when the drone detection procedure is triggered.

Scanning procedure considerations. The procedure of scanning the upper hemisphere is central for the described system, since it provides information on the ADr location.

However, properties of the corresponding steering mechanism may raise further questions, such as the optimal selection of the interference beam steering regime in terms of the core radar metrics. In addition, being a source of considerable disruption, background noise impacts the detection capabilities during the beam movement; the means for reducing this negative effect require further research.

Big data management. More investigation might also be demanded by multi-step detection techniques that employ complementary detection technologies to verify the radar data and reduce the false detection probability. These technologies include infrared and visible detectors, acoustic arrays, time-of-flight equipment, and electromagnetic detectors. Employing information from multiple BSs as well as such complementary sensors, leads to a challenge of big data management. Despite the fact that the described task is novel in this context, in the last decade computers have provided with inexpensive capabilities to collect and store big data.

Network planning aspects. It is well known that network planning is central to achieve high-quality communication. The same holds true for built-in radar systems, which should also be deployed by taking into account a number of parameters. The planning tasks may include evaluation of the minimum number of mmWave BSs required in a given locality to ensure the detection of drones of a particular size with a certain probability. Further, increasing the quality of detectable data might be necessary to improve the drone recognition properties. Hence, the problem of determining the type of a drone arises based on the scattering properties. Finally, since the transmitting system may be omnidirectional, the challenge of interference mitigation despite the densification of mmWave BSs may play an important role.

VI. MAIN CONCLUSIONS

Utilization of 5G mmWave BSs as radars for detecting unauthorized drones is a new direction in research. By employing our in-house ray based modeler as well as building on several theories, we contributed our vision of the corresponding system design with the drone detection capability that relies on 5G mmWave infrastructure. In particular, we observed that the high bandwidth (up to 2 GHz) of mmWave band offers a number of benefits for early detection of rule-violating ADr. This is because we expect that small-sized drones will prevail as the main violators of air traffic rules in urban scenarios as well as may serve as instruments of unlawful acts from the side of their operator.

We demonstrated that the utilization of a high-gain mmWave antenna with beamforming capabilities has the potential to provide better accuracy for drone detection purposes, since it might interfere less with the signals coming from the low-gain directions. Moreover, reuse of the phased antenna arrays with beamsteering properties brings benefits in terms of more intelligent assessment of the threat level. However, due to the added complexity, not every mmWave BS can support such an operation. In particular, mmWave MIMO BSs with digital beamforming (and possibly hybrid beamforming) become preferred candidates for this role, as they can deliver

simultaneous operation of radar and communication modes. Switching between these modes might be resource demanding, thus decreasing performance efficiency in both modes.

REFERENCES

- [1] "Official website of federal aviation administration," [Online]. Available: <https://www.faa.gov/>. [Accessed on 07/2017].
- [2] Y. Zeng, R. Zhang, and T. J. Lim, "Wireless communications with unmanned aerial vehicles: opportunities and challenges," *IEEE Communications Magazine*, vol. 54, pp. 36–42, May 2016.
- [3] H. Zhang, Y. Dong, J. Cheng, M. J. Hossain, and V. C. M. Leung, "Fronthauling for 5G LTE-U ultra dense cloud small cell networks," *IEEE Wireless Communications*, vol. 23, pp. 48–53, December 2016.
- [4] K. Kusume *et al.*, "Updated scenarios, requirements and KPIs for 5G mobile and wireless system with recommendations for future investigations," ICT-317669-METIS/D1.5, April 2015.
- [5] H. Zhang, S. Huang, C. Jiang, K. Long, V. C. M. Leung, and H. V. Poor, "Energy efficient user association and power allocation in millimeter wave based ultra dense networks with energy harvesting base stations," *IEEE Journal on Selected Areas in Communications*, vol. TBD, p. TBD, 2017.
- [6] H. Zhang, N. Liu, X. Chu, K. Long, A. Aghvami, and V. C. M. Leung, "Network slicing based 5G and future mobile networks: Mobility, resource management, and challenges," *IEEE Communications Magazine*, [Online]. Available: <https://arxiv.org/abs/1704.07038>. [Accessed on 07/2017], 2017.
- [7] L. M. L. Oliveira and J. J. P. C. Rodrigues, "Wireless sensor networks: a survey on environmental monitoring," *Journal of Communications*, vol. 6, pp. 143–151, April 2011.
- [8] F. Hoffmann, M. Ritchie, F. Fioranelli, A. Charlish, and H. Griffiths, "Micro-doppler based detection and tracking of UAVs with multistatic radar," in *IEEE Radar Conference (RadarConf)*, pp. 1–6, May 2016.
- [9] D. Solomitckii, Q. C. Li, T. Balercia, C. R. C. M. da Silva, S. Talwar, S. Andreev, and Y. Koucheryavy, "Characterizing the impact of diffuse scattering in urban millimeter-wave deployments," *IEEE Wireless Communications Letters*, vol. 5, pp. 432–435, August 2016.
- [10] G. Kulemin, *Millimeter-wave Radar Targets and Clutter*. Artech House, 2003.
- [11] R. Heckel, "Super-resolution MIMO radar," in *IEEE International Symposium on Information Theory (ISIT)*, pp. 1416–1420, July 2016.
- [12] F. Sohrabi and W. Yu, "Hybrid digital and analog beamforming design for large-scale MIMO systems," in *IEEE International Conference on Acoustics, Speech and Signal Processing (ICASSP)*, pp. 2929–2933, April 2015.
- [13] "Official website of federal communication commission," [Online]. Available: <https://www.fcc.gov/>. [Accessed on 07/2017].
- [14] I. Kononenko and M. Kukar, *Machine Learning and Data Mining*. Elsevier, 1st ed., April 2007.
- [15] Y. Saleem, M. H. Rehmani, and S. Zeadally, "Integration of cognitive radio technology with unmanned aerial vehicles: Issues, opportunities, and future research challenges," *Journal of Network and Computer Applications*, vol. 50, pp. 15–31, 2015.

AUTHORS' BIOGRAPHIES

Dmitrii Solomitckii (dmitrii.solomitckii@tut.fi) is a Ph.D. candidate at the Department of Electronics and Communications Engineering at Tampere University of Technology, Finland. He received the B.Sc. and M.Sc. degrees in electronics and microelectronics from St. Petersburg Electrotechnical University "LETI" in 2006 and 2008, respectively. His research interests include wireless communication focused on propagation physics, antennas, modeling, and signal processing. He also has extensive experience in design electronic systems for critical applications.

Margarita Gapeyenko (margarita.gapeyenko@tut.fi) is a Ph.D. candidate at the Department of Electronics and Communications Engineering at Tampere University of Technology, Finland. She earned her M.Sc. degree in Telecommunication Engineering from University of Vaasa, Finland, in 2014, and

B.Sc. degree in Radio-Engineering, Electronics, and Telecommunications from Karaganda State Technical University, Kazakhstan, in 2012. Her research interests include mathematical analysis, performance evaluation, and optimization methods of future wireless networks, device-to-device communication, and 5G-grade heterogeneous networks.

Vasilii Semkin (vasilii.semkin@aalto.fi) received B.Sc. degree with honors from Saint-Petersburg state University of Aerospace Instrumentation in 2009 and M.Sc. degree in 2011. He received Lic. Sc. (Tech.) in 2014 and D.Sc. (Tech.) in 2016 from Aalto University, School of Electrical Engineering, Finland. He is currently working as a postdoctoral researcher at Aalto University, Department of Electronics and Nano-engineering. He is studying millimeter-wave reconfigurable antennas and radio-wave propagation.

Sergey Andreev (sergey.andreev@tut.fi) is a Senior Research Scientist in the Department of Electronics and Communications Engineering at Tampere University of Technology, Finland. He received the Specialist degree (2006) and the Cand.Sc. degree (2009) both from St. Petersburg State University of Aerospace Instrumentation, St. Petersburg, Russia, as well as the Ph.D. degree (2012) from Tampere University of Technology. Sergey (co-)authored more than 100 published research works on wireless communications, energy efficiency and heterogeneous networking.

Yevgeni Koucheryavy (evgeni.koucheryavy@tut.fi) is a Professor and Lab Director at the Department of Electronics and Communications Engineering of Tampere University of Technology (TUT), Finland. He received his Ph.D. degree (2004) from TUT. He is the author of numerous publications in the field of advanced wired and wireless networking and communications. He is Associate Technical Editor of IEEE Communications Magazine and Editor of IEEE Communications Surveys and Tutorials.

PUBLICATION

VI

Ray-Based Evaluation of Dual-Polarized MIMO in (Ultra-) Dense Millimeter-Wave Urban Deployments

D. Solomitckii, V. Petrov, H. Nikopour, M. Akdeniz, O. Orhan, N. Himayat,
S. Talwar, S. Andreev and Y. Koucheryavy

IEEE 87th Vehicular Technology Conference (VTC Spring). Ed. by 2018

DOI: 10.1109/VTCSpring.2018.8417788

Publication reprinted with the permission of the copyright holders

Ray-Based Evaluation of Dual-Polarized MIMO in (Ultra-)Dense Millimeter-Wave Urban Deployments

Dmitrii Solomitskii*, Vitaly Petrov*, Hosein Nikopour[†], Mustafa Akdeniz[†], Oner Orhan[†],
Nageen Himayat[†], Shilpa Talwar[†], Sergey Andreev*, and Yevgeni Koucheryavy*

*Tampere University of Technology, Tampere, Finland

[†]Intel Labs, Santa Clara, CA, USA

Email: firstname.lastname@tut.fi, firstname.lastname@intel.com

Abstract—Dense deployments of millimeter-wave (mmWave) base stations (BSs) are being considered as the most feasible solution to meet the steadily growing data rate demands of mobile users. Accordingly, the achievable performance gains of mmWave-based dense networks in real deployments have to be studied carefully, since mmWave radio technology features specific transceiver, antenna, and propagation properties. In this paper, we contribute an accurate performance evaluation of single- versus dual-polarized MIMO systems operating over the mmWave channel in typical urban scenarios as well as address the impact of device- and network-centric parameters on the performance gains enabled by MIMO in dense to ultra-dense BS deployments. This study relies on our in-house ray-based modeler and takes into account the key mmWave system effects, such as multi-path propagation, utilization of dual-polarized antennas, and characteristic interference models. Our results show that the benefit of using mmWave-MIMO grows with increasing BS density, thus encouraging a further study of this technology especially for (ultra-)dense setups. We also demonstrate that non-coherent non-polarized diffuse scattering component may reduce the capacity gain of dual-polarized vs. single-polarized MIMO.

I. INTRODUCTION

The New Radio (NR) technology operating over the millimeter-wave (mmWave) spectrum enables the next generation of wireless communication systems aiming to provide improved data rate, latency, and energy-efficiency to mobile users [1]. While the standardization process of the key NR features as part of the fifth-generation (5G) mobile networks is almost complete [2], and the vendors are testing their early implementations [3], the question of what would be the quantitative gains of several advanced mmWave features in real-world deployments and thus is it worth implementing them, remains open [4], [5].

One of the emerging features of the mmWave radio as compared to microwave systems is its inherent ability to operate with compact large-scale antenna arrays [6]. The use of such arrays enables higher directionality of mmWave transmissions, dynamic beam steering and beamforming [7], [8], as well as allows to effectively construct multiple-input multiple-output (MIMO) systems and hence increase the capacity by transmitting multiple data streams in parallel [9].

While the capacity gain of MIMO utilization over mmWave is notable [10], [11], the actual improvement may vary drastically subject to both the environment- and the implementation-specific parameters [12], [13]. Broadly, the existing investi-

gations on MIMO systems capacity can be divided into two groups: (i) general analytical evaluations and (ii) site-specific simulation studies. The authors of the first class of works aim to develop an analytical framework for a generalized (abstract) deployment, so that their model may be applicable to a wide range of scenarios. On the contrary, the second group of papers is dedicated to in-depth analysis of a particular deployment, such that the applicability of the results is exchanged for their accuracy.

There are numerous visible works in the first category. The authors of [14] investigate the system capacity for a group of interfering users that employ single-user detection and multiple transmit/receive antennas over flat Rayleigh-fading channels. Another work in [15] proposes a simple prediction model of MIMO systems capacity by using vertically polarized and dual-polarized antennas. Finally, the study in [16] addresses the potential benefits of dual-polarized arrays in multi-antenna wireless systems. There are more studies in the first group, but all of them introduce certain simplifying assumptions for the sake of modeling tractability, which affects the accuracy of the final results and, consequently, becomes the motivation for the second category of contributions.

The site-specific research typically incorporates detailed ray-based simulations of a given scenario by taking into account realistic antenna gains, site-specific channel gains, and other relevant physical features [17]. For instance, the authors of [18] investigate the channel characteristics for a compact 2x2 MIMO dipole antenna array with decoupling by using ray-tracing simulations. The study presented in [19] addresses the capacity of a 4x4 MIMO system operating at 2.55 GHz and 24 GHz bands through site-specific simulations as well. Finally, the work in [20] reports on the channel behavior with mmWave massive MIMO at 26 GHz.

However, the dense and, especially, ultra-dense deployments of base stations (BSs) in urban scenarios introduce certain additional effects that have to be carefully taken into account in the MIMO studies. The first one is related to inter-cell interference that is typically disregarded in the technical literature, which mainly focuses on the point-to-point mmWave communications [21]. Another one is the effect of realistic beam patterns at both the BS and the user equipment (UE) sides, which is different from idealistic models (e.g., a cone) assumed in many works on the topic [22]. Finally, the utilization of

practical dual-polarized antennas has additional implications on the system behavior. To the best of our knowledge, there has been no study that addresses the capacity gains of MIMO in (ultra-)dense mmWave deployments by carefully accounting for all the aforementioned important effects.

Aiming to bridge this gap, this paper presents an in-depth study of a dense mmWave network with MIMO capabilities. We apply our in-house ray-based simulation framework [23], which is extended to accurately model the effects of (i) inter-cell interference, (ii) dual-polarized antennas, and (iii) practical beam patterns from the codebooks, as well as all the crucial mmWave propagation phenomena, such as reflection, diffraction, and diffuse scattering within the environment. We thus study the capacity gains of mmWave MIMO in realistic urban deployments by quantifying the effects of beamwidth and inter-site distance (ISD). We believe that our evaluation methodology and obtained numerical results may be further employed for the applicability assessment of mmWave MIMO systems in certain practical scenarios.

The rest of this paper is organized as follows. In Section II, the scenario of interest and the deployments under consideration are summarized. Section III outlines the developed evaluation methodology with a focus on the mmWave- and MIMO-specific features. The key numerical results are reported and explained in Section IV, while Section V discusses the important physical effects behind the presented results. The conclusions are drawn in the last section.

II. CONSIDERED DEPLOYMENT

Here, we utilize the Manhattan grid scenario that represents a typical urban area. It has a grid of square buildings (see Fig. 1), 6,500 outdoor UEs (dots in Fig. 1), and a number of mmWave BSs (max 131 items for the highest density). The latter are arranged as a grid with variable ISD between the adjacent nodes 90, 180, and 360 m, while the UE-grid has a constant step of 5 m. It should be noted that depending on the density of the mmWave BSs, the numbers of UEs in the line-of-sight (LoS) and the non-LoS (NLoS) conditions vary. The following proportions of the LoS and NLoS UEs have been considered across the deployment: (i) ultra-dense, $ISD = 90$ m, $UE_{LoS} = 100\%$, $UE_{NLoS} = 0\%$; (ii) dense, $ISD = 180$ m, $UE_{LoS} = 67\%$, $UE_{NLoS} = 23\%$; and (iii) low-dense/sparse, $ISD = 360$ m, $UE_{LoS} = 17\%$, $UE_{NLoS} = 83\%$.

The mmWave carrier frequency utilized in all of our simulations is 28 GHz, which is envisioned for the initial 5G mmWave cellular deployments [24]. In the subsequent study, we primarily focus on the downlink transmissions. The remaining parameters of our deployment of interest are summarized in Table I.

III. DEVELOPED EVALUATION METHODOLOGY

This section summarizes our evaluation methodology. Subsection III-A introduces our methodology at-a-glance, subsection III-B explains the details of how the antenna polarization effects are taken into account, while the implementation of the diffuse scattering model is explained in subsection III-C,

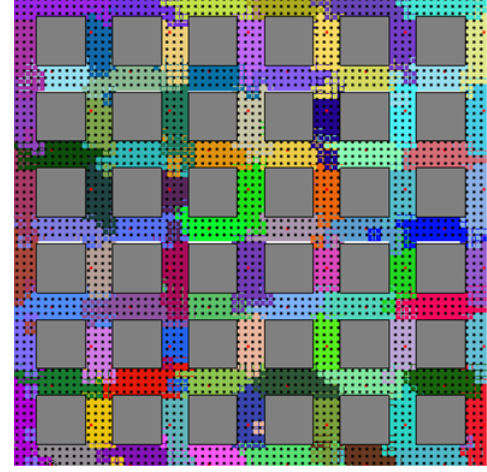


Fig. 1. Urban mmWave deployment of interest. Gray-colored squares represent buildings and black dots are UEs. Each color demonstrates a certain group of UEs belonging to a single mmWave BS.

TABLE I
CONSIDERED SCENARIO PARAMETERS

Parameter	Value
Total square, m	800 x 800
Propagation area, m	600 x 600
Building, m	60 x 60 x 100
Road width, m	20
Wall width, m	0.3
Wall material	concrete
Selected ISDs, m	90, 180, 360
Selected HPBW, °	12, 30, 50
Carrier frequency, GHz	28
Bandwidth, GHz	0.5
Noise figure, dB	7

and the procedure of MIMO capacity evaluation is outlined in subsection III-D.

A. Methodology-at-a-Glance

Our evaluation methodology utilized in this paper comprises two stages: (i) deterministic ray-based simulation and (ii) refining procedure. The first stage is carried out by our in-house ray-based modeler, which was calibrated against the recent mmWave numerology in various scenarios [23], [25]. The tool is used to model all of the possible connections between every UE-BS pair and characterize the mmWave radio channel between them. The output of the first stage is the channel impulse response (CIR) between each Tx antenna at the mmWave BS and Rx antenna at the UE:

$$h(\tau, \theta, \gamma) = \sum_{n=1}^N a_n \exp(j\phi_n) \delta(\tau - \tau_n) \delta(\phi^{Rx} - \phi_n^{Rx}) \delta(\theta^{Rx} - \theta_n^{Rx}) \delta(\phi^{Tx} - \phi_n^{Tx}) \delta(\theta^{Tx} - \theta_n^{Tx}), \quad (1)$$

where a_n is the amplitude of n^{th} multipath component arriving at a certain Tx antenna of a particular UE from the direction having azimuth and elevation components (angle of arrival, AoA) as follows $[\phi^{Rx}, \theta^{Rx}]$. At the same time, $[\phi^{Tx}, \theta^{Tx}]$ describes the departure direction (angle of departure, AoD)

of n^{th} multipath component from the antenna of a particular mmWave BS. The output data is stored in a sorted database.

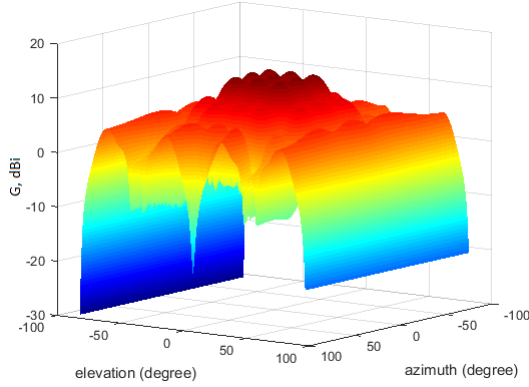


Fig. 2. Typical codebook with HPBW = 50° oriented along $\phi = 0^\circ$ and $\theta = 0^\circ$. The main lobe consists of multiple smaller beams due to large HPBW.

Once all of the CIRs are obtained, the refining stage begins by applying a channel access abstraction that models a round-robin algorithm together with the corresponding antenna radiation patterns. The overall evaluation process can be briefly summarized as follows:

- 1) Each UE is associated with a serving BS based on the SNR maximization criterion.
- 2) Each of the BSs randomizes the order of UEs associated to it, so that the scheduling interval for the UE does not depend on its initial number. This step is needed to accurately model the inter-cell interference.
- 3) Simulations are run in a time-driven fashion. During each of the scheduling intervals, the BS selects a UE from its list. For the selected UE, the serving BS defines the best AoD and AoA according to the SNR multipaths.
- 4) Both the BS and the UE search for the most beneficial antenna pattern (w.r.t. the SNR maximization criterion) from their codebooks and thus align the main lobes of their beams according to the estimated AoA and AoD values. Accordingly, the “best” beam configuration between each of the UE and the associated BS is established and the mmWave channel between them can now be evaluated.
- 5) The tool sequentially calculates the capacity for each BS-UE link by carefully considering the impact of inter-cell interference.
- 6) Return to step 2) to randomize the interference.
- 7) After a given number of rounds, the data for the current sample is stored, while the deployment becomes randomized and the procedure reiterates. Steps 2)–6) are repeated and the intermediate statistics are collected for each of them.
- 8) For the sake of higher accuracy in the mean output results, the intermediate values for each of the samples are averaged over 100 replications.

In this study, the practical codebooks were used that rep-

resent realistic antenna radiation patterns at mmWave frequencies. The employed codebooks cover all of the possible azimuthal and elevation directions. The number of utilized codebooks per a simulation run depends on their HPBW (169 codebooks for HPBW = 13° and 9 for HPBW = 50°). An example codebook with HPBW = 50° oriented at $\phi = 0^\circ$ and $\theta = 0^\circ$ is illustrated in Fig. 2.

We believe that the proposed approach offers appropriate balance between accuracy and flexibility. Its inherent advantage is that the ray-based geometry between the BS and the UE does not have to be recalculated at every step, as it is typically done in the state-of-the-art solutions. Instead, our tool models a scenario with omnidirectional antenna radiation patterns only once and then produces the final results by adjusting the data at the output of the omnidirectional modeling according to the selected antenna radiation pattern: certain rays become stronger or weaker depending on the AoA, AoD, and the antenna radiation pattern. However, our numerical results remain in-line with those contributed by the past studies in [26], [27].

B. Considering Polarization

To model the MIMO channel between the UE(s) and the mmWave BS(s), all of them were equipped with 8x8 antenna arrays in case of single polarization and with 16x16 arrays in case of dual polarization (slanted antennas). The latter option was simulated as two collocated 8x8 antenna arrays with the relative orthogonal polarizations of $\pm 45^\circ$. Hence, based on electromagnetic theory, such slanted orientation might be resolved as a combination of both the vertical and the horizontal components of electrical field radiated by the antenna:

$$\mathbf{E}_{\text{tot}} = \hat{\mathbf{e}}_{\parallel} E^{\parallel} + \hat{\mathbf{e}}_{\perp} E^{\perp}, \quad (2)$$

where $\hat{\mathbf{e}}_{\parallel}$ and $\hat{\mathbf{e}}_{\perp}$ are the basis. This means that a signal radiated from such a slanted antenna carries both polarization components by default and thus each of them suffers from intermediate interaction with the surrounding objects. It is represented in our methodology via dyadic reflection and diffraction coefficients. It was also assumed that a single Tx antenna at the BS side communicates with each Rx antenna at the UE side. Therefore, when receiving a signal for which polarization differs by 90° from the polarization of the receiving antenna, the received power level will be negligible.

C. Diffuse Scattering Effects

With respect to the existing studies, an additional Lambertian model of diffuse scattering on reflection was added to our proposed methodology. This model was included after several preliminary simulations in order to strengthen the potential output results (will be discussed in detail in Section IV). Following the said model, a signal reflecting from a surface with certain effective roughness produces the coherent (specular) and incoherent (diffuse scattering) components being radiated by the surface. Specifically, specular amplitude is negatively related to the diffuse scattering components through the coefficient of roughness. Accordingly, the total signal strength of the UE's Rx is a combination of the specular

and the diffuse scattering paths: $E_{tot} = E_{spec} + E_s$. Here, the magnitude of diffuse scattering electrical field is represented by the following equation [28]:

$$|E_s|^2 = |E_{s0}|^2 \cdot \cos(\theta_s) = \frac{dS \cdot S^2 \cdot \cos(\theta_i) \cdot \cos(\theta_s)}{\pi r_i^2 \cdot r_s^2}. \quad (3)$$

In (3), $|E_{s0}|$ is the amplitude of a radiated signal, θ_s and θ_i are the angles of scattered and incident fields, r_i is the distance from the Tx to the area of scattering, and r_s is the distance from the area of scattering to the Rx. Each of the building walls is divided into multiple tiles (scattering sources) with the linear size of dS . Finally, S is a coefficient that defines the amount of scattered field with respect to the incident field and demonstrates the diffuse scattering capability of a certain surface, such that $S = \frac{E_s}{E_i}$. The value of S may be calculated analytically from the reflection and roughness coefficients, but we here adopt specific practical values of 0.1, 0.3, and 0.6 from [29], [30]. We additionally assume that a diffuse scattered signal is incoherent, which means that each scattered ray carries a randomly polarized signal [31] i.e., the polarization vector may be oriented in any direction.

D. Capacity of mmWave MIMO System

In order to post-process the calculated intermediate results and estimate the capacity of the mmWave MIMO system, the following canonical approach has been utilized:

$$C = \log_2 \det(\mathbf{I} + \mathbf{P}_i^{-1} \mathbf{P}_{rx}), \quad (4)$$

where the power at Rx might be represented as a combination of the co- and cross-polarized power of a multipath signal. The latter is given by:

$$\mathbf{P}_{rx} = \frac{1}{N} \begin{pmatrix} P_{vv}^{Rx} & P_{vh}^{Rx} \\ P_{hv}^{Rx} & P_{hh}^{Rx} \end{pmatrix}. \quad (5)$$

Further, to simplify the numerical calculations, the matrix responsible for the co-channel interference has been rewritten as follows:

$$\mathbf{P}_i = \begin{pmatrix} NL + P_{vv}^i & NL \\ NL & NL + P_{hh}^i \end{pmatrix}, \quad (6)$$

where NL is the noise level set to 80 dBm, which corresponds to 0.5 GHz of bandwidth, while I_{vv} I_{hh} are the interfering power from the mmWave BSs to $+45^\circ$ and -45° .

In (4), the component $\mathbf{P}_i^{-1} \mathbf{P}_{rx}$ represents the ideal SINR, which may reach an impractical value of over 35 dB. To incorporate the realistic limits imposed by the practical mmWave modulation and coding schemes (MCSs) [32], we add the error vector magnitude (EVM) to the estimated signal, which maximum value is set to 27 dB. Generally, this parameter is a measure of error in the constellation of a modulated signal, which actually determines the maximum SINR that might be reached at the Rx side in the case of no additional impairments to the Tx signal [33]. Adjusting the SINR with the help of the EVM has been implemented by using the following equation:

$$\frac{1}{\text{SINR}_{EVM}} = \frac{1}{\text{SINR}} + \frac{1}{\text{EVM}}. \quad (7)$$

An additional cap was further applied to the maximum achievable value of the spectral efficiency as 4.8 bit/s/Hz, which corresponds to 64QAM with the coding rate of 4/5. The minimum sensitivity level for the outage conditions was also introduced ($\text{SINR} < -6$ dB in our case), which defines the minimum supported SINR along the list of the utilized MCSs. We offer the numerical results produced by our evaluation methodology in the following section.

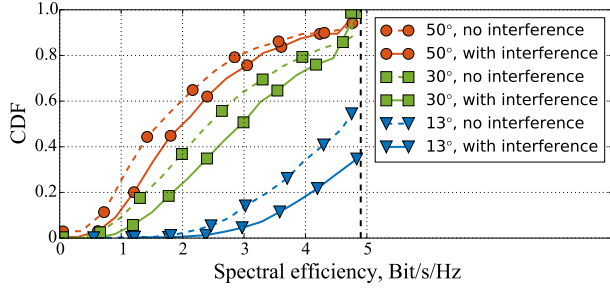
IV. NUMERICAL RESULTS

First, we present the cumulative distribution function (CDF) of the UE spectral efficiency by taking into account different HPBW (13°, 30°, and 50°) and ISDs (180 m and 360 m). The output results for the single- and dual-polarized MIMO spectral efficiency are displayed in Fig. 3. These plots confirm that in the low-dense (ISD = 360 m) and, especially, dense (ISD = 180 m) regime, higher gains of the antenna radiation pattern lead to better spectral efficiency. Specifically, in Fig 3(a) (ISD = 180 m), the spectral efficiency is within the range of 2.0–4.8 bit/s/Hz, while Fig. 3(c) (ISD = 360 m) demonstrates the range of 0–2.1 bit/s/Hz, correspondingly. For dual-polarized MIMO, the respective values are: 3.9–9.6 bit/s/Hz for ISD = 180 m, see Fig. 3(b), and 0–3.9 bit/s/Hz for ISD = 360 m, see Fig. 3(d). Another interesting observation from Fig. 3 is that ISD = 180 m guarantees that all of the UEs have their spectral efficiency of over 0, while 50–60% of the UEs are in outage (spectral efficiency is zero) with ISD = 360 m. Here, with large ISD the system operates primarily in the noise-limited regime, while the contribution of interference becomes of secondary importance.

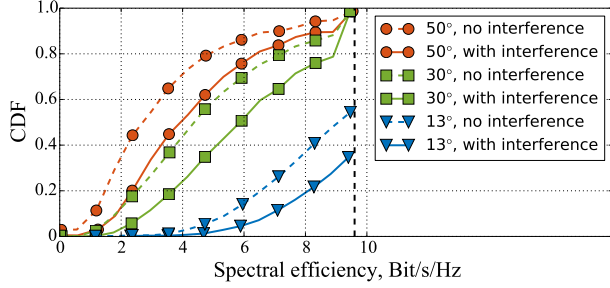
We further study the capacity gain provided by a dual-polarized system vs. a single-polarized counterpart. To this aim, the ratios of the two average capacities are calculated as Capacity Gain = C_{dual}/C_{single} , while the output is collected in Fig. 4. Understanding the results in Fig. 4, we conclude that the capacity of a dual-polarized MIMO system decreases with the increase in the ISD as well as the impact of the non-polarized diffuse scattering (coefficient S). When diffuse scattering is small ($S = 10\%$), the slope of the dashed line is negligible and none of the HPBWs provide with any notable advantage in terms of capacity. In particular, the capacity gain at ISD = 90 m is about 1.98 (98% improvement), whereas the one at ISD = 360 m is 1.95. Further increase in S to 0.3 leads to a non-uniform decrease in the gain down to 1.95 at ISD = 90 m and 1.84 at ISD = 360 m, respectively. The most significant decrease in the capacity gain is observed at $S = 0.6$, when the ISD is equal to 360 m (only 1.74). Based on the technical literature, further growth of S is impractical for urban deployments [31].

V. DISCUSSION

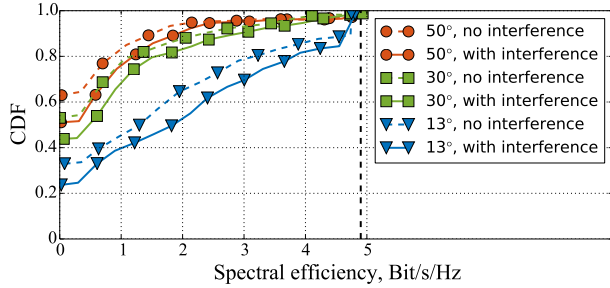
A polarized MIMO channel with two orthogonal branches provides a higher number of uncorrelated communication channels (channel matrix rank is 2), which could potentially double the channel capacity. However, based on our simulation results, the idealistic value of 2 has never been achieved



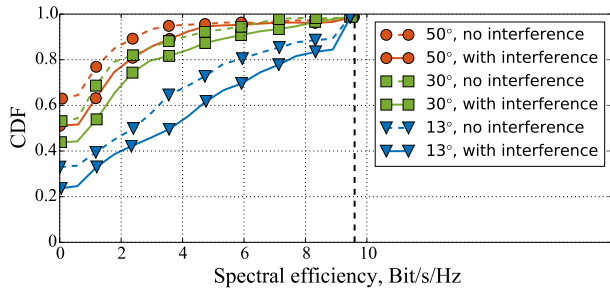
(a) ISD = 180 m, single stream



(b) ISD = 180 m, dual stream



(c) ISD = 360 m, single stream

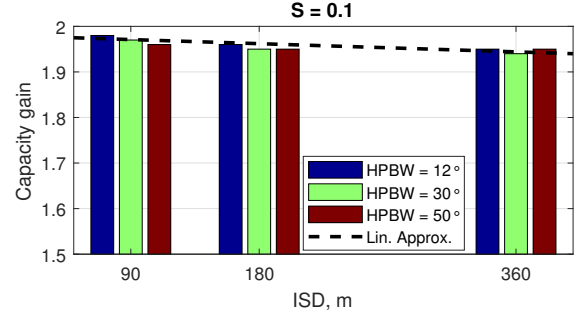


(d) ISD = 360 m, dual stream

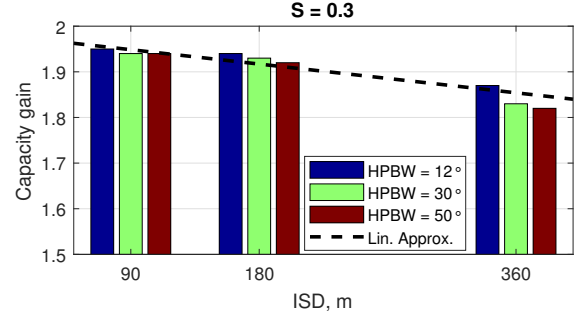
Fig. 3. Spectral efficiency for single- and dual-polarized mmWave MIMO system at $S = 0.1$, different ISDs and HPBW.

subject to practical losses due to signal attenuation, scattering, and inter-cell interference. Particularly, a gradual decrease of capacity occurs with the growing distance, HPBW, and, especially, the environment property S . Below, we briefly explain and interpret these observations.

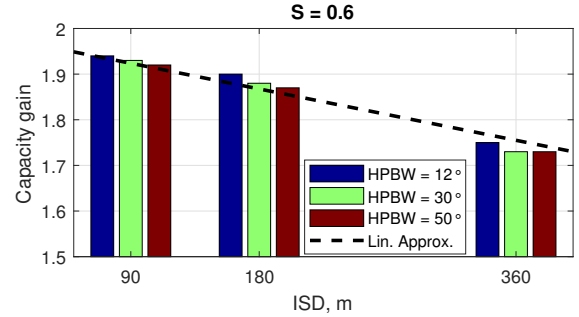
Theoretically, an arbitrarily polarized signal (having both polarization components) that impinges on a free-oriented surface may change its polarization after a reflection. It happens because the reflection coefficients (often named the Fresnel



(a)



(b)



(c)

Fig. 4. Capacity gain for single-polarized MIMO channel vs. dual-polarized MIMO-channel as a function of ISD, HPBW, and diffuse scattering coefficient. Capacity gain reduces significantly with distance and the amount of scattered field. Also, some decrease in capacity occurs with growing HPBW.

coefficients) are different for the two polarization types, see Fig. 5. Hence, the horizontal component attenuates faster with respect to the vertical component after each reflection. Subsequently, two signals emitted by any mmWave BS with orthogonal polarization and suffering from intermediate interaction with the objects can no longer be considered in isolation with respect to each other at the UE side, since the polarization angle cannot be 90° . This effect is known as *depolarization* and leads to an imbalance of the matrix in (5) by increasing the non-diagonal received power components and thus decreasing the total capacity.

On the other hand, despite the fact that more reflections make depolarization higher, the amplitude of the signal is steadily dropping. The degradation rate depends on the angle of incidence and the dielectric permittivity of a surface. Fig. 6 demonstrates a situation where the dielectric permittivity of

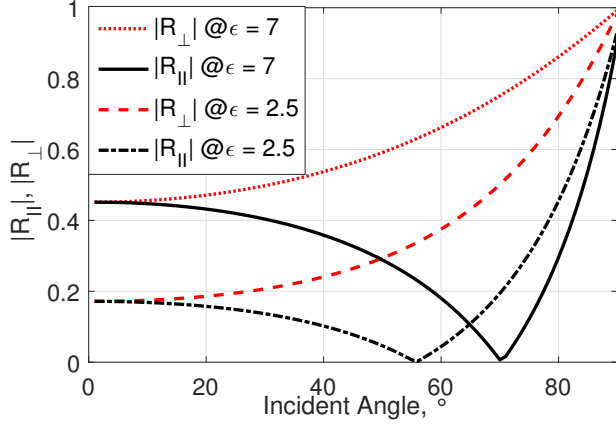


Fig. 5. Reflection coefficient R for horizontal (black) and vertical (red) polarization. Higher dielectric permittivity ϵ leads to larger reflection coefficient and thus greater reflected power.

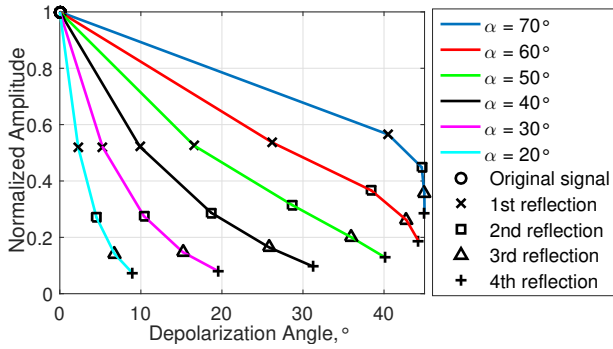


Fig. 6. Signal impinging on a surface experiences a depolarization effect by changing its polarization by a certain angle. Greater angle of incidence α leads to more significant depolarization.

surrounding walls is $\epsilon = 7$ (concrete at mmWave). Accordingly, it can be observed that the original signal (normalized for simplification) sent by a single slanted antenna ($+45^\circ$) changes its amplitude and orientation of the polarization vector toward vertical direction after each step of reflection. Therefore, the highest probability of depolarization may occur when the incident angle α is large and the material is not transparent for transmission. The second criterion is based on the propagation principle where transmission and reflection are negatively related to each other through the dielectric permittivity, ϵ : higher reflectivity is connected to smaller transmission capability.

Another criterion of wide incident angle is when the UE and the BS are located far from each other (case BS2-UE1 in Fig. 7) or close to a building (case BS1-UE2 in Fig. 7). Due to the fact that the core of our methodology exploits a specular reflection model from the conditionally idealized surface (without irregularities, roughness, detailization, etc.), the impact of cross-polarization components may be underestimated. Moreover, the average cross-polarization ratio (XPR) is on the order of 30 dB, which is rather high [34], [35].

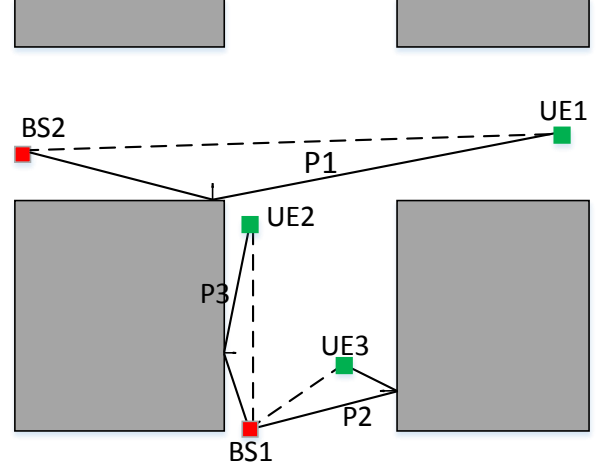


Fig. 7. Favorable (BS1-UE2 and BS2-UE1) and unfavorable (BS1-UE3) conditions for emergence of cross-polarization losses.

To improve on this situation, a model for the first-order diffuse scattering from surface irregularities was introduced to our methodology. It operates as an additional amplification of the cross-polarized received power. However, the functionality of this model is limited and thus the impact on MIMO capacity is reduced. Primarily, it is connected with significant attenuation and the contribution of power. Consequently, it should also be mentioned that in the presence of a LoS-path (or another strong path), the effect of depolarization is negligible. Therefore, even in diffuse scattering rich deployments, the capacity of a dual-polarized MIMO system with small ISDs practically does not change. However, with the increasing ISD and subsequently growing number of NLoS UEs, the influence of depolarizing paths improves, which leads to a decrease in capacity. In such conditions, small capacity drops as HPBW widens are associated with larger diffusing areas on walls, which also somewhat degrade the capacity.

VI. CONCLUSIONS

Dense and ultra-dense mmWave networks are envisioned to soon become an integral part of 5G and beyond-5G wireless systems. While the incorporation of mmWave technology brings notable gains in the network capacity, research currently investigates if these benefits can be increased further by the use of advanced radio techniques. In this paper, a detailed analysis of the mmWave MIMO system in a realistic deployment has been conducted. It was shown that the gain of using the dual-polarized mmWave array vs. the single-polarized option varies in the range of 1.7–2 with the BS density and the directivity of the preferred antenna radiation pattern. It was also demonstrated that the negative effect of interference at higher densities of BSs is well mitigated by the fact that the overwhelming majority of the UEs are in the LoS conditions with respect to the associated BS. Accordingly, the impact of

the mmWave MIMO is the greatest for the highest considered density of the BSs, thus advocating for the use of MIMO systems in dense and, especially, ultra-dense urban mmWave deployments.

ACKNOWLEDGMENT

This work was supported by Intel Corporation, by the Academy of Finland (projects WiFiUS and PRISMA), and by the project TAKE-5: The 5th Evolution Take of Wireless Communication Networks, funded by Tekes. V. Petrov acknowledges the support of HPY Research Foundation funded by Elisa.

REFERENCES

- [1] S. Y. Lien, S. L. Shieh, Y. Huang, B. Su, Y. L. Hsu, and H. Y. Wei, "5G New Radio: Waveform, Frame structure, Multiple Access, and Initial Access," *IEEE Communications Magazine*, vol. 55, no. 6, pp. 64–71, 2017.
- [2] A. A. Zaidi, R. Baldemair, M. Andersson, S. Faxer, V. Moles-Cases, and Z. Wang, "Designing for the future: The 5G NR physical layer," *Ericsson Technology Review*, pp. 1–13, June 2017.
- [3] W. Hong, K. H. Baek, Y. Lee, Y. Kim, and S. T. Ko, "Study and prototyping of practically large-scale mmWave antenna systems for 5G cellular devices," *IEEE Communications Magazine*, vol. 52, pp. 63–69, September 2014.
- [4] M. Xiao *et al.*, "Millimeter wave communications for future mobile networks [Editorial]," *IEEE Journal on Selected Areas in Communications*, vol. 35, pp. 1909–1935, September 2017.
- [5] V. Petrov, D. Solomitckii, A. Samuylov, M. A. Lema, M. Gapeyenko, D. Moltchanov, S. Andreev, V. Naumov, K. Samouylov, M. Dohler, and Y. Koucheryavy, "Dynamic multi-connectivity performance in ultra-dense urban mmWave deployments," *IEEE Journal on Selected Areas in Communications*, vol. 35, pp. 2038–2055, September 2017.
- [6] H. K. Pan, B. D. Horine, M. Ruberto, and S. Ravid, "Mm-wave phased array antenna and system integration on semi-flex packaging," in *Proc. of IEEE International Symposium on Antennas and Propagation (IEEE APSURSI)*, pp. 2059–2062, July 2011.
- [7] S. Jayaprakasam, X. Ma, J. W. Choi, and S. Kim, "Robust beam-tracking for mmwave mobile communications," *IEEE Communications Letters*, vol. 21, pp. 2654–2657, December 2017.
- [8] V. Petrov, D. Moltchanov, and Y. Koucheryavy, "Applicability assessment of terahertz information showers for next-generation wireless networks," in *Proc. of IEEE International Conference on Communications (ICC)*, pp. 1–7, May 2016.
- [9] S. Sun, T. S. Rappaport, R. W. Heath, A. Nix, and S. Rangan, "MIMO for millimeter-wave wireless communications: Beamforming, spatial multiplexing, or both?," *IEEE Communications Magazine*, vol. 52, pp. 110–121, December 2014.
- [10] J. Mo and R. W. Heath, "High SNR capacity of millimeter wave MIMO systems with one-bit quantization," in *Proc. of Information Theory and Applications Workshop (ITA)*, pp. 1–5, February 2014.
- [11] S. A. Hoseini, M. Ding, and M. Hassan, "A new look at MIMO capacity in the millimeter wave," in *Proc. of IEEE Global Communications Conference (GLOBECOM)*, December 2017.
- [12] M. K. Samimi, S. Sun, and T. S. Rappaport, "MIMO channel modeling and capacity analysis for 5G millimeter-wave wireless systems," in *Proc. of 10th European Conference on Antennas and Propagation (EuCAP)*, pp. 1–5, April 2016.
- [13] J. C. Shen, J. Zhang, and K. B. Letaief, "Downlink user capacity of massive MIMO under pilot contamination," *IEEE Transactions on Wireless Communications*, vol. 14, pp. 3183–3193, June 2015.
- [14] R. S. Blum, "MIMO capacity with interference," *IEEE Journal on Selected Areas in Communications*, vol. 21, pp. 793–801, June 2003.
- [15] V. Eiceg, H. Sampath, and S. Catreux-Erceg, "Dual-polarization versus single-polarization MIMO channel measurement results and modeling," *IEEE Transactions on Wireless Communications*, vol. 5, pp. 28–33, January 2006.
- [16] C. Oestges, B. Clerckx, M. Guillaud, and M. Debbah, "Dual-polarized wireless communications: from propagation models to system performance evaluation," *IEEE Trans. Wireless Commun.*, pp. 4019–4031, Oct. 2008.
- [17] C. Wang, H. Papadopoulos, K. Kitao, and T. Imai, "Ray-tracing based performance evaluation of 5G mmWave massive MIMO in hotspots," in *Proc. of International Symposium on Antennas and Propagation (ISAP)*, pp. 608–609, October 2016.
- [18] M. M. Taygur, W. K., and E. T. E., "Ray tracing based channel analysis involving compact MIMO antenna arrays with decoupling networks," *Proc. of the 20th International ITG Workshop on Smart Antennas (WSA 2016)*, March 2016.
- [19] J. W. Wallace, W. Ahmad, Y. Yang, R. Mehmood, and M. A. Jensen, "A comparison of indoor MIMO measurements and ray-tracing at 24 and 2.55 GHz," *IEEE Transactions on Antennas and Propagation*, vol. 65, pp. 6656–6668, December 2017.
- [20] B. Ai, K. Guan, R. He, J. Li, G. Li, D. He, Z. Zhong, and K. M. S. Huq, "On indoor millimeter wave massive MIMO channels: Measurement and simulation," *IEEE Journal on Selected Areas in Communications*, vol. 35, pp. 1678–1690, July 2017.
- [21] D. Solomitckii, V. Petrov, H. Nikopour, M. Akdeniz, O. Orhan, N. Himayat, S. Talwar, S. Andreev, and Y. Koucheryavy, "Detailed interference analysis in dense mmWave systems employing dual-polarized antennas," in *Proc. of IEEE Globecom Workshops (GC Wkshps)*, pp. 1–7, December 2017.
- [22] V. Petrov, M. Komarov, D. Moltchanov, J. M. Jornet, and Y. Koucheryavy, "Interference analysis of EHF / THF communications systems with blocking and directional antennas," in *Proc. of IEEE Global Communications Conference (GLOBECOM)*, pp. 1–7, December 2016.
- [23] D. Solomitckii, Q. C. Li, T. Balercia, C. R. C. M. da Silva, S. Talwar, S. Andreev, and Y. Koucheryavy, "Characterizing the impact of diffuse scattering in urban millimeter-wave deployments," *IEEE Wireless Communications Letters*, vol. 5, pp. 432–435, August 2016.
- [24] M. R. Akdeniz, Y. Liu, M. K. Samimi, S. Sun, S. Rangan, T. S. Rappaport, and E. Erkip, "Millimeter wave channel modeling and cellular capacity evaluation," *IEEE Journal on Selected Areas in Communications*, vol. 32, pp. 1164–1179, June 2014.
- [25] D. Solomitckii, M. Gapeyenko, S. S. Szyszkowicz, S. Andreev, H. Yanikomeroğlu, and Y. Koucheryavy, "Toward massive ray-based simulations of mmWave small cells on open urban maps," *IEEE Antennas and Wireless Propagation Letters*, vol. 16, pp. 1435–1438, December 2017.
- [26] 3GPP, "Channel model for frequency spectrum above 6 GHz (Release 14)," 3GPP TR 38.900 V2.0.0, 2016.
- [27] "METIS channel models," Tech. Rep. ICT-317669-METIS/D1.4, METIS, February 2015.
- [28] V. Degli-Esposti, D. Guiducci, A. de'Marsi, P. Azzi, and F. Fuschini, "An advanced field prediction model including diffuse scattering," *IEEE Transactions on Antennas and Propagation*, vol. 52, pp. 1717–1728, July 2004.
- [29] V. Degli-Esposti and H. L. Bertoni, "Evaluation of the role of diffuse scattering in urban microcellular propagation," *Proc. IEEE Vehicular Technology Conference (IEEE VTC)*, p. 1922, September 1999.
- [30] J. Pascual-Garcia, M. T. Martinez-Ingles, J. M. Molina-Garcia-Pardo, J. V. Rodriguez, and V. Degli-Esposti, "Experimental parameterization of a diffuse scattering model at 60 GHz," in *Proc. of IEEE-APS Topical Conference on Antennas and Propagation in Wireless Communications (APWC)*, pp. 734–737, September 2015.
- [31] V. Degli-Esposti, F. Fuschini, E. M. Vitucci, and G. Falciaeseca, "Measurement and modelling of scattering from buildings," *IEEE Transactions on Antennas and Propagation*, vol. 55, no. 1, pp. 143–153, 2007.
- [32] R. Ford, M. Zhang, S. Dutta, M. Mezzavilla, S. Rangan, and M. Zorzi, "A framework for end-to-end evaluation of 5G mmWave cellular networks in ns-3," in *Proc. of the Workshop on Ns-3*, ACM, 2016.
- [33] E. Dahlman, S. Parkvall, and J. Skold, *4G, LTE-advanced Pro and the Road to 5G*. Academic Press, 2016.
- [34] K. Haneda, J. Zhang, L. Tan, G. Liu, Y. Zheng, H. Asplund, J. Li, Y. Wang, D. Steer, C. Li, *et al.*, "5G 3GPP-like channel models for outdoor urban microcellular and macrocellular environments," in *Proc. of IEEE Vehicular Technology Conference (IEEE VTC)*, IEEE, 2016.
- [35] C. Gustafson, D. Bolin, and F. Tufvesson, "Modeling the polarimetric mm-wave propagation channel using censored measurements," in *Proc. of IEEE Global Communications Conference (IEEE GLOBECOM)*, IEEE, 2016.

PUBLICATION

VII

Characterizing Radio Wave Propagation in Urban Street Canyon with Vehicular Blockage at 28 GHz

D. Solomitckii, V. Semkin, A. Karttunen, V. Petrov, S. Nguyen, H. Nikopour,
K. Haneda, S. Andreev, S. Talwar and Y. Koucheryavy

IEEE Transaction on Vehicular Technologies (2019). Accepted, to appear.

Publication reprinted with the permission of the copyright holders

